university of groningen

Data processing and applications of fluorescent nanodiamonds for bio-technology

PhD thesis

to obtain the degree of PhD at the
University of Groningen
on the authority of the
Rector Magnificus Prof. C. Wijmenga
and in accordance with
the decision by the College of Deans.

This thesis will be defended in public on

Wednesday 25 January 2023 at 12.45 hours

by

Thea Annie Vedelaar

born on 4 February 1994
in Emmen, the Netherlands

Supervisor
Prof. R. Schirhagl

Co-supervisor
Prof. V.G. Damle

Assessment Committee
Prof. A. Hermann
Prof. T. Cordes
Prof. P. Rudolf

Cover art by: Alexander Korf

Paranymps:

Runrun Li

Ari Rolando Ortiz Moreno

Contents

Chapter 1 General introduction 5

Chapter 2 Optimising data processing for nanodiamond based relaxometry..... 13

Chapter 3 Insight into a Fenton-Like Reaction Using Nanodiamond Based Relaxometry 39

Chapter 4 Following polymer degradation with nanodiamond magnetometry 65

Chapter 5 Applying NV center-based quantum sensing to study intracellular free radical response upon viral infections .. 101

Chapter 6 General discussion 155

Summary 164

Samenvatting 166

Acknowledgements 169

About the Author..... 173

Chapter 1

General Introduction

1.1 Diamond applications

Sparkling, beautiful, durable these are some of the properties commonly associated with diamond. These qualities have made them desirable within our society for a very long time. The most well-known purpose of diamond is as a valuable gemstone, to be embedded in crowns, rings and other tokens of wealth. Nowadays diamonds are still often found in jewelry, but understanding their unique properties lead to using them for other applications as well, some of which are less visible. Each of these relies on specific material properties. One of them is the hardness which enables diamond tools to cut other extremely hard materials like glass, concrete and other diamonds. Another property is the high thermal conductivity which can be used to produce heat sinks in super computers. In the recent years, material development enabled the growth of thin layers of diamond which make glass more heat and scratch resistant. This shows that diamond has a wide range of properties which can be used as either a stand-alone product or to improve an already existing one.

1.2 Properties of diamond

Also in research, diamond properties are unique. The first property which is usually focused on is the hardness of the material, which is around 100GPa. This is due to carbon atoms being relatively small and strongly covalently bound to their neighbors with a short bond length leading to a very tight packing[1]. Diamond has a large bandgap due to low electron mobility in the lattice, which means that diamond is a good insulator and is transparent for a large range of wavelengths. However these properties can be tuned depending on how the material is obtained[2]. As a result diamonds can be used as insulators for new types of electronics[3,4]. Another property, the biocompatibility and chemical stability of the surface has allowed numerous biological applications, such as the growth of cells on a diamond film or the uptake of nanodiamonds with varying sizes into cells[5–7]. One use of nanodiamonds in biological environments so far has been as drug delivery carriers[8,9].

1.3 From material properties to sensing

Another important property comes not from the carbons in the diamond structure itself, but from defects in the diamond. There are a number of possible defects, with the most common being vacancies, substitution with another element like nitrogen, silicon or boron or a combination of these. The most well studied is the combination of a substitution with nitrogen with an adjacent vacancy, the so called nitrogen vacancy center (NV-center). There are a number of key properties that enable the use of the NV-centers in biology: a photostable transition, a ground state that can couple to electronic and nuclear spins and polarizability[10]. Due to the coupling to different types of spins, the NV-center in diamond can be used to sense free radicals, which contain an unpaired electron. These free radicals are produced in a number of processes in healthy cells but also play a key role in a large number of diseases and are a factor in ageing[11]. These molecules are hard to measure due to their high reactivity, which means that they only exist for a limited time (from nanoseconds). The most common conventional ways to detect these are with various dyes that react with specific free radicals, electron spin resonance (ESR) and gene expression assessments[12].

1.4 The NV-centers in biomedical engineering

The excellent properties of the NV-center in diamond have spurred the development of various techniques towards sensing the properties of interest. In physics these properties are currents in materials and magnetic fields[13–15]. In chemistry the sensing of specific compounds which have a spin component are the main interest[16,17]. In biology we use them as a fluorescent probe to sense free radicals in cells[18,19]. The application in cells is favorable as the sensing can be performed in single living cells, at room temperature and in real time[20]. As the Fluorescent nanodiamonds (FNDs) which are commonly used for this purpose are usually larger than their counterparts for drug delivery, a number of tests were performed to address the uptake of the FNDs. These have shown that FNDs are endocytosed by most cells including macrophages, HeLa and lung cells[6,21]. However, besides the implementation in cells, the FNDs can be embedded into other materials which are potentially interesting in different fields[22].

Sensing with FNDs additionally has a number of modes in which it can be used. All of these rely on the properties of the NV-center itself, namely the linking between magnetic fields or noise and the ability to polarize the center. All of the methods require the excitation and following polarization of the NV-center and most of the time the use of microwaves. The method we use in this thesis is the so called T1 relaxation measurement. The main advantage of this method is that it can be performed without the use of microwaves, therefore reducing the complexity and prize of equipment. The basic principle of a T1 measurement is shown in figure 1, where first the NV-centers are polarized into the $m_s = 0$ state with a laser pulse. Afterwards the laser is turned off and the system is allowed to relax back to the equilibrium. The speed at which the system returns to equilibrium depends on the surrounding of the NV-center. When there is a lot of spin noise, will be accelerated[23].

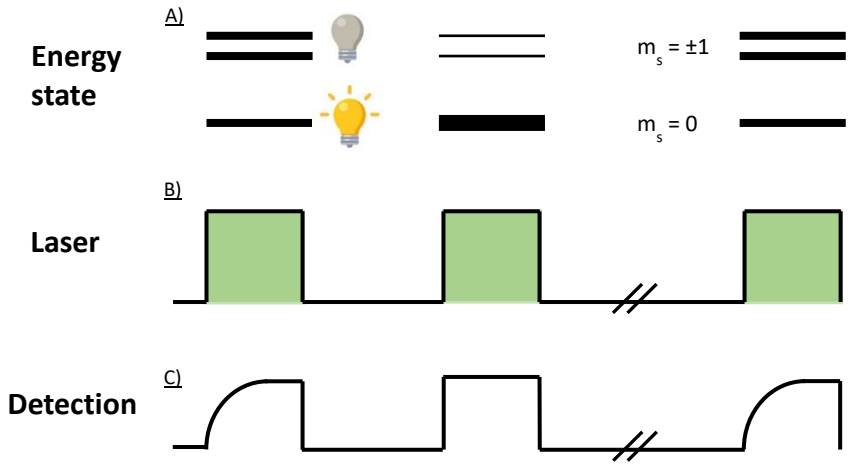

Figure 1. The basic principles of a T1 measurement. A) The energy states of the NV-center during the T1 measurement. The thickness of the line correlates to the population densities at different stages during the T1 measurement. When the population density in the $m_s = 0$ state is high (thick line) the resulting fluorescence is high. B) The pulsing sequence of the laser. During the pulsing of the laser (532nm) the NV-center will be polarized into the $m_s = 0$ state. The laser is pulsed to allow the system to relax back to an equilibrium state. Each pulse is used to both probe the population densities and to initialize the system for the next measurement. C) The resulting detected signal. During the pulsing of the laser, the resulting signal is detected. When starting from equilibrium, the transitions from the $m_s = \pm 1$ will not add to the detected signal, resulting in a build up in the pulses.

1.5 Objective and outline

This thesis focuses on improving and applying T1 to sense processes based on free spins in different cases important within biomedical engineering. The first step towards implementation of T1 is to understand the processes involved in relaxation time and modelling this process. In **chapter 2** calibration data from diamonds exposed to gadolinium is used to compare different models for fitting T1 relaxation. Furthermore, this chapter explores different data analysis methods in order to further process the data obtained from a single T1 experiment. The models we established are applied to better understand the Fenton like reaction of copper in **chapter 3**. Additionally, as FNDs can be incorporated into different materials, they can be used to study material properties of these specific materials. In **chapter 4** FNDs were incorporated into a polymer film to quantify the degradation speed. Here, a degradation solution containing gadolinium was used to degrade the film while T1 measurements were used to quantify the degradation speed. In **chapter 5** FNDs were used in cells to assess the free radical production upon a viral infection. Besides tracking the change in T1, the fate of the FND within both healthy and infected cells was studied. Lastly, **chapter 6** will discuss the importance of each work presented in this thesis and look at potential further options within the different aspects of the studies.

References

1. Gracio JJ, Fan QH, Madaleno JC. Diamond growth by chemical vapour deposition. *J Phys D Appl Phys*. 2010;43(37). doi:10.1088/0022-3727/43/37/374017

2. Williams OA, Nesladek M, Daenen M, et al. Growth, electronic properties and applications of nanodiamond. *Diam Relat Mater*. 2008;17(7-10):1080-1088. doi:10.1016/j.diamond.2008.01.103

3. Yang W, Butler JE, Russell JN, Hamers RJ. Direct electrical detection of antigen-antibody binding on diamond and silicon substrates using electrical impedance spectroscopy. *Analyst*. 2007;132(4):296-306. doi:10.1039/b612201a

4. Sun B, Baker SE, Butler JE, et al. Covalent molecular functionalization of diamond thin-film transistors. *Diam Relat Mater*. 2007;16(8):1608-1615. doi:10.1016/j.diamond.2007.02.004

5. Krueger A. Diamond nanoparticles: Jewels for chemistry and physics. *Adv Mater*. 2008;20(12):2445-2449. doi:10.1002/adma.200701856

6. Vaijayanthimala V, Tzeng YK, Chang HC, Li CL. The biocompatibility of fluorescent nanodiamonds and their mechanism of cellular uptake. *Nanotechnology*. 2009;20(42). doi:10.1088/0957-4484/20/42/425103

7. Chen YC, Lee DC, Hsiao CY, et al. The effect of ultra-nanocrystalline diamond films on the proliferation and differentiation of neural stem cells. *Biomaterials*. 2009;30(20):3428-3435. doi:10.1016/j.biomaterials.2009.03.058

8. Zhang XQ, Lam R, Xu X, Chow EK, Kim HJ, Ho D. Multimodal nanodiamond drug delivery carriers for selective targeting, imaging, and enhanced chemotherapeutic efficacy. *Adv Mater*. 2011;23(41):4770-4775. doi:10.1002/adma.201102263

9. Xi G, Robinson E, Mania-Farnell B, et al. Convection-enhanced delivery of nanodiamond drug delivery platforms for intracranial tumor treatment. *Nanomedicine Nanotechnology, Biol Med*. 2014;10(2):381-391. doi:10.1016/j.nano.2013.07.013

10. Doherty MW, Manson NB, Delaney P, Jelezko F, Wrachtrup J, Hollenberg LCL. The nitrogen-vacancy colour centre in diamond.

Phys Rep. 2013;528(1):1-45. doi:10.1016/j.physrep.2013.02.001

11. Pham-Huy LA, He H, Pham-Huy C. Free radicals, antioxidants in disease and health. *Int J Biomed Sci*. 2008;4(2):89-96.

12. Griendling KK, Touyz RM, Zweier JL, et al. *Measurement of Reactive Oxygen Species, Reactive Nitrogen Species, and Redox-Dependent Signaling in the Cardiovascular System: A Scientific Statement from the American Heart Association*. Vol 119.; 2016. doi:10.1161/RES.0000000000000110

13. Ho KO, Leung MY, Pang YY, Wong KC, Ng PH, Yang S. In Situ Studies of Stress Environment in Amorphous Solids Using Negatively Charged Nitrogen Vacancy (NV-) Centers in Nanodiamond. *ACS Appl Polym Mater*. 2021;3(1):162-170. doi:10.1021/acsapm.0c00964

14. Kolkowitz S, Safira A, High AA, et al. Probing Johnson noise and ballistic transport in normal metals with a single-spin qubit. *Science (80-)*. 2015;347(6226):1129-1132. doi:10.1126/science.aaa4298

15. Tetienne JP, Dontschuk N, Broadway DA, Stacey A, Simpson DA, Hollenberg LCL. Quantum imaging of current flow in graphene. *Sci Adv*. 2017;3(4). doi:10.1126/sciadv.1602429

16. Rosskopf T, Dussaux A, Ohashi K, et al. Investigation of surface magnetic noise by shallow spins in diamond. *Phys Rev Lett*. 2014;112(14):1-5. doi:10.1103/PhysRevLett.112.147602

17. Perona Martínez F, Nusantara AC, Chipaux M, Padamati SK, Schirhagl R. Nanodiamond Relaxometry-Based Detection of Free-Radical Species When Produced in Chemical Reactions in Biologically Relevant Conditions. *ACS Sensors*. 2020;5(12):3862-3869. doi:10.1021/acssensors.0c01037

18. Chipaux M, van der Laan KJ, Hemelaar SR, Hasani M, Zheng T, Schirhagl R. Nanodiamonds and Their Applications in Cells. *Small*. 2018;14(24):1-25. doi:10.1002/smll.201704263

19. Claveau S, Bertrand JR, Treussart F. Fluorescent nanodiamond applications for cellular process sensing and cell tracking. *Micromachines*. 2018;9(5):1-13. doi:10.3390/mi9050247

20. Fu C, Lee H, Chen K, et al. Characterization and application of single fluorescent nanodiamonds as cellular biomarkers. *PNAS*.

2007;104(3):727-732. doi:10.1073/pnas.0605409104

21. Liu KK, Cheng CL, Chang CC, Chao JI. Biocompatible and detectable carboxylated nanodiamond on human cell. *Nanotechnology*. 2007;18(32). doi:10.1088/0957-4484/18/32/325102

22. Aversa R, Petrescu RV V., Apicella A, Petrescu FIT. Nano-diamond hybrid materials for structural biomedical application. *Am J Biochem Biotechnol*. 2017;13(1):34-41. doi:10.3844/ajbbsp.2017.34.41

23. Lazda R, Busaite L, Berzins A, et al. Cross-relaxation studies with optically detected magnetic resonances in nitrogen-vacancy centers in diamond in external magnetic field. *Phys Rev B*. 2021;103(13):134104. doi:10.1103/PhysRevB.103.134104

Chapter 2

Optimising data processing for nanodiamond based relaxometry

Thea A. Vedelaar[1], Thamir H. Hamoh[1], Felipe P. Perona Martinez[1], Viraj G. Damle[1], Mayeul Chipaux[*,2], Romana Schirhagl[*,1]

1 Groningen University, University Medical Center Groningen, Antonius Deusinglaan 1, 9713 AW.

2 Institute of Physics, École Polytechnique Fédérale de Lausanne (EPFL), CH-1015 Lausanne, Switzerland

** mayeul.chipaux@epfl.ch ; romana.schirhagl@gmail.com*

Abstract

The negatively charged nitrogen-vacancy (NV) center in diamond has emerged as a powerful and versatile quantum sensor for diverse quantities. In particular, all-optical diamond based relaxometry (or T1), which consists of monitoring the NV centers' photoluminescence submitted to a train of green laser pulses, allows to detect magnetic noise and its origin. When applied on diamond nanoparticles, it allows nanoscale resolution and has many applications in biology, for monitoring chemical reactions metabolic activity or diagnostic markers. While increasing the number of NV centers in a nanodiamond allows to collect more signal, a standardized method to extract information from relaxometry experiments of such NV ensembles is still missing. In this article, we use a set of T1 relaxation curves acquired at different concentrations of gadolinium ions to calibrate and optimize the entire data processing flow, from the acquired raw data to the extracted T1. In particular, we use a bootstrap to derive a signal to noise ratio that can be quantitatively compared from one method to another. At first, T1 curves are extracted from photoluminescence pulses. We compare integrating their signal through an optimized window as performed conventionally, to fitting a known function on it. Fitting the decaying T1 curves allows to obtain the relevant T1 value. We compared here the three most commonly used fit models that are, single, bi, and stretched-exponential. We finally investigated the effect of the bootstrap itself on the precision of the result as well as the use of a rolling window to allows time-resolution.

2.1 Introduction

Diamond based quantum sensing methods have gained attention over the last few years. Through Optically Detected Magnetic Resonance (ODMR)[1] the negatively charged Nitrogen-Vacancy defect in diamond (hereafter called NV center) possesses fluorescence properties which depend on the surrounding magnetic field[2]. Working at room temperature[2,3] and allowing for nanoscale resolution[4–7] it offers many tremendous experimental assets[8] as well as unprecedented sensitivity[9–11] for sensing variables like temperature[12,13], pH [14,15], strain[16], electric[17] or magnetic fields[4,18], microwave signals[19–21] and electrical current[22].

Among the NV based sensing methods, T1 relaxometry enables sensing magnetic noise without any microwave excitation[23]. As described in **Figure 1(a)**, a pulse of light initializes the NV center's electron spin into its the bright ($m_s = 0$) state. Another pulse, applied after different delays (or dark times, τ), probes the proportion of NV^- centers which have returned to a darker equilibrium between $m_s = 0,\ +1$ or -1 states. The time this process takes is called relaxation time or T1, which, as initially observed in Tetienne *et al.*[23] and further quantified in Rollo *et al.*[24], is shortened by magnetic noise. The method was originally used to detect spin labels such as gadolinium ions[23,25,26] or to monitor chemical reactions[15,27,28]. In our group, T1 relaxometry has turned out to be particularly useful for measuring free-radicals (chemicals with unpaired electrons) that are generated by the metabolism of individual cells[29–31].

The relaxometry curve for a single NV-center is well understood and can be fitted by a single exponential model[24]. Using a larger amount of NV centers allows to significantly increase the photoluminescent signal. However, the summation of the signals from different NV centers in varying magnetic environment renders the situation more complex. While few fitting models like the single exponential[32–37], bi-exponential[28–31,38] and the stretched exponential[39–41] decays are often use to analyze such data, there is no clear consensus on which is to be used under different circumstances.

In this work, we use the acquisition procedure developed in[28] with predefined laser intensity and pulse duration. Applying it on a set of 8 nanodiamond submitted to different gadolinium concentrations, we

acquired a calibration data set that we used to systematically compare different ways to extract data from to optimize the whole data processing flow. In particular, we investigate how to best extract the data from the raw photoluminescence pulse train. We then quantitatively compare the three fitting models. To that end, we use a bootstrap approach to obtain a signal to noise ratio that can be directly compared between the different methods. We also investigate the effect of the bootstrap itself on the result precision as well as the use of a rolling window to obtain temporal information.

2.2 Materials and methods

2.2.1 Experimental details

Sample

We use gadolinium ions (in the form of $GdCl_3$ in solution) which is a common contrast agent in MRI for magnetic noise to lower T1 in a controlled manner. We use oxygen terminated nanodiamonds with hydrodynamic diameter of 70 nm (Adamas Nanotechnology), identical to the ones used in our intracellular experiments[29–31]. To perform a measurement, we first allow the nanodiamonds to attach to a petri dish cover glass before filling it with water. Gadolinium (Gd) solution is then added such that the concentration is increased step wise from 1nM up to 100mM.

T1 protocol

One diamond nanoparticle is first identified with our homemade confocal microscope. A set of T1 measurements is acquired on that same nanoparticle for each Gd^{3+} concentration. Our previously developed T1 measurement protocol[28] (see Fig 1 (a)) consists of a train of 51 laser pulses (532 nm, of (8 mW/μm^2)) lasting $5\ \mu s$ each, intermitted by 50 dark times exponentially varied from $200\ \mathrm{ns}$ to $10\ \mathrm{ms}$. During that sequence, the times at which each photon is detected is stored. We call one execution of a whole sequence of $N_{pulses} = 51$ pulses an observation.

Averaging

A single observation is too noisy to extract any relevant information. A measurement sequence (Fig. 1(b)) consists of $N_{obs} = 10^4$ observations acquired on the same particle at each concentration. Those

observations are then aggregated either altogether (See Fig. 1(b)), through a bootstrap (Fig. 2(a)) or a rolling window aggregation (Fig. 2(b)) (Detailed in Sec. 2.4). A photoluminescence pulse train is obtained by counting, how many photons are detected at each instant of the pulse sequence (Fig. 1(a)) over all the aggregated observations. Each of the photoluminescence pulses of the train is extracted and isolated such as presented in (Fig. 1(c))[38]. As described in Sec. 2.2 a T1 relaxation curve (Fig. 1(d)) is extracted from the first microsecond of each pulse as a function of the preceding dark time. The relevant T1 is obtained by fitting a decaying curve (see Sec. 2.3).

This whole process has been reproduced independently on $N_{part} = 8$ different nanoparticles, each submitted to all the investigated Gd^{3+} concentrations.

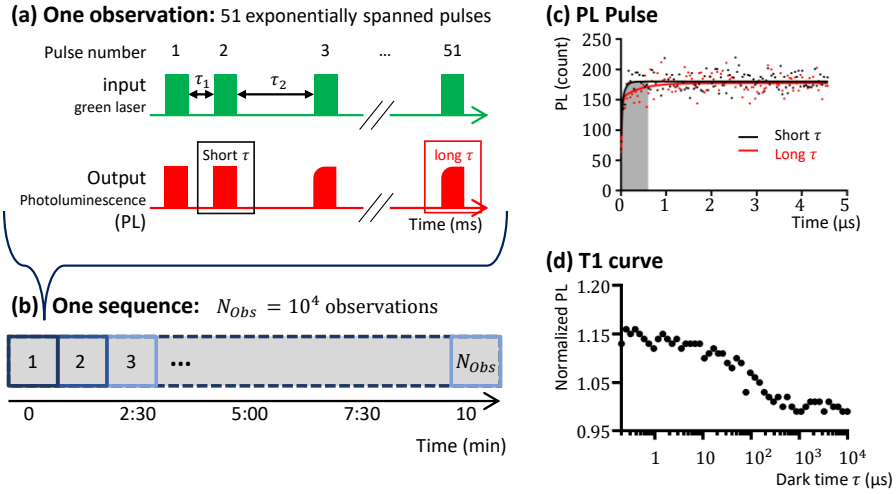

Figure 1 Principle of T_1 measurements: *(a) An observation consists of applying a train of 51 laser pulses (532 nm, of (8* mW/µm^2*)) of* 5 µs *each, used both to initialize the and readout the NV center spin state. The 50 darktimes τ between them are exponentially spanned from* 0.2 *up to* 10^4 *µs. Each received photon is timestamped with respect to the laser pulse. (b) each measurement sequence is made of $N_{acq} = 10^4$ successive observations (c) The pulses starting from the second onward are used to determine the T1 by summing the total number of photons received at each timepoint either through the whole N_{Acq} or through the bootstrap or rolling window methods. The black dots indicate the pulse succeeding a dark time of* 0.4 *µs and the red dots a dark time of* 6.8 *µs. The intensities of the pulses are integrated over the read window or through pulse fitting. (d) The T1 relaxation curve is obtained either by integrating the first* 0.6 *µs of each pulse, or through fitting Eq. 1 on it. The photoluminescence is normalized to 1 by dividing by I_∞ obtained from the fit of the Eq. 2, 3 or 4.*

2.2.2 Pulse reading

Given the laser power density we apply on the sample, the photoluminescence pulses typically differ only within the few first microseconds.

The photoluminescence signal of a T1 curve can be obtained by integrating the photoluminescence pulses over an optimized window. We use here the first 0.6 µs as previously determined in[28].

Alternatively, the photoluminescence can be fitted with eq 1, adapted from[42], which models an ensemble of NV^- centers.

$$I(t) = A_1\left(1 - e^{-k_1 t}\right) + A_2\left(1 - e^{-k_2 t}\right) \quad (1)$$

Here t is the time after the beginning of the pulse. A_1 and A_2 are related to the different populations in the $m_s = 0$ and $m_s = \pm 1$ states and k_1 and k_2 are parameters that include but are not limited to the laser power and relaxation rates for the different spin states. To obtain a directly comparable T1 curve, the obtained fitted function is integrating the first $0.6\ \mu s$.

2.2.3 Extraction of T1 dynamics

Information about the dynamics of the spin relaxation is obtained from the relaxation curve in the form of a T1 time resulting from a fit. We compared different commonly used fit models including single exponential[32–34], bi-exponential[37–39] and stretched exponential[39–41]. In any case, τ is the dark time between pulses.

The simplest investigated model is a single exponential decay (Eq. 2). Applied on an ensemble, it computes a global relaxation time of the average of all NV^- centers.

$$I(t) = I_\infty\left(1 + C_1 \mathrm{e}^{-\tau/\mathrm{T}_1}\right) \quad (2)$$

I_∞ is the average intensity over all spin states. C_1 is the normalized difference between the photoluminescent intensity of the initial $m_s = 0$ state $I_\infty(1 + C_1)$ state and the one of final thermal equilibrium I_∞.

As empirically found[28], the T1 relaxation curves are often well fitted by a bi-exponential model (Eq. 3) comprising a short T_S and a long T_L component. The shorter is in the range of a few microseconds, the longer is of about a few hundreds of microseconds.

$$I(\tau) = I_\infty\left(1 + C_S e^{-\tau/T_s} + C_L\, e^{-\tau/T_L}\right) (3)$$

The final model is the stretched exponential in which an additional exponent (β) ranging from 0 to 1[43] (Eq. 4). This way, the obtained T1 constitutes the global relaxation time of the system.

$$I(\tau) = I_\infty\left(1 + C_2 e^{-(\tau/T_1)^\beta}\right) \quad (4)$$

2.2.4 Data aggregation: Generation of the raw photoluminescence pulse train

Bootstrap

As commonly applied in both medical sciences and signal processing, our data was aggregated using a bootstrap[44]. This method allows to infer the probability density for the fitted parameter[45], derive its maximum likelihood, and a standard deviation (see below).

The basic principle of bootstrap is to resample the whole data set over randomly chosen observations considered independently from one another (see **Figure 2(a)** and **Table 1**). A subset of N_{Sub} randomly chosen observations are combined allowing each observation to be chosen more than once. In our case, $N_{sub} = 10^4$ (same as N_{acq}). T1 is then obtained as described in Sec. 2.2 and 2.3.

To obtain the probability density of T_1 this procedure is repeated N_{boot} times, until a desirable confidence is achieved (or limited by the total number of combination if N_{acq} is small). In our case, $N_{boot} = 10^4$ resulting in 10^4 different values for T_1 constituting the probability density using the Kernel Density Estimate (KDE) or Parzen-Rosenblatt window[46]. The kernel was based on the one developed by Botev et al[46] which is based on diffusion equations. The KDE transfers the continuous values into a smooth distribution with a total integral of 1 from which the most likely T1 or contrast values and their confidence interval.

***Table 1**. Step wise procedure for a bootstrap process.*

Bootstrap process	
Select N_{sub} observations randomly among the N_{acq} allowing to select the same measurement multiple times*	$N_{acq} = 10^4$ $N_{sub} = 10^4$
Reconstruct the T1 measurement based on the selected repetitions	
Compute the T1 value from the resulting curve	
Repeat step 1-4 N_{boot} times to obtain the bootstrap samples	$N_{boot} = 10^4$
Apply kernel density approximation	
Compute the applicable statistical properties	

*the observations are selected randomly, without excluding the ones already selected.

Rolling window:

To observe the temporal evolution of T1 over the total duration of acquisition, a rolling window (or rolling average) can be applied. This process, often used in econometric studies[47], is schematically presented in figure 3. While we previously used the entire N_{acq} repetitions (which are collected within about 10 min) to compute one T1 value, we here attempt to further divide the measurement to gain time resolution. To perform a rolling window the first T1 was computed for a defined number of repetitions (here 1 to 7000). Afterwards the window was moved by 10 repetitions (this is called shift) and the second T1 was computed for observation 11 to 7010. The window was moved again and this was repeated until the window for the final T1 was computed up to the final repetition. The steps that are needed to perform a rolling window are shown in table 2.

Table 2. *The rolling window process.*

Rolling window process
Select a window size and a shift size
Reconstruct the T1 measurement in the window
Compute the T1 for this window
Move the window by the shift size
Repeat steps 2-4 until the window ends at the last repetition

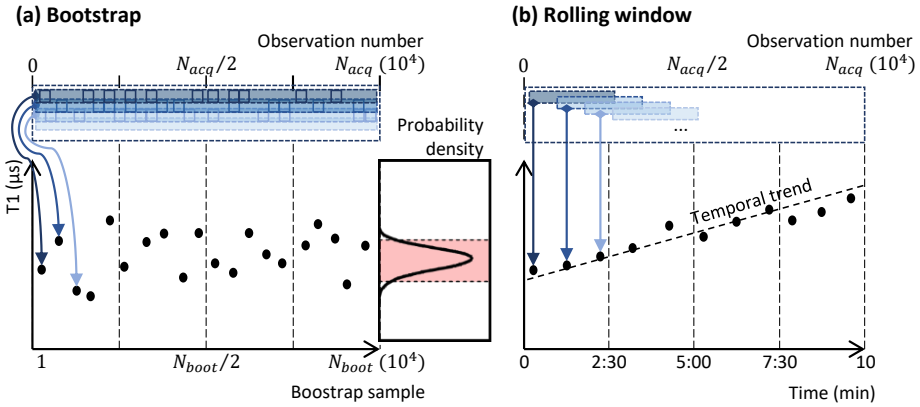

Figure 2: Data aggregation *(a) Bootstrap: A subset of the N_{Sub} observations is randomly chosen to calculate a T1 value. This process is repeated N_{Boot} times to obtain the same amount of T1 values, from which a T1 probability density can be obtained. (b) Rolling window: We first generate a T1 from the first N_{Width} observations. We then move the window by N_{step} observations to generate the next T1. This process is repeated until the entire dataset is processed to infer a temporal evolution.*

2.2.5 Signal to noise ratio calculation

In case the bootstrap cannot be applied, (Section 3.3, Fig. 5), the signal S is obtained for each concentration by taking the absolute value of the subtraction of the T1 obtained at that concentration to the one in the water condition, averaged over 8 particles. The noise is taken from the standard deviation over the 8 particles. However, this value includes both the T1 estimation error made by the fit methods and the initial T1 dispersion. Since the second is much larger than the first[28], the ability to discriminate different concentrations is significantly masked by the dispersion of the initial T1 value.

The role of the bootstrap is therefore to place the randomization on the selection of the observation when using a particle rather than on selecting that particles. It therefore allows to derive statistics on the effect of the measurement method itself. In case it can be applied, (Sec. 3.1 and 3.2, Fig 3, 4), a signal S is taken from the T1 of maximum of likelihood as obtained by the bootstrap (absolute value of the subtraction to the one of the water condition). The noise N is also taken from the standard deviation obtain from the bootstrap at the considered concentration. Both the signal and noise are averaged over the 8 different particles.

2.3 Results and Discussions

2.3.1 Pulse fitting

All pulses follow a general pattern shown in (**Figure 1(c)**). They start with a rapid build-up towards a steady value. The pulses succeeding longer dark times (red) reach the steady value slower than those after shorter ones (black). As described in Section 2.2, the pulses were either integrated over the read window (grey) or fitted with Eq. 1 to better take all the timepoints of the pulse into account and reduce the noise.

The difference between pulses is caused by the probability of the decay from the excited to the ground state via the metastable state which does not emit photons in the detected range[48,49]. When the decay goes through the metastable state, NV center's electrons are also shelved there for a few hundreds of nanosecond before they can cycle again[49,50]**.** Furthermore, the decay via the metastable state is more likely to occur for

electrons in the $m_S = \pm 1$ state[48,49]. These factors create the build-up in the pulses and are the basis of the spin readout of the NV^- center. A major variable in the polarization model is the excitation rate. Related to the laser intensity, it impacts k_1 and k_2 in equation 1 directly. While too low pumping does not allow to polarize the NV- center fast enough compared to the relaxation, too high energies may ionize the NV^-center to NV^0 [51,52]. In our case, the laser intensity was chosen to be safe for biological samples and kept constant between experiments[15,29–31].

The fit well captures the build-up to a saturated steady state (ranging up to ≈ 200 counts). Taking all datapoints into account, the pulse fit should reduce the total relative shot noise. The comparison between the resulting T1 curve obtained from particle 1 exposed to either $10\ \mathrm{nM}$ and $1\ \mathrm{mM}$, fitted with the bi-exponential model is shown in **Figure 3(a)**.

However, as observed in **Figure 3(b)** the signal to noise ratio is not significantly improved when the fit pulse is used. This highlights that at our laser power, the integration window is already well optimized.

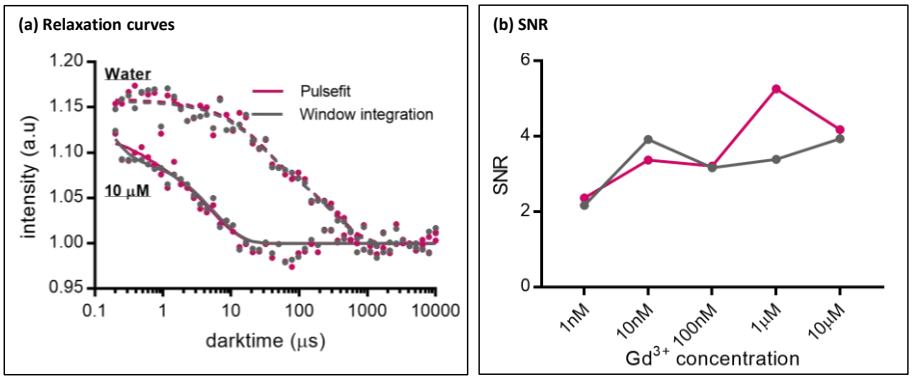

Figure 3: *(a) The T1 curves from particle 1 in water and $10\ \mu M$ 1 mM and 10 nM Gd^{3+} resulting from window integration (grey) and fitting with Eq. 1 (b) Signal to noise ratio as defined in Sec. 2.5.*

2.3.2 Exponential fits

We compare the performance of the three different models in differentiating known concentrations of Gd^{3+}. Each of these models have their origin in the population dynamics of the NV^- center. The most important parameters are the difference in intensity between the $m_S = 0$ and $m_S = \pm 1$ and the transition rate between these states (expressed in the T1). The single exponential model depicted in Eq. 2 can be naturally derived from the spin relaxation decay dynamics of individual NV center [23].

Extending the model to ensembles starts with considering that each NV center has different T1 times. These depend on their orientation and distance to the surface of the nanodiamond[31], the number and proximity of both paramagnetic species and dangling bonds on the surface[36] and nitrogen and ^{13}C within the diamond. As a result, each NV center feels a slightly different magnetic noise intensity. The relaxation curve obtained from an ensemble is therefore the sum off all those contributions. However, the number of NV centers vary for each nanodiamond and fitting over many variables reduces the precision of the fit and complicates the calculation.

As shown in[43] such a sum over the different T1 can be modeled with a stretched exponential depicted in Eq. 4. This reduces the number of fitted parameters to four.

Alternatively, it has been found empirically[28–30,37] that a bi-exponential decay may fit the data well. While the long-time component has been associated to spin relaxation, the origin of the short one remains uncertain. For instance, the laser pumping can induce charge transfer, altering the charge state of the NV centers and the photoluminescence we collect, while the dark time allows it to relax to equilibrium[15,53,54]. Nevertheless, we evidenced in previous work[28] that the longer time constant varies most sensitively with the concentration of samples' than the shorter one.

The fits of these three models on typical T1 relaxation curves are presented in **Figure 4 (a)**. It corresponds to the first observed particle exposed to 1 and 100 nM Gd^{3+}.

A first measure of the performance of the fits can be read through their residuals which considers the total average squared error made by the fit with respect to the original data. The residuals, averaged over the 8 particles obtained from those fits is presented in the inset of **Figure 4 (a)**. At first, it confirms that the bi and stretched exponential decaying models render the situation better than the single exponential one. Despite a clear first shoulder corresponding to the short relaxation decay is often observed subjectively, the stretch and bi exponential's residuals turned out to be quite similar. We could also observe that, weight associated to each decay depends on the nanodiamond, or the Gd concentration. When the last is too high, or for certain particles, only the longer decay persists. In such a case the bi-exponential fit approaches the single or stretched exponential ones.

The degree to which the models explain the difference in T1 as caused by changes in concentration rather than random noise can be measured by computing the signal to noise ratio (SNR) (see Sec. 2.4). Higher SNR implies that a change in concentration induces better visible difference in the signal with respect to the noise.

Figure 4(b) depicts the most likely T1 values and the standard deviations obtained from the bootstrap at each Gd^{3+} concentrations, both cases averaged over the 8 different particles. **Figure 4(c)** shows the obtained signal to noise ratio as defined in Sec. 2.5. For the lower concentrations (1 and 10 nM Gd^{3+}), the bi- and stretched-exponentials are significantly more sensitive than the single exponential one. While the bi-exponential has also slightly higher standard deviation, the steepness of the concentration dependency outweighs this disadvantage.

For higher concentrations however, the error bars linked to the bi-exponential fit increases. With more fitted parameters, and when the two time constants T_S and T_L get closer, we observe that the fitting procedure may exchange the role of the two, or eventually combine them into a unique exponential decay. While this fit data similarly well, this may render the fit result less predictable.

Nonetheless, our analysis notably confirms that for most of biologically relevant cases i.e. when the T1 is larger than 100 μs, the widely used bi-exponential fit remains well suited.

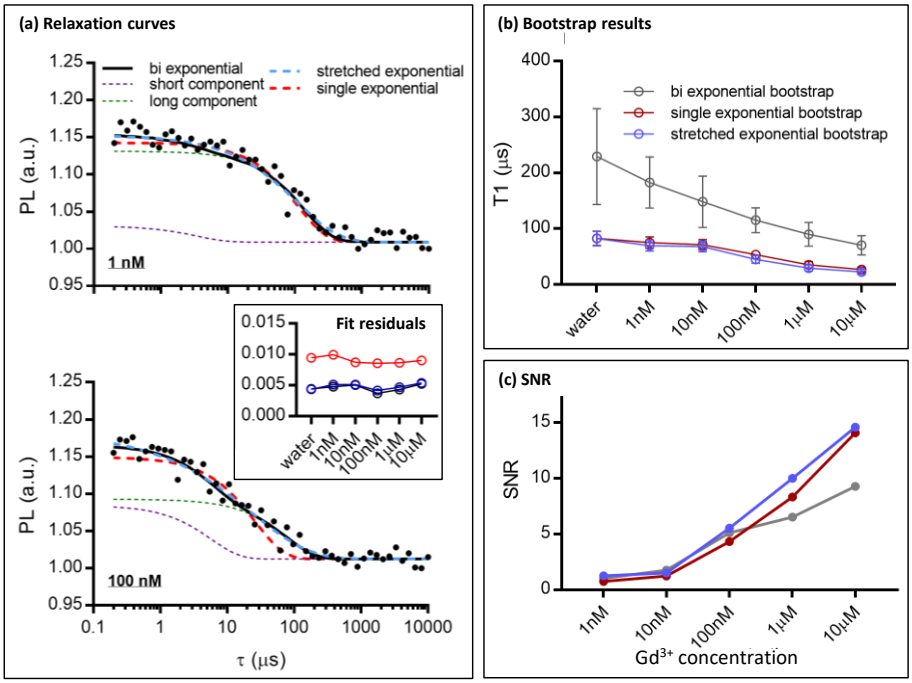

Figure 4: *(a) Fitted single and bi exponential model for 2 different concentrations of* Gd^{3+}*.* $1\ nM$ *(top) and* $100\ nM$ *bottom. The black dots represent the results of the measurement. The figure shows fits for the bi exponential model (solid black), single exponential model (dashed red) and stretched exponential (dashed blue) and the long (green dashed) and short (purple dashed) components of the bi-exponential fits. (b) T1 most likely value (line) and noise N (error bars) as derived by the bootstrap, (c) Signal to noise ratio as defined in Sec. 2.5.*

2.3.3 Bootstrap

While the bootstrap can be used to compare the different fit model, it can also be applied on the raw data to determine the most likely T1. The idea behind is that some outlier observations may not to be considered in a random manner such that the obtained most likely value can be more robust than the direct fit. Since the bootstrap cannot be used on data that has already processed with a bootstrap, we compare in **Figure 5** the fit results taken over all observation to the most likely value obtained from the bootstrap, for both the stretched and bi exponential model. The uncertainty is obtained each time from the standard deviation observed over the 8 different particles at the considered Gd^{3+} concentration. (See Sec. 2.5)

While the T1 values remain quite similar when using the bootstrap, the method did not lead to any improvement. First, it is to be noted that the standard deviations are taken from the 8 different particles. They are therefore significantly enlarged by the initial T1 dispersion. Furthermore, the bootstrap selects observations independently from one another. This both allows to take each observation more than once but also not to take some observations at all. Although both the direct fit and bootstrap take the same amount of observations in total $\left(N_{Sub} = N_{Acq} = 10^4\right)$, the number of them that are independent from one another is lower in the bootstrap than in the direct fit. This therefore reduces the averaging and increases the relative noise in the T1 curve and so on the fitted T1. It appears that this is not compensated by allowing potential outlier observations to be ignored.

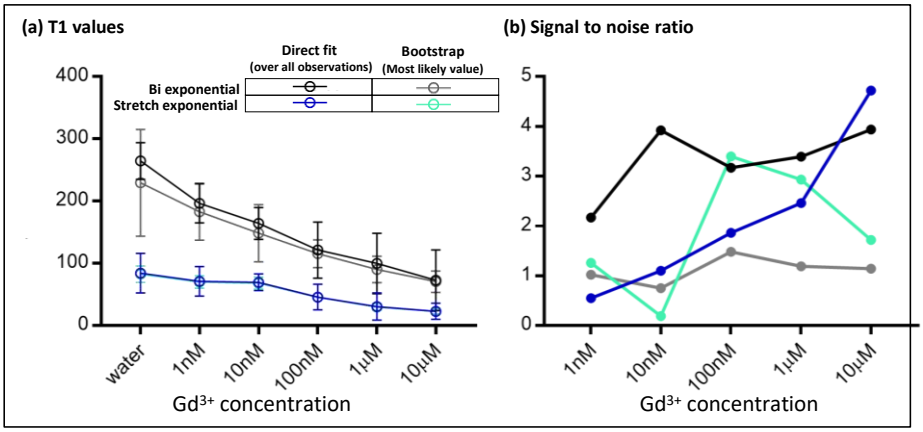

Figure 5: *(a) T1 values obtained by fitting all the observation at once or taking the most likely value from the bootstrap. The errorbars correspond to the standard deviation calculated over the 8 particles. (b) Signal to noise ratio as defined in Sec. 2.5*

2.3.4 Rolling window

While the previous methods aim to detect a concentration that is constant within one measurement, we here attempt to improve time resolution. To this end we created a measurement consisting of three Gd^{3+} concentrations: water (0nM), 10nM and 1µM (1000nM) by selecting more or less observations related to each case. In particular, the number of selected observations corresponding the Gd^{3+} concentrations are linearly changed in the pink and green areas. This means that the T1 should be high in the beginning of the measurement and low at the end. The rolling window (shown in figure 7) used 7000 repetitions with a shift of 10.

This window was intentionally moved over the different concentrations. This simulates a case where we do not know when a concentration change occurs. The most important consideration for chosing the right parameters for a rolling window is the window's size. If the timescale of the expected changes is known this can be used as a guideline for selecting the window size. However, when lowering the window size, we have to consider that each resulting T1 value is then based on a smaller number of repetitions (for a optimization of this parameter see supplementary information).

The rolling window acts as a longpass filter. A too long rolling window would average out changes on short time scales. Oppositely, a too short window will lead to unreliable results. Overall, the window size has to be optimized per set of experiments. In our case, we observed that bellow 7000 observations, the fits are becoming less stable, which reduces the accuracy of the fit.

The points in the purple and green areas of figure 7 are composed of data from two different concentrations. The T1 value in each point can be predicted by using the average T1 value of the rolling window of each measurement with a size of 7000. The concentration prediction is then made by calculating the proportion of each measurement in each point and computing the average T1 based on these proportions. The predicted values are shown in Figure 7 with the dotted lines with different colors representing the different models (black: bi-exponential, red: single exponential, blue: stretched exponential). Figure 7 shows that all exponential models follow the predicted curve very well.

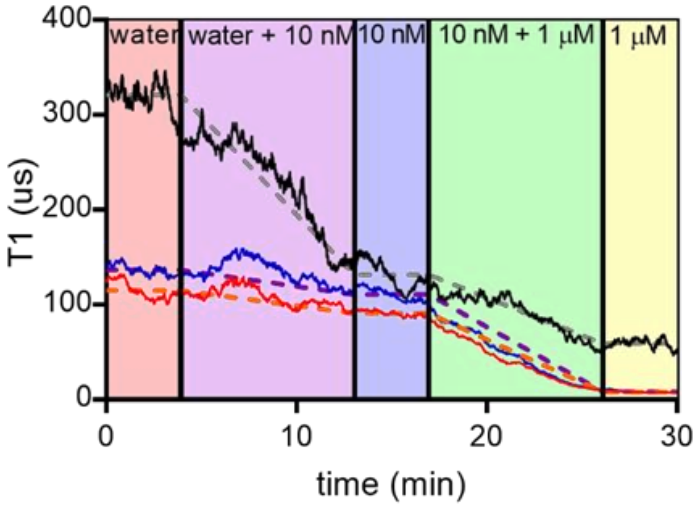

Figure 6: *The rolling window of 3 measurements for different concentrations. Each window consisted of 7000 repetitions and are shifted by 10 for each sequential point. The solid lines represent the T1 values computed for each point of the figure for the different models; bi- (black), single (red) and stretched (blue) exponentials. The colored blocks represent where each calculation consisted of which concentration (purple for water and 10nM, green for 10nM and 1μM). The dotted lines represent the T1 value obtained from the average of a rolling window of 7000 and are used to represent the average T1 for one specific concentration.*

2.4 Conclusion

In this paper we compared different methods to analyze T1 data: single, bi- and stretched exponential models. These are the most commonly used models to fit the T1 curve. We presented pulse fitting and bootstrap to remove noise from T1 data. Lastly, we showed the rolling window method for improving the temporal resolution of the measurement. We compared all these methods based on a calibration dataset which uses NV^- centers in diamond to measure different concentrations of gadolinium. We demonstrated that all models and methods can be applied successfully to this data.

By using a bootstrap, we showed that the stretched and bi-exponential fit models are better in differentiating between concentrations, with a preference for the stretched one at higher Gd^{3+} concentrations. For

lower concentrations, the bi-exponential has larger variation between measurements, but is also more sensitive to concentration changes. The T1 resulting from the stretched exponential remains very similar to the single exponential but appears to be more predictable. Furthermore, the fit quality, for the bi and stretched exponentials, are significantly better than for single exponential. However, when selecting the best model for the data, the experimental design should be a leading factor as well. While we investigated here nanodiamond with NV centers ensemble, the single exponential model may still be best for single NV^- centers.

We also presented two alternative methods to compute the T1 from the measurement. The first is based on modelling the pulses from the pulse train. While the output T1 remain unchanged, the measurement quality is not improved in term of signal to noise ratio. This it might be useful in datasets of worse quality, or when the optimized integration window is not known.

The second concerns the use of the bootstrap to improve the quality of an output T1. Either masked by initial T1 dispersion, or due to plausible limitations that we identified, we could not observe significant improvement here as well.

Lastly, the rolling window was used to show temporal information on the T1. We showed that, in this case, each model renders the decrease in T1 with increasing concentrations rather well. While the T1 is “noisy” as the rolling window moves, the changes induced by combining different Gd^{3+} concentration is larger.

References

1. Suter, D. Optical detection of magnetic resonance. *Magn. Reson.* **1**, 115–139 (2020).

2. Gruber, A. *et al.* Scanning confocal optical microscopy and magnetic resonance on single defect centers. *Science (80-.).* **276**, 2012–2014 (1997).

3. Balasubramanian, G. *et al.* Nanoscale imaging magnetometry with diamond spins under ambient conditions. *Nature* **455**, 648–651 (2008).

4. Maze, J. R. *et al.* Nanoscale magnetic sensing with an individual electronic spin in diamond. *Nature* **455**, 644–647 (2008).

5. Pham, L. M. *et al.* Magnetic field imaging with nitrogen-vacancy ensembles. *New J. Phys.* **13**, (2011).

6. Steinert, S. *et al.* High sensitivity magnetic imaging using an array of spins in diamond. *Rev. Sci. Instrum.* **81**, 1–6 (2010).

7. Chipaux, M. *et al.* Magnetic imaging with an ensemble of nitrogen vacancy-centers in diamond. *Eur. Phys. J. D* **69**, 1–10 (2015).

8. Babashah, H. *et al.* Optically detected magnetic resonance with an open source platform. 1–25 (2022).

9. Grinolds, M. S. *et al.* Nanoscale magnetic imaging of a single electron spin under ambient conditions. *Nat. Phys.* **9**, 215–219 (2013).

10. Mamin, H. J. *et al.* Nanoscale magnetic imaging of a single electron spin under ambient conditions. *Science (80-.).* **339(6119)**, 557–560 (2013).

11. Cujia, K. S., Boss, J. M., Herb, K., Zopes, J. & Degen, C. L. Tracking the precession of single nuclear spins by weak measurements. *Nature* **571**, 230–233 (2019).

12. Choi, J. *et al.* Probing and manipulating embryogenesis via nanoscale thermometry and temperature control. *Proc. Natl. Acad. Sci. U. S. A.* **117**, 14636–14641 (2020).

13. Yukawa, H. *et al.* A quantum thermometric sensing and analysis system using fluorescent nanodiamonds for the evaluation of living stem

cell functions according to intracellular temperature. *Nanoscale Adv.* **2**, 1859–1868 (2020).

14. Fujiwara, M. *et al.* Monitoring spin coherence of single nitrogen-vacancy centers in nanodiamonds during pH changes in aqueous buffer solutions. *RSC Adv.* **9**, 12606–12614 (2019).

15. Rendler, T. *et al.* Optical imaging of localized chemical events using programmable diamond quantum nanosensors. *Nat. Commun.* **8**, (2017).

16. Ho, K. O. *et al.* In Situ Studies of Stress Environment in Amorphous Solids Using Negatively Charged Nitrogen Vacancy (NV-) Centers in Nanodiamond. *ACS Appl. Polym. Mater.* **3**, 162–170 (2021).

17. Kolkowitz, S. *et al.* Probing Johnson noise and ballistic transport in normal metals with a single-spin qubit. *Science (80-.).* **347**, 1129–1132 (2015).

18. Hong, S. *et al.* Nanoscale magnetometry with NV centers in diamond. *MRS Bull.* **38**, 155–161 (2013).

19. Chipaux, M. *et al.* Wide bandwidth instantaneous radio frequency spectrum analyzer based on nitrogen vacancy centers in diamond. *Appl. Phys. Lett.* **107**, (2015).

20. Dolde, F. *et al.* Electric-field sensing using single diamond spins. *Nat. Phys.* **7**, 459–463 (2011).

21. Meinel, J. *et al.* Heterodyne sensing of microwaves with a quantum sensor. *Nat. Commun.* **12**, 1–8 (2021).

22. Nowodzinski, A. *et al.* Nitrogen-Vacancy centers in diamond for current imaging at the redistributive layer level of Integrated Circuits. *Microelectron. Reliab.* **55**, 1549–1553 (2015).

23. Tetienne, J. P. *et al.* Spin relaxometry of single nitrogen-vacancy defects in diamond nanocrystals for magnetic noise sensing. *Phys. Rev. B - Condens. Matter Mater. Phys.* **87**, 1–5 (2013).

24. Rollo, M. *et al.* Quantitative study of the response of a single NV defect in diamond to magnetic noise. *Phys. Rev. B* **103**, 1–5 (2021).

25. Kaufmanna, S. *et al.* Detection of atomic spin labels in a lipid bilayer using a single-spin nanodiamond probe. *Proc. Natl. Acad. Sci. U. S. A.* **110**, 10894–10898 (2013).

26. Sushkov, A. O. *et al.* All-optical sensing of a single-molecule electron spin. *Nano Lett.* **14**, 6443–6448 (2014).

27. Barton, J. *et al.* Nanoscale dynamic readout of a chemical redox process using radicals coupled with nitrogen-vacancy centers in nanodiamonds. *ACS Nano* **14**, 12938–12950 (2020).

28. Perona Martínez, F., Nusantara, A. C., Chipaux, M., Padamati, S. K. & Schirhagl, R. Nanodiamond Relaxometry-Based Detection of Free-Radical Species When Produced in Chemical Reactions in Biologically Relevant Conditions. *ACS Sensors* **5**, 3862–3869 (2020).

29. Morita, A. *et al.* The fate of lipid-coated and uncoated fluorescent nanodiamonds during cell division in yeast. *Nanomaterials* **10**, 1–17 (2020).

30. Nie, L. *et al.* In press. *Nano Lett.* (2021).

31. Nie, L. *et al.* Quantum Sensing of Free Radicals in Primary Human Dendritic Cells. *Nano Lett.* **22**, 1818–1825 (2022).

32. Myers, B. A., Ariyaratne, A. & Jayich, A. C. B. Double-Quantum Spin-Relaxation Limits to Coherence of Near-Surface Nitrogen-Vacancy Centers. *Phys. Rev. Lett.* **118**, 1–7 (2017).

33. Giri, R. *et al.* Coupled charge and spin dynamics in high-density ensembles of nitrogen-vacancy centers in diamond. *Phys. Rev. B* **98**, 1–7 (2018).

34. Song, X. *et al.* A statistical correlation investigation for the role of surface spins to the spin relaxation of nitrogen vacancy centers. *AIP Adv.* **4**, (2014).

35. Jarmola, A., Acosta, V. M., Jensen, K., Chemerisov, S. & Budker, D. Temperature- and magnetic-field-dependent longitudinal spin relaxation in nitrogen-vacancy ensembles in diamond. *Phys. Rev. Lett.* **108**, 1–5 (2012).

36. Wood, J. D. A. *et al.* Wide-band nanoscale magnetic resonance spectroscopy using quantum relaxation of a single spin in diamond. *Phys. Rev. B* **94**, 1–20 (2016).

37. Rosskopf, T. *et al.* Investigation of surface magnetic noise by shallow spins in diamond. *Phys. Rev. Lett.* **112**, 1–5 (2014).

38. Steinert, S. *et al.* Magnetic spin imaging under ambient conditions with sub-cellular resolution. *Nat. Commun.* **4**, (2013).

39. Reineck, P. *et al.* Not All Fluorescent Nanodiamonds Are Created Equal: A Comparative Study. *Part. Part. Syst. Charact.* **36**, (2019).

40. Ariyaratne, A., Bluvstein, D., Myers, B. A. & Jayich, A. C. B. Nanoscale electrical conductivity imaging using a nitrogen-vacancy center in diamond. *Nat. Commun.* **9**, 1–7 (2018).

41. Choi, J. *et al.* Depolarization Dynamics in a Strongly Interacting Solid-State Spin Ensemble. *Phys. Rev. Lett.* **118**, 1–6 (2017).

42. Fuchs, G. D. *et al.* Excited-state spin coherence of a single nitrogen-vacancy centre in diamond. *Nat. Phys.* **6**, 668–672 (2010).

43. Johnston, D. C. Stretched exponential relaxation arising from a continuous sum of exponential decays. *Phys. Rev. B - Condens. Matter Mater. Phys.* **74**, 1–7 (2006).

44. Zoubir, A. M. & Iskandler, D. R. Bootstrap methods and applications. *IEEE Signal Process. Mag.* **24**, 10–19 (2007).

45. Efron, B. & Tibshirani, R. J. *No Title*. (1994).

46. Botev, Z. I., Grotowski, J. F. & Kroese, D. P. Kernel density estimation via diffusion. *Ann. Stat.* **38**, 2916–2957 (2010).

47. Inoue, A., Jin, L. & Rossi, B. Rolling window selection for out-of-sample forecasting with time-varying parameters. *J. Econom.* **196**, 55–67 (2017).

48. Hopper, D. A., Shulevitz, H. J. & Bassett, L. C. Spin readout techniques of the nitrogen-vacancy center in diamond. *Micromachines* **9**, 1–30 (2018).

49. Manson, N. B., Harrison, J. P. & Sellars, M. J. Nitrogen-vacancy center in diamond: Model of the electronic structure and associated dynamics. *Phys. Rev. B - Condens. Matter Mater. Phys.* **74**, 1–11 (2006).

50. Gupta, A., Hacquebard, L. & Childress, L. Efficient signal processing for time-resolved fluorescence detection of nitrogen-vacancy spins in diamond. *J. Opt. Soc. Am. B* **33**, B28 (2016).

51. Popa, I., Gaebel, T., Neumann, P., Jelezko, F. & Wrachtrup, J. Spin Polarization in Single Spin Experiments on Defects in Diamond. *Isr. J. Chem.* **46**, 393–398 (2006).

52. Giri, R., Dorigoni, C., Tambalo, S., Gorrini, F. & Bifone, A. Selective measurement of charge dynamics in an ensemble of nitrogen-vacancy centers in nanodiamond and bulk diamond. *Phys. Rev. B* **99**, 155426 (2019).

53. Manson, N. B. & Harrison, J. P. Photo-ionization of the nitrogen-vacancy center in diamond. *Diam. Relat. Mater.* **14**, 1705–1710 (2005).

54. Shinei, C. *et al.* Equilibrium charge state of NV centers in diamond. *Appl. Phys. Lett.* **119**, (2021).

Supplementary material

Optimization of rolling window

The rolling window for different window sizes was computed to assess the relative error (RE) of the average for each window and each concentration. For each point in figure S1 we calculated the RE for all measurements and took the average and calculated the standard deviation. Outliers were removed by IQR before computing the RE. This figure shows that there is a relation between the RE and the window size. It shows that the RE decreases with window size. Furthermore, the standard deviation of the RE also decreases with window size. What this implies is that for larger window sizes, the T1 over the full rolling window is more stable than for the smaller values. When comparing the different models presented in figure 5, it is clear that the bi exponential model has a few large outliers, as shown by the large standard deviations for smaller windows. However, after a window size of 4500 repetitions it behaves more like the other models. The single and stretched exponentials show less of these extreme outliers. These models still clearly show a decrease in relative error with larger windows. Furthermore, the figure shows that the single exponential model has the smallest RE while the bi-exponential has the highest RE.

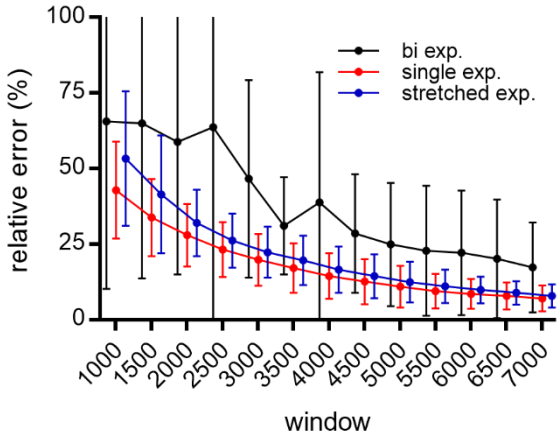

Figure S1: The relative error of the rolling window analysis of all measurements for different window sizes. Each point represents the mean of the relative error for the bi exponential model (black), single exponential (red) and the stretched exponential (blue). The error is computed as the standard deviation of the average of the relative error.

Chapter 3

Insight into a Fenton-Like Reaction Using Nanodiamond Based Relaxometry

Sandeep Kumar Padamati [†], **Thea Annie Vedelaar** [†], Felipe Perona Martínez, Anggrek Citra Nusantara and Romana Schirhagl *

* Correspondence: romana.schirhagl@gmail.com

† These authors contributed equally to this work

Abstract

Copper has several biological functions, but also some toxicity, as it can act as a catalyst for oxidative damage to tissues. This is especially relevant in the presence of H_2O_2, a by-product of oxygen metabolism. In this study, the reactions of copper with H_2O_2 have been investigated with spectroscopic techniques. These results were complemented by a new quantum sensing technique (relaxometry), which allows nanoscale magnetic resonance measurements at room temperature, and at nanomolar concentrations. For this purpose, we used fluorescent nanodiamonds (FNDs) containing ensembles of specific defects called nitrogen-vacancy (NV) centers. More specifically, we performed so-called T1 measurements. We use this method to provide real-time measurements of copper during a Fenton-like reaction. Unlike with other chemical fluorescent probes, we can determine both the increase and decrease in copper formed in real time.

Keywords: NV-centers; nanodiamonds; copper; Fenton-like reactions; diamonds

3.1 Introduction

Copper is one of the vital elements present in cells. It is especially important in enzymes, which catalyze a variety of biological processes including oxidation, photosynthesis or cell wall metabolism[1]. However, copper in its free hydrated form, i.e., Cu^{2+}, can be toxic to both plants and animals by altering membrane permeability and affecting chromatin structure, protein synthesis, and various enzyme activities[2]. In humans, several neurodegenerative diseases including Alzheimer's and Parkinson's disease are characterized by modified copper homeostasis[3]. Changes in copper metabolism in the brain either directly or indirectly increase oxidative stress, which is an important factor in neuronal toxicity. Copper-based materials are regarded as efficient catalysts in Fenton-like reactions at neutral pH and have thus been considered excellent candidates for developing new cancer treatments[4]. Notably, copper is used in chemodynamic therapy treatment for cancers by triggering ROS production. For this application, copper(I)-nanoparticles selectively kill tumor cells[5]. Another important process that involves copper in biology is the generation of hydroxyl radicals (HO●) and/or other reactive oxygen species (ROS). These are generated as a result of the reaction of copper with hydrogen peroxide (H_2O_2) in cells as a by-product of oxygen metabolism[6]. These reactions are studied by quantifying hydroxyl radicals using coumarin dyes[7] or other hydroxyl-specific dyes such as disodium terephthalic acid[8]. While these dyes have the advantage to be radical specific, they are limited by photo-bleaching and do not provide real-time measurements. Standard electron paramagnetic resonance (EPR) measurements can be used to detect copper(II). However, aqueous solutions are affected by the absorption of microwaves by water, which complicates measurements in biological samples[9]. In order to investigate Fenton-like reactions, in this case a reaction of copper with H_2O_2, we use T1-relaxometry in this article. This approach allows us to optically follow the reaction of copper with H_2O_2 at nanomolar concentrations in aqueous conditions, avoiding the effect of microwave absorption which is a bottleneck in conventional EPR.

So far, diamond magnetometry has been used for nanoscale magnetic resonance measurements and successfully applied to measure the magnetic field from nanoparticles[10], 2D materials, domain walls in magnetic structures[11], gadolinium ions in solution[12], spin-labeled molecules,

proteins with metallic parts[13] or even slices of cells[14]. Recently, the first measurements in living cells have been demonstrated[15–19]. Here, we use a specific form of diamond magnetometry called T1 or relaxometry measurements[20]. This technique is suitable to measure paramagnetic copper(II) as well as spin noise from free radicals[21]. Recently, we used T1 magnetometry to detect the radicals formed during a Fenton reaction. More specifically, we investigated the hydrolysis of H_2O_2 during UV-irradiation and during the reaction of iron (II)perchlorate with H_2O_2 [12]. However, since copper is often used in chemotherapeutic studies and is preferred there over iron, we investigated the effect of copper and its reaction with H_2O_2 in this article. The concentrations we used are comparable with concentrations which appear in cells[22]. This is the first use of relaxometry for the measurement of copper generated by a copper-H_2O_2 reaction. Furthermore, we also complement these measurements with standard spectroscopic tools.

3.2 Materials and Methods

3.2.1 Materials

FNDs were purchased from ADAMAS nano, (Raleigh, NC, USA) average size ~70 nm as stock solution of 1 mg/mL. Each of these particles contains an ensemble of several hundred NV centers. These particles are produced from HPHT synthesis followed by milling and irradiation by the manufacturer. In the last step of the particle synthesis the particles are treated with oxidizing acid and thus are oxygen terminated. They are used widely for other applications and have been characterized extensively[23–25]. $CuSO_4$ was purchased from the Alfa Aesar (Lancashire, United Kingdom). H_2O_2 (30 wt%), disodium terephthalate (Na_2TH) and hydroxy terephthalic acid (HTA) was purchased from Sigma-Aldrich (St. Louis, MO, United States) and used without further purification. Petri dishes with glass bottom were purchased from Ibidi. All experiments were conducted at around ~22 °C, atmospheric pressure in aqueous solutions. Caution! The drying or concentration of solutions that potentially contain H_2O_2 should be avoided. Prior to drying or concentrating, the presence of H_2O_2 should be tested for using peroxide test strips followed by neutralization on solid $NaHSO_3$ or another suitable reducing agent. When working with H_2O_2, suitable

protective safeguards should be in place at all times due to the risk of explosion.

3.2.2 Relaxometry

The nanodiamond stock solution was diluted to 10 µg/mL using ultrapure water. An amount of 20 µL of this solution was added to a Petri dish with a glass bottom, which was pre-treated with air plasma for 15 min. After adding the solution, the Petri dish was kept in a fume hood for 1 h to evaporate the solvent. Then, 100 µL of ultrapure water was added to the plate and the first set of T1 measurements was performed. Further, solutions of $CuSO_4$ were added until the respective concentrations (100 nM, 10 µM, 100 µM, 500 µM, 1 mM and 10 mM) were reached and T1 was measured. Another set of T1 relaxometry measurements was conducted with the same particle after adding H_2O_2 (30%) in the amount required to reach the specified concentration (10 nM, 100 nM, 1 mM, 10 mM).

The diamonds for T1 measurements were selected based on intensity counts (between 10^6 and 10^7 counts per second) recorded by a home-built magnetometer. After appropriate particles were identified, the T1 was measured. This was performed by repeating the pulsing sequence shown previously in our group[12]. Obvious aggregates were excluded. During analysis, particles with a T1 higher than 600 µs were excluded. These values were likely caused by dirt or an outlier in the nanodiamonds (extremely large or small particles or fitting errors). First, the NV-centers in the nanodiamond were polarized by the laser (532 nm, Ventum, laser quantum, Novanta Photonics (Wackersdorf, Germany)). To ensure proper polarization, the nanodiamonds were illuminated for 5 µs and the dark time between pulses varied between 0.2 µs and 10 ms. The pulsing was applied by sending the pulsing scheme with a pulseblaster (Pulseblaster ESR pro, SpinCore) to an acousto-optical modulator (AOM, Gooch & Housego, Gainesville, Florida, United States). While a single experiment lasts microseconds, each experiment is repeated 10,000 times to improve the signal-to-noise ratio. The resulting experimental time is approximately 10 min. The photoluminescent signal was detected with a sensitive avalanche photo diode (APD). A long-pass filter (550 nm) was placed before the APD to only allow the fluorescence from NV centers to pass through.

The fluorescence from the NV-centers was quantified in a detection window. This detection window was determined for each particle. The signal for each pulse was integrated over this window to obtain the T1 curve. This curve was fitted with a bi-exponential model (Equation (4)) as shown previously[12].

$$PL(\tau) = I_{inf} + C_a e^{-\tau/T_a} + C_b e^{-\tau/T_b} \quad 1)$$

Equation (1): Equation for obtaining T1.

This model approximates that an ensemble of NV centers consists of 2 groups: one with a shorter T1 and one with a longer one. The latter was found to be most concentration dependent in earlier experiments.

Instead of using the entire 10,000 data points to generate one T1 value, it is also possible to increase the time resolution by using a moving window method. To this end the 1st–2500th repetitions are combined in one data point, the points 100–2600 form the second point and so on. This equals to approximately 2.5 min of experimental time. We repeat the process until the last repetition of a window ends at the 10,000th repetition.

The T1 values obtained during this process are not independent, due to the overlap between the different windows. Outliers in the moving window results were determined using the interquartile range (IQR).

3.2.3 $CuSO_4$ Calibration Curve Using T1

A stock solution of $CuSO_4$ (1M) was prepared by dissolving $CuSO_4$ (2.49 g) in 10 mL of ultrapure water. For the calibration experiments, 100 µL of solvent (ultrapure water was taken in a petri dish with FNDs attached to it, and to this 1 M stock solution of $CuSO_4$ solution was added gradually in increments to obtain the desired concentrations (0.1 µM, 10 µM, 100 µM, 500 µM and 1 mM). T1 measurements were recorded at each concentration according to the procedure described in Section 2.1. pH values for the solutions are shown in Supplementary Figure S2.

3.2.4 UV–Vis Absorption Spectroscopy Measurements

UV/vis absorption spectra were recorded with a Specord600 spectrometer (AnalytikJena, Jena, Germany) in 10 mm path length quartz cuvettes. The spectroscopy was performed at room temperature from 180–1000 nm. UV–Vis absorption spectra were recorded at different time intervals The data analysis was performed by the Spekwin software (Spectragryph version 1.2.14. Author name Dr. Friedrich Manges, Germany).

3.2.5 Measuring the Concentration of Hydroxyl Radicals by HTA

Disodium terephthalate (Na_2TH) acts as chemical trap for hydroxyl radicals and is a standard hydroxyl dosimeter[8].

A calibration curve has been established with different concentrations of HTA against intensity using a fluorimeter (Edinburgh instruments (module sc-20), $\lambda_{Excition}$ = 330 nm and $\lambda_{Emission}$ = 420 nm). We performed a typical Fenton-like reaction using $CuSO_4$ (1 mM), H_2O_2 (10 mM) and Na_2TH (100 mM) in a quartz cuvette (10 mm pathlength). The solution (1.5 mL) contained $CuSO_4$ (1 mM) and Na_2TH (100 mM). Then, H_2O_2 (10 mM) was slowly added, and spectra were recorded at different time intervals. The fluorescence intensity was plotted for different concentrations of HTA to establish a calibration curve. From the calibration curve's slope, we determined the concentration of hydroxyl radicals formed during the reaction of $CuSO_4$ with H_2O_2.

3.2.6 Raman Spectroscopy

Raman spectra at 785 nm (300 mW at source, Cobolt Lasers, Hübner Photonics, Hannover, Germany) were acquired in a 180° backscattering arrangement. Raman scattering was collected by a 2.5 cm diameter plano-convex lens (f = 7.5 cm). The collimated Raman scattering passed through an appropriate long-pass edge filter (Semrock, Rochester, NU, USA) and was focused by a second 2.5 cm diameter plano-convex lens (f = 15 cm) into a Shamrock500i spectrograph (Andor Technology, Belfast, United Kingdom). We used a 2399 L/mm grating blazed at 300 nm and the data was collected with an iDus-420-BU2 charge-coupled device (CCD) camera (Andor Technology, Belfast, United Kingdom). The spectral slit

width was set to 12 µm. Data were recorded and processed using Solis (Andor Technology, Belfast, United Kingdom) software. Spectral calibration was performed using the Raman spectrum of acetonitrile/toluene 50:50 (*v*:*v*). Samples were held in quartz cuvettes with a 10 mm path length. Multi point baseline correction was performed for all spectra.

3.2.7 Oxygen Sensor Measurements

A typical measurement was performed by taking $CuSO_4$ (1 mM) 5 mL volume in a glass vial (15 mL). Then, H_2O_2 (10 mM) was slowly added. Oxygen sensor measurements were recorded using a WTW 2BA301 Oxi 3310. $CuSO_4$ (1 mM) and H_2O_2 (10 mM) solutions were used for these measurements. The temperature for the measurements was around ~22 °C.

3.3 Results and Discussion

We study the reaction of $CuSO_4$ at low concentrations (<1 mM) with H_2O_2 (<10 mM) at room temperature using fluorescent nanodiamonds (FNDs) that contain NV centers. These NV centers detect paramagnetic species within about 20 nm range[26]. Through this method we follow the real-time changes in copper(II) concentration. The reaction of the copper(II) leads to the formation of hydroxyl radicals, and hydroxide ions (Figure 1 and Equation (1)) and oxidized copper(III). The hydroxyl radicals have a chance to either react with another hydroxyl radical or they can react with hydrogen peroxide to form further hydroperoxide species. This in turn can lead to the formation of water and oxygen (see Equations (4) and (5) in figure 2). Another possible reaction path is the formation of a superoxide radical and copper(I). These superoxide radicals can react with excess copper in the solution to form Cu(I) liberating oxygen. As this reaction includes the formation of several radicals and copper oxidation states, it is a fast dynamic process. A technique that can provide a concentration of these species in real time at low concentrations is highly desirable.

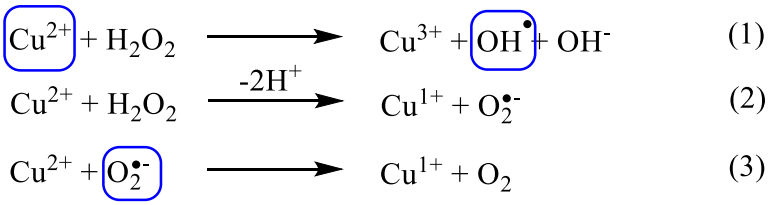

Figure 1. Reaction of copper(II) with H_2O_2 to form $OH^{\bullet}$ radicals and $O_2^{\bullet-}$ (species that are paramagnetic are marked in blue).

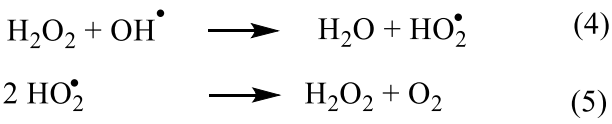

Figure 2. Radical formation from H_2O_2 and OH●.

3.3.1 T1-Relaxation Measurements

T1-relaxation measurements reveal the concentration of paramagnetic species present around the NV centers. In this paper, this is primarily copper(II). Superoxide radicals and OH● radicals which also occur in the reaction are present in relatively low concentrations and are short-lived and thus only detected in the higher concentrations. T1 measurements, which have been described before were performed as follows[12,27]. First, the laser brings the NV centers to the bright $m_s = 0$ state of the ground state. Then, we measure again after specific times (see the materials and methods sections for details) to see whether the NV centers are still in this state or not. Since the states differ in brightness (the $m_s = 0$ state is brighter) we can observe the process by recording the change in fluorescence. When there are flipping spins (in this case from copper or free radicals) in the surrounding, the NV centers will lose this state faster. Thus, the time that is required to lose the prepared state gives a quantitative measure for the concentration of these species.

From Figure 3a, we see that the T1 relaxation times are normalized for ultrapure water for different concentrations of copper. After the addition of copper(II), the T1 value is decreased by more than 50% w.r.t ultrapure water, and further addition of H_2O_2 resulted in an increase in the T1 value. This shows the conversion of copper(II) to copper(I) or copper(III) as shown in the scheme above, which has resulted in an increase in T1. The

data also supports the fact that copper(II) reacts with H_2O_2 to liberate OH● radicals (which were identified with other spectroscopic tools in the sections below) and the decrease in copper(II) concentrations over time.

When lower concentrations of copper(II) were used (10 µM), we observe a smaller decrease in T1 value (Figure 3a) compared to higher concentrations of copper(II) in agreement with the copper calibration shown Figure 4b. A calibration curve of T1 values measured for copper(II) solutions in Figure 4b shows that the detection limit of the copper(II) with FNDs can reach nanomolar concentrations, confirming that copper(II) still can be detected in the solution in the reaction time scale (which is 20 min).

The most plausible reasons for the smaller decrease in T1 at lower concentrations of copper(II) 10 µM compared to 1 mM are mainly (a) the reaction of copper(II) of H_2O_2 takes place at a slower speed (around 20 min) compared to higher concentration (>1 mM), which leads to slower decrease in T1; (b) the concentration of H_2O_2 is 100 µM which is 100 times less than H_2O_2 used from higher concentration (10 mM). Therefore, the copper(II) decay is slow, because of the lower availability of H_2O_2. In this case, less H_2O_2 is present in relation to the copper(II) decay by different amounts of H_2O_2 present in solution. A similar situation has been described by the Pham et al.[28] (c) In addition OH● radicals produced in the solution at higher concentrations of H_2O_2 might be quenched quickly by reducing excess H_2O_2. In this process, they form peroxide radicals and further dimerize to form H_2O_2 and O_2 as shown in Schemes 4 and 5. A similar observation has been described by Sapihu and co-workers, which is the most plausible steps in the OH● radicals decay process[29].

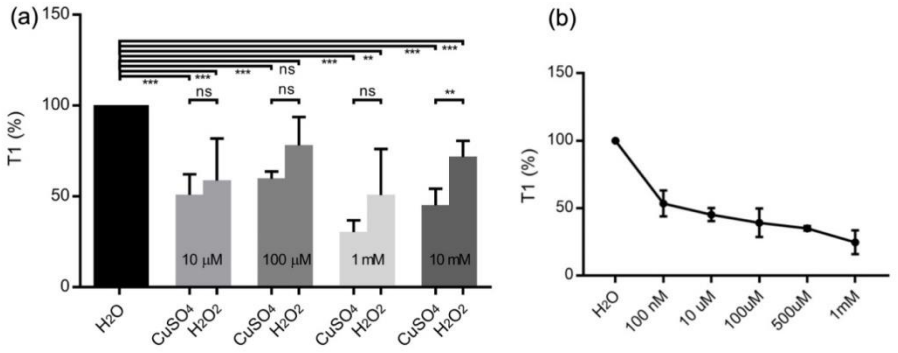

Figure 3. *(**a**) T1- relaxation measurements of water, $CuSO_4$ and after addition of H_2O_2 at different concentrations. Each bar represents an average of 4–5 independent measurements. (**b**) T1- relaxation measurements of CuSO4 at different concentrations (n = 4). The error bars represent standard deviations. (ns = non significant, * $p \leq 0.05$, ** $p \leq 0.01$, *** $p \leq 0.001$, **** $p \leq 0.0001$)*

Another important point to consider is the adsorption of copper ions on the diamond surface. Since FNDs are electronegative, they can potentially interact with copper ions. This process has been described before in detail for detonation nanodiamonds[30]. To test this hypothesis, we conducted T1 measurements of two concentrations and then reversed the order of measuring. Indeed, we observed that after measuring a large concentration, we were not able to detect the small concentration accurately (See Supplementary Figure S1). This is a common problem in analytical chemistry where it is common to measure small concentrations first or rinse thoroughly between measurements.

3.3.2 $CuSO_4$ Decay by UV–Vis Absorption Spectroscopy

UV–vis absorption spectra of $CuSO_4$ show a broad saturated band at 220 nm and a weak absorption at 800 nm, which is useful for monitoring the changes in the copper(II) concentration[31]. This band is caused by d-d band transitions, which indicate the concentration of copper(II)[32]. Figure 3 shows a clear decrease in absorption from copper(II) upon addition of H_2O_2. There is a change of 0.2 mM in concentration of copper over 20 min (based on the $\varepsilon = 12.6\ M^{-1}\ cm^{-1}$)[31]. This confirms that there is a reaction between copper(II) and H_2O_2. Pham et al. have shown that copper(II) reacts with H_2O_2 to form OH● radicals[28]. Thus, this is an example of a classical Fenton-like reaction. The studies here are consistent with the T1 relaxation

measurements from Figure 3b, where there is an increase in T1 due to the decrease in copper(II) concentration over the reaction time.

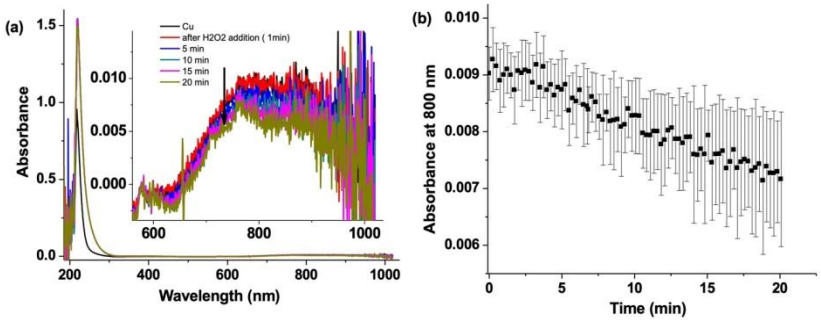

Figure 4. *(**a**) UV–Vis absorption spectra of CuSO4 (1 mM) (black) and after addition of H_2O_2 and (**b**) its kinetic trace plotted at 800 nm over 20 min.*

3.3. Hydroxyl Radical Detection by Emission Spectroscopy:

The fluorescent dye Na_2TH was used to detect OH● radicals produced by the reaction of copper(II) with H_2O_2 (Figure 1 and Equation (1)).

Na_2TH reacts specifically with hydroxyl radicals resulting in the formation of the fluorescent molecule hydroxyl tereprethalic acid (HTA). HTA is probed by excitation at 330 nm collecting the emission spectra at 420 nm (Figure 5a). In order to estimate the concentration of OH● radicals, a calibration curve of known concentrations of HTA was plotted. From this calibration, the concentration of OH● radicals produced in the reaction of CuSO4 with H_2O_2 was estimated to be 0.9 µM (Figure 5b).

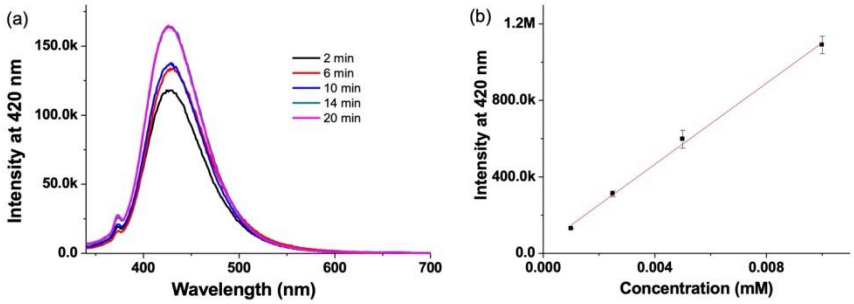

Figure 5. *(**a**) Fluorescence spectra of HTA obtained by the reaction of $CuSO_4$ (1 mM) and H_2O_2 (10 mM) with Na_2TH (100 mM), 2 min (black), 6 min (red), 10 min (blue), 14 min (green) and 20 min (pink)) and (**b**) calibration curve obtained by plotting the fluorescence intensity at 420 nm for different concentrations of HTA.*

3.3.4 H_2O_2 Decay by Raman Spectroscopy

To quantify the decrease in the H_2O_2 concentration over time, Raman spectroscopy was used (Figure 6a). The O-O symmetric stretch, which is the signature band of H_2O_2 at 876 cm^{-1} and its intensity were followed over time at 785 nm[33]. Since there is no resonance enhancement of this band at 785 nm, we have used higher concentrations of H_2O_2, i.e., 100 mM H_2O_2. The 876 cm-1 band decreases by 3% over time (Figure 6b), which shows that roughly 0.3 mM of H_2O_2 has been consumed over the reaction time (20 min). This indicates that H_2O_2 reacts with copper(II), and is consistent with UV–vis absorption, fluorescence, and T1 measurements described above.

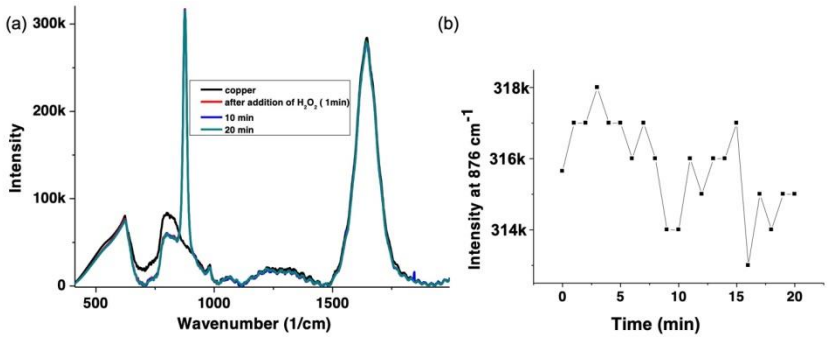

Figure 6. *(**a**) Raman spectra of $CuSO_4$ (1 mM) (black) and after addition of H_2O_2 (100 mM). Data points are shown at 1 min (red), 10 min (blue) and 20 min (green). (**b**) shows the intensity of the 876 cm^{-1} peak (H_2O_2 band (O-O band)) over 20 min detected by Raman spectroscopy with excitation at 785 nm. This indicates that the concentration of H_2O_2 is reduced during the reaction as outlined in Figure 1.*

3.3.5 Oxygen Sensor Measurements

Pham et al. proposed that oxygen is liberated from the reaction of copper(II) with H_2O_2[28]. To confirm this hypothesis, we performed oxygen sensor measurements before addition of H_2O_2 to copper(II) (5 mg/L). Over the reaction time, there is a steady increase in the concentration of dissolved oxygen which suggests a clear liberation of O_2 (14 mg/L) during the copper(II) reaction with H_2O_2 as shown in Figure 6.

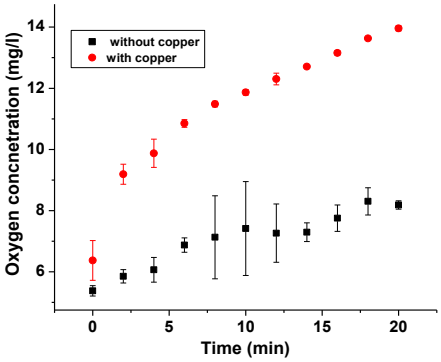

Figure 7. *Dissolved oxygen measurements during the reaction of $CuSO_4$ (1 mM) and H_2O_2 (10 mM) (red) and $H2O_2$ added to ultrapure water (black).*

3.3.6 Combined Measurements from Spectroscopic Techniques

Figure 7 shows the normalized concentration of copper(II), H_2O_2, OH● radicals and oxygen liberated during the reaction of $CuSO_4$ with H_2O_2 as well as our T1 measurements processed by the rolling window approach. We show the decrease in the concentration of copper(II) and H_2O_2, and an increase in hydroxide radicals and oxygen. These findings are very consistent with Figure 1. Hydroxyl radicals are produced in the solution and we observe a decrease in the copper(II) concentration which is consistent with the UV–vis absorption shown in Figure 4a. We also compare T1 obtained via the rolling window method with the conventional methods. We observed an initial decrease in water (100% in Figure 8) due to the presence of paramagnetic copper(II). As the reaction proceeds, the radicals are degraded and a decrease in copper(II) concentration occurs. T1 increases as a result. However, the T1 is not fully recovered to the level of the blank (only water), since there is a formation of hydroxyl radicals over time and not all copper(II) is consumed in the reaction.

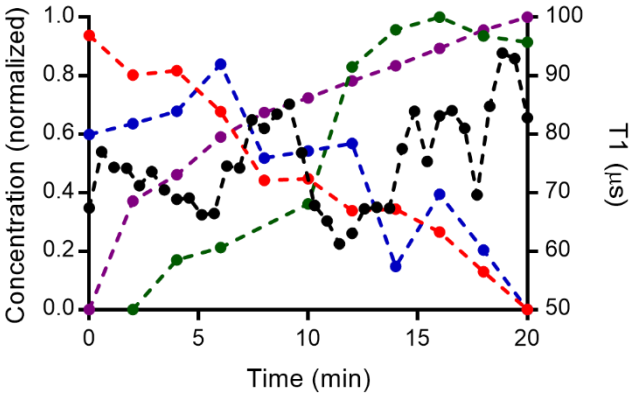

Figure 8. *Normalized concentration changes of the different species obtained in the reaction of $CuSO_4$ and H_2O_2. The changes T1 (black, averages from 9 particles are shown), the absorbance of copper (red), and H_2O_2 decay changes from Raman intensity (blue), fluorescence of the HTA for hydroxyl radicals (green) and the dissolved oxygen during the reaction (purple).*

3.3.7 Copper Detection by Existing Techniques

There are some other advanced spectroscopic techniques which are used to measure the copper concentrations as shown in the table below. However, new technologies are emerging to study copper in lower concentrations in real time as well. These techniques are atomic absorption[34,35], emission[36] or mass spectrometry[37]. These are particularly useful to detect elements with high sensitivity. However, the ionizing or flaming of the solutes is a drawback and the methods do not provide a real-time analysis. Some label-free sensors, for instance photoluminescent polymer nanodots (PPNDs), were recently reported to detect copper(II). Liu et al. described the usage of these PPNDs to detect copper(II) by using fluorescence quenching down to 1 nM[38]. Another photoluminescence method to detect copper is using ligation to the copper(II) center. The 3-hydroxy-5-nitrobenzaldehyde-4-hydroxybenzoylhydrazone (3-HNHBH) ligand was used by Abdulazeez et al. to ligate to copper(II). This ligand is highly selective towards copper(II) ions and the authors were able to detect copper with a detection limit of 0.34 $\mu g L^{-1}$ [39]. NV centers are infinitely stable and follow the paramagnetic species in real time at sub micromolar concentrations. We have shown copper(II) depletion in aqueous solutions using relaxometry. Additionally, magnetic resonance, in the long run, would allow us to differentiate between species using more complex pulsing schemes as the double electron resonance (DEER) can be used in near future[40].

Table 1. *Comparing sensing performance of different techniques.*

Technique	Concentration	Pros and Cons	Mechanism and Information Obtained	Reference
FAAS (flame atomic absorption spectrometry)	47–1888 nM	-destructive -spatial resolution +relatively simple	Atomic absorption on the sample is recorded. It is an invasive technique, but is highly sensitive to the element of choice.	[33]
ETAAS (Electrothermal atomic absorption spectrometry)	8 nM	-destructive -spatial resolution +high sensitivity		[34]
ICP OES (Inductively coupled plasma optical emission spectrometry)	19 nM	-destructive -destructive +relatively simple +high sensitivity	The mass spectra were recorded by emission spectroscopy. It is an invasive technique, and highly selective to copper.	[35]
ICP-MS (inductively coupled plasma mass spectrometry)	1 nM	-Expensive equipment -destructive +high sensitivity	The solution mass spectra were recorded, the method is highly specific to the particular element and highly sensitive to copper.	[36]
Cu(II)-DNAzyme	100 nM	+Non-destructive +spatial resolution	Cu(II) binds to DNA, which leads to the release of fluorophore (6-carboxyfluorescein). Hence a fluorescence signal from the fluorophore is detected.	[41]
FNDs (fluorescent nanodiamonds)	100 nM	-specialised equipment +Non-destructive +spatial resolution	Change in T1 time in presence of paramagnetic species. Copper(II) can be quantified down to nanomolar concentrations.	This work

3.4 Conclusions

In this work, we demonstrated the use of relaxometry measurements on a Fenton-like reaction (copper(II) and H_2O_2) and observed the decrease and increase in the concentration of paramagnetic species. We are able to measure nanomolar to micromolar concentrations of copper that are currently present, using low amounts of solution. Most

importantly we can measure sub nanomolar concentrations of copper that are usually hard to detect in aqueous environments with standard EPR or ultraviolet–visible (UV–vis) absorption, because of the limitations in their detection range. We worked at concentrations that can be present in biological environments, which in the future can be applied to study the Fenton reactions in biological environments. It has to be noted that in this specific case (next to copper) we are not able to detect the hydroxyl radicals themselves. The observation of copper(II) would help in other biological fields such as targeting cancer cells with copper nanoparticles. Relaxometry can be potentially applied to study the killing mechanism in tumor cells. The tools applied here would be a great asset in the future to study reactions in cells, which are catalyzed by copper systems such as copper nanoparticles. However, one has to be cautious if large concentrations are measured before small ones due to an adsorption of copper ions on the FND surface.

Author Contributions: S.K.P. and T.A.V. performed the experiments presented here with the help of A.C.N. and F.P.M. The draft of the paper was prepared by S.K.P. The project was conducted under the supervision of R.S. All authors have approved the final version of the article. All authors have read and agreed to the published version of the manuscript.

Funding: Romana Schirhagl acknowledges financial support from FOM via the projectruimte grant 15PR3229 and for an ERC starting grant 714289—Stress Imaging. Felipe Perona Martinez acknowledges support from the Chilean government via a CONICYT scholarship (grant number 72160222).

Data Availability Statement: All data in relation to this manuscript are available in the paper or on request from the authors.

Acknowledgments: We thank Wesley R. Browne from Stratingh Institute for Chemistry for kindly giving us access to a Fluorometer, and Raman spectrometer.

Conflicts of Interest: We have no conflicts of interest to report and there are no ethical concerns with this work that we are aware of.

References

1. Clavadetscher, J.; Hoffmann, S.; Lilienkampf, A.; Mackay, L.; Yusop, R.M.; Rider, S.A.; Mullins, J.J.; Bradley, M. Copper Catalysis in Living Systems and In Situ Drug Synthesis. *Angew. Chem. Int. Ed.* **2016**, *55*, 15662–15666. https://doi.org/10.1002/anie.201609837.

2. Yruela, I. Copper in plants: Acquisition, transport and interactions. *Funct. Plant Biol.* **2009**, *36*, 409–430.

3. Donnelly, P.S.; Xiao, Z.; Wedd, A.G. Copper and Alzheimer's disease. *Curr. Opin. Chem. Biol.* **2007**, *11*, 128–133.

4. Lee, H.; Lee, H.J.; Sedlak, D.L.; Lee, C. pH-Dependent reactivity of oxidants formed by iron and copper-catalyzed decomposition of hydrogen peroxide. *Chemosphere* **2013**, *92*, 652–658.

5. Ranji-Burachaloo, H.; Fu, Q.; Gurr, P.A.; Dunstan, D.E.; Qiao, G.G. Improved Fenton Therapy Using Cancer Cell Hydrogen Peroxide. *Aust. J. Chem.* **2018**, *71*, 826. https://doi.org/10.1071/ch18281.

6. Jomova, K.; Valko, M. Advances in metal-induced oxidative stress and human disease. *Toxicology* **2011** 2*83*, 65–87. https://doi.org/10.1016/j.tox.2011.03.001.

7. Chudal, L.; Pandey, N.K.; Phan, J.; Johnson, O.; Lin, L.; Yu, H.; Shu, Y.; Huang, Z.; Xing, M.; Liu, J.P.; et al. Copper-cysteamine nanoparticles as a heterogeneous Fenton-like catalyst for highly selective cancer treatment. *ACS Appl. Bio Mater.* **2020**, *3*, 1804–1814.

8. Freinbichler, W.; Colivicchi, M.A.; Fattori, M.; Ballini, C.; Tipton, K.F.; Linert, W.; Della Corte, L. Validation of a robust and sensitive method for detecting hydroxyl radical formation together with evoked neurotransmitter release in brain microdialysis. *J. Neurochem.* **2008**, *105*, 738–749. https://doi.org/10.1111/j.1471-4159.2007.05168.x.

9. Nesmelov, Y.E.; Gopinath, A.; Thomas, D.D. Aqueous sample in an EPR cavity: Sensitivity considerations. *J. Magn. Reson.* **2004**, *167*, 138–146.

10. Le Sage, D.; Arai, K.; Glenn, D.R.; DeVience, S.J.; Pham, L.M.; Rahn-Lee, L.; Lukin, M.D.; Yacoby, A.; Komeili, A.; Walsworth, R.L. Optical magnetic imaging of living cells. *Nature* **2013**, *496*, 486–489. https://doi.org/10.1038/nature12072.

11. Juraschek, D.M.; Meier, Q.N.; Trassin, M.; Trolier-McKinstry, S.E.; Degen, C.L.; Spaldin, N.A. Dynamical Magnetic Field Accompanying the Motion of Ferroelectric Domain Walls. *Phys. Rev. Lett.* **2019**, *123*, 127601. https://doi.org/10.1103/physrevlett.123.127601.

12. Martínez, F.P.; Nusantara, A.C.; Chipaux, M.; Padamati, S.K.; Schirhagl, R. Nanodiamond Relaxometry-Based Detection of Free-Radical Species When Produced in Chemical Reactions in Biologically Relevant Conditions. *ACS Sens.* **2020**, *5*, 3862–3869. https://doi.org/10.1021/acssensors.0c01037.

13. Ermakova, A.; Pramanik, G.; Cai, J.M.; Algara-Siller, G.; Kaiser, U.; Weil, T.; Tzeng, Y.K.; Chang, H.C.; Mcguinness, L.P.; Plenio, M.B.; et al. Detection of a Few Metallo-Protein Molecules Using Color Centers in Nanodiamonds. *Nano Lett.* **2013**, *13*, 3305–3309. https://doi.org/10.1021/nl4015233.

14. Davis, H.C.; Ramesh, P.; Bhatnagar, A.; Lee-Gosselin, A.; Barry, J.F.; Glenn, D.R.; Walsworth, R.L.; Shapiro, M.G. Mapping the microscale origins of magnetic resonance image contrast with subcellular diamond magnetometry. *Nat. Commun.* **2018**, *9*, 131.

15. Morita, A.; Nusantara, A.C.; Martinez, F.P.P.; Hamoh, T.; Damle, V.G.; van der Laan, K.J.; Sigaeva, A.; Vedelaar, T.; Chang, M.; Chipaux, M.; et al. Quantum monitoring the metabolism of individual yeast mutant strain cells when aged, stressed or treated with antioxidant. *arXiv* **2020**, arXiv:2007.16130.

16. Nie, L.; Nusantara, A.C.; Damle, V.G.; Sharmin, R.; Evans, E.P.P.; Hemelaar, S.R.; Van der Laan, K.J.; Li, R.; Perona Martinez, F.P.; Vedelaar, T.; et al. Quantum monitoring of cellular metabolic activities in single mitochondria. *Sci. Adv.* **2021**, *7*, eabf0573.

17. Nie, L.; Nusantara, A.C.; Damle, V.G.; Baranov, M.V.; Chipaux, M.; Reyes-San-Martin, C.; Hamoh, T.; Epperla, C.P.; Guricova, M.; Cigler, P.; et al. Quantum Sensing of Free Radicals in Primary Human Dendritic Cells. *Nano Lett.* **2021**, *22*, 1818–1825. https://doi.org/10.1021/acs.nanolett.1c03021.

18. Wu, K.; Vedelaar, T.A.; Damle, V.G.; Morita, A.; Mougnaud, J.; Martin, C.R.S.; Zhang, Y.; van der Pol, D.P.; Ende-Metselaar, H.; Rodenhuis-Zybert, I.; et al. Applying NV center-based quantum sensing to study intracellular free radical response upon viral infections. *Redox Biol.* **2022**, *52*, 102279. https://doi.org/10.1016/j.redox.2022.102279.

19. Sharmin, R.; Hamoh, T.; Sigaeva, A.; Mzyk, A.; Damle, V.G.; Morita, A.; Vedelaar, T.; Schirhagl, R. Fluorescent Nanodiamonds for Detecting Free-Radical Generation in Real Time during Shear Stress in Human Umbilical Vein Endothelial Cells. *ACS Sens.* **2021**, *6*, 4349–4359.

20. Tetienne, J.P.; Hingant, T.; Rondin, L.; Cavaillès, A.; Mayer, L.; Dantelle, G.; Gacoin, T.; Wrachtrup, J.; Roch, J.F.; Jacques, V. Spin relaxometry of single nitrogen-vacancy defects in diamond nanocrystals for magnetic noise sensing. *Phys. Rev. B* **2013**, *87*, 235436.

21. Schirhagl, R.; Chang, K.; Loretz, M.; Degen, C.L. Nitrogen-Vacancy Centers in Diamond: Nanoscale Sensors for Physics and Biology. *Annu. Rev. Phys. Chem.* **2014**, *65*, 83–105. https://doi.org/10.1146/annurev-physchem-040513-103659.

22. Korotkova, E.I.; Misini, B.; Dorozhko, E.V.; Bukkel, M.V.; Plotnikov, E.V.; and Linert, W. Study of OH radicals in human serum blood of healthy individuals and those with pathological schizophrenia. *Int. J. Mol. Sci.* **2011**, *12*, 401–409.

23. Morita, A.; Martinez, F.P.P.; Chipaux, M.; Jamot, N.; Hemelaar, S.R.; van der Laan, K.J.; Schirhagl, R. Cell Uptake of Lipid-Coated Diamond. *Part. Part. Syst. Charact.* **2019**, *36*, 1900116.

24. Shenderova, O.A.; Shames, A.I.; Nunn, N.A.; Torelli, M.D.; Vlasov, I.; Zaitsev, A. Review Article: Synthesis, properties, and applications of fluorescent diamond particles. *J. Vac. Sci. Technol. B Nanotechnol. Microelectron. Mater. Process. Meas. Phenom.* **2019**, *37*, 030802. https://doi.org/10.1116/1.5089898.

25. Hemelaar, S.R.; de Boer, P.; Chipaux, M.; Zuidema, W.; Hamoh, T.; Martinez, F.P.; Nagl, A.; Hoogenboom, J.P.; Giepmans, B.N.G.; Schirhagl, R. Nanodiamonds as multi-purpose labels for microscopy. *Sci. Rep.* **2017**, *7*, 720. https://doi.org/10.1038/s41598-017-00797-2.

26. Ofori-Okai, B.K.; Pezzagna, S.; Chang, K.; Loretz, M.; Schirhagl, R.; Tao, Y.; Moores, B.A.; Groot-Berning, K.; Meijer, J.; Degen, C.L. Spin properties of very shallow nitrogen vacancy defects in diamond. *Phys. Rev. B* **2012**, *86*, 081406. https://doi.org/10.1103/physrevb.86.081406.

27. Ong, S.Y.; Chipaux, M.; Nagl, A.; Schirhagl, R. Shape and crystallographic orientation of nanodiamonds for quantum sensing. *Phys. Chem. Chem. Phys.* **2017**, *19*, 10748–10752. https://doi.org/10.1039/c6cp07431f.

28. Pham, A.N.; Xing, G.; Miller, C.J.; Waite, T.D. Fenton-like copper redox chemistry revisited: Hydrogen peroxide ang superoxide mediation of copper-catalyzed oxidant production. J. Catal. 2013, 301, 54–64.

29. Bauhn, L.; Hansson, N.; Ekberg, C.; Fors, P.; Spahiu, K. The fate of hydroxyl radicals produced during H_2O_2 decomposition on a SIMFUEL surface in the presence of dissolved hydrogen. *J. Nucl. Mater.* **2018**, *507*, 38–43.

30. Shames, A.I.; Panich, A.M.; Osipov, V.Y.; Aleksenskiy, A.E.; Vul', A.Y.; Enoki, T.; Takai, K. Structure and magnetic properties of detonation

nanodiamond chemically modified by copper. *J. Appl. Phys.* **2010**, *107*, 014318.

31. Jancsó, G. Effect of D and 18O isotope substitution on the absorption spectra of aqueous copper sulfate solutions. *Radiat. Phys. Chem.* **2005**, *74*, 168–171.

32. Aravinda, C.L.; Mayanna, S.M.; Muralidharan, V.S. Electrochemical behaviour of alkaline copper complexes. *J. Chem. Sci.* **2000**, *112*, 543–550.

33. Padamati, S.K.; Draksharapu, A.; Unjaroen, D.; Browne, W.R. Conflicting role of water in the activation of H_2O_2 and the formation and reactivity of non-heme Fe^{III}–OOH and Fe^{III}–O–Fe^{III} complexes at room temperature. *Inorg. Chem.* **2016**, *55*, 4211–4222.

34. Bagherian, G.; Arab Chamjangali, M.; Shariati Evari, H.; Ashrafi, M. Determination of copper (II) by flame atomic absorption spectrometry after its perconcentration by a highly selective and environmentally friendly dispersive liquid–liquid microextraction technique. *J. Anal. Sci. Technol.* **2019**, *10*, 3.

35. Acar, O. Determination of cadmium, copper and lead in soils, sediments and sea water samples by ETAAS using a Sc+ Pd+ NH4NO3 chemical modifier. *Talanta* **2005**, *65*, 672–677.

36. Ferreira, S.L.; Bezerra, M.A.; Santos, A.S.; dos Santos, W.N.; Novaes, C.G.; de Oliveira, O.M.; Oliveira, M.L.; Garcia, R.L. Atomic absorption spectrometry–A multi element technique. *TrAC Trends Anal. Chem.* **2018**, *100*, 1–6. https://doi.org/10.1016/j.trac.2017.12.012.

37. De la Calle, I.; Perez-Rodriguez, P.; Soto-Gomez, D.; López-Periago, J.E. Detection and characterization of Cu-bearing particles in throughfall samples from vine leaves by DLS, AF4-MALLS (-ICP-MS) and SP-ICP-MS. *Microchem. J.* **2017**, *133*, 293–301.

38. Liu, S.; Tian, J.; Wang, L.; Zhang, Y.; Qin, X.; Luo, Y.; Asiri, A.M.; Al-Youbi, A.O.; Sun, X. Hydrothermal treatment of grass: A low-cost, green route to nitrogen-doped, carbon-rich, photoluminescent polymer nanodots as an effective fluorescent sensing platform for label-free detection of Cu (II) ions. *Adv. Mater.* **2012**, *24*, 2037–2041.

39. Abdulazeez, I.; Basheer, C.; Al-Saadi, A.A. A selective detection approach for copper (ii) ions using a hydra-zone-based colorimetric sensor: Spectroscopic and DFT study. *RSC Adv.* **2018**, *8*, 39983–39991.

40. Kim, M.; Mamin, H.J.; Sherwood, M.H.; Ohno, K.; Awschalom, D.D.; Rugar, D. Decoherence of near-surface nitrogen-vacancy centers due to electric field noise. *Phys. Rev. Lett.* **2015**, *115*, 087602.

41. He, E.; Cai, L.; Zheng, F.; Zhou, Q.; Guo, D.; Zhou, Y.; Zhang, X.; Li, Z. Rapid quantitative fluorescence detection of copper ions with disposable microcapsule arrays utilizing functional nucleic acid strategy. *Sci. Rep.* **2019**, *9*, 36.

Supplementary information

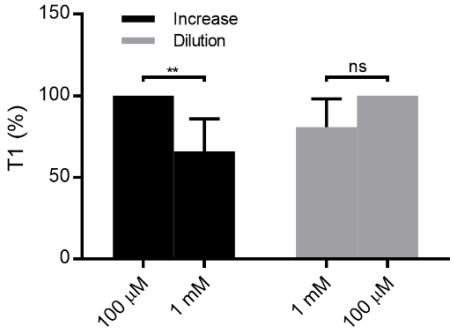

Scheme S1. Testing copper adsorbtion on FNDs. To test if copper adsorbs to the FNDs we reversed the order of experiments.

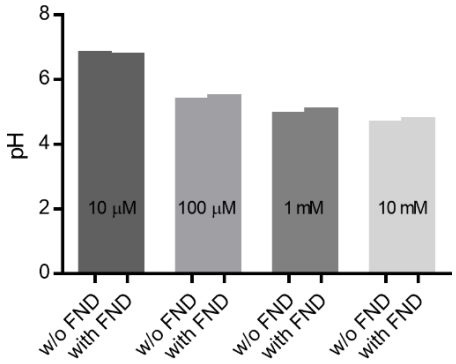

Scheme S2. pH values of the differently concentrated copper sulfate solutions with and without FNDs.

Chapter 4

Following polymer degradation with nanodiamond magnetometry

Runrun Li[1#], **Thea Vedelaar**[1#], Aldona Mzyk[1,2], Aryan Morita[1,3], Sandeep Kumar Padamati[1], Romana Schirhagl[*1]

Correspondence to: romana.schirhagl@gmail.com

# These two authors contributed equally

KEYWORDS: Polymer degradation, Nitrogen vacancy center, Magnetometry, Relaxometry, Nanodiamonds

ABSTRACT

Degradable polymers are widely used in the biomedical fields due to non-toxic, greatly biocompatible and biodegradability and it is crucial to understand how they degrade. These polymers are exposed to various biochemical media in medical practice. Hence, it is important to precisely follow the degradation of the polymer in real-time. In this study, we made use of diamond magnetometry for the first time to track polymer degradation with nanoscale precision. The method is based on a fluorescent defect in nanodiamonds, which changes its optical properties based on its magnetic surrounding. Since optical signals can be read out more sensitively than magnetic signals, this method allows unprecedented sensitivity. We used a specific mode of diamond magnetometry called relaxometry or T1 measurements. These are sensitive to magnetic noise and thus can detect paramagnetic species (gadolinium in this case). Nanodiamonds were incorporated into polylactic acid (PLA) films and PLA nanoparticles in order to follow polymer degradation. But in principle they can be incorporated into other polymers too. We found that T1 constants decreased gradually with the erosion of the film exposed to an alkaline condition. Besides, the mobility of nanodiamond increased, which allows to estimate polymer viscosity. The degradation rates obtained using this approach were in good agreement with data obtained by quartz crystal microbalance (QCM), fourier-transform infrared spectroscopy (FTIR), and atomic force microscopy (AFM).

4.1 Introduction

Understanding material degradation is an important area within material science.[1] Degradable polymeric materials, such as PLA, PCL, PGA or thermoplastics, hydrogels of natural and synthetic origin are increasingly popular for biomedical applications.[2,3] They are easy to process and functionalize, have tunable mechanical properties, often low toxicity, and controlled degradation times. Their applications include treatment of cancer,[4] the development of vaccines,[5] the manufacture of nanoparticles with increased plasma half-life,[5,6,7] scaffolds for cell culture and tissue regeneration or drug delivery.[8]

Here, we investigate the degradation of polylactic acid as a model system. This polymer is widely used for instance in tissue engineering,[9] drug delivery,[10] or wound management.[11]

There are several methods which can be used for studying material degradation. Imaging methods as atomic force microscopy (AFM), scanning force microscopy reveal changes in the surface morphology,[12] while spectroscopic tools as infrared spectroscopy (IR), X-Ray Photoelectron Spectroscopy (XPS)[13] or Raman spectroscopy reveal changes in chemical composition.[14] However, none of them allow straightforward and time efficient tracking of polymer degradation time in real-time with high precision. Our aim here is to evaluate the usefulness of diamond magnetometry for this purpose.

Diamond magnetometry is a new technique which allows nanoscale magnetic resonance measurements.[15] It is based on defects in diamond, which change their optical properties based on their magnetic surrounding. Since the optical signals are easier to read out and this method offers unprecedented sensitivity down to the single spin level.[16] This technique has already been successfully applied to measuring magnetic structures,[17,18] spin labels,[19] ions in solution,[20] iron containing proteins,[21] or free radicals.[22] Recently, temperature,[23,24] orientation,[25] or even metabolic activity[26,27] have been detected with this technique within living cells. Polymers including diamonds have been used for several applications[28] including generating sensitivity for changes in pH,[29] protecting diamond sensing particles from attracting a protein corona,[30] drug delivery[31] or for preventing aggregation.[32] Yet, diamond magnetometry has not been used before for

sensing polymer properties themselves, which is shown here. In this study, a home-made magnetometry setup was used to investigate degradation of an exemplary polymer (PLA) at different pH conditions via measuring relaxation time and track the displacement of diamond. The derived degradation was compared to the data obtained using conventional techniques, namely: AFM, FTIR, and QCM. The PLA has degraded much quicker around pH=13 than at neutral pH. This degradation led to a sharp decrease in the relaxation of nitrogen-vacancy (NV) center spins. A schematic representation of the experiments is shown in Figure 1.

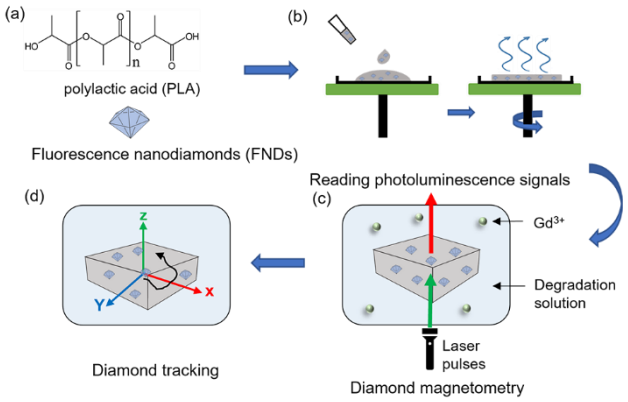

Figure 1. *Overview of PLA film preparation and degradation experiment. (a) The compounds of the polymer film: Poly (L-lactic acid) (PLA) and fluorescent nanodiamonds (FND). (b)FND sensors are embedded in the polymer by simple mixing and spin-coating is used to produce a thin film. (c) The PLA film containing nanodiamond sensors is immersed in degradation medium which contains* Gd^{3+}*. When the film is degraded* Gd^{3+} *(green dots) can come closer to the nanodiamonds and thus leads to an increase in spin noise which can be detected by a home-made magnetometry setup. (d) Particle tracking is used to evaluate polymer degradation in real-time.*

4.2 Experimental Section

4.2.1 Materials.

PLA was purchased from Sigma-Aldrich. Its molecular weight and M_w/M_n are about 260,000 and 1.5, respectively. Its viscosity is about 2.0 dL/g, 0.1% (w/v) in chloroform (25 °C). Sodium hydroxide pellets, chloroform and gadolinium chloride were purchased from Sigma-Aldrich. Fluorescent nanodiamonds (FNDs) with a hydrodynamic mean diameter around 70 nm were purchased from Adamas Nanotechnologies. These

particles are produced by high pressure high temperature (HPHT) synthesis followed by size separation and irradiation (3MeV electrons at a fluence of $5*10^{19}$ e/cm^2).[33] As a result of the irradiation, nanodiamonds contain 300 nitrogen-vacancy centers per diamond on average. Thus, every measurement is essentially an average of 300 individual sensors within one particle and reproducibility is greatly enhanced over single defect sensing. These particles are widely used and have been extensively characterized before.[34,35] Au-coated quartz crystals (QSX301, 4.95 MHz, available from Biolin Scientific, Sweden) were used for Quartz crystal microbalance measurements with dissipation monitoring.

4.2.2 AFM observation of morphology.

The morphology and roughness of the films are altered during exposure to different media, and thus are helpful when characterizing degradation behavior.[36] AFM is an excellent tool for exploring surface morphology and monitoring roughness. Here, we used AFM to observe morphology and roughness of PLA films with or without degradation. To prepare the samples, 50 µL of PLA solution in chloroform (5 mg/mL) was dropped on the silicon wafer (N-type, contains no dopant, diam.× thickness 3 in.× 0.5 mm, Sigma-Aldrich). The polymer films were prepared by spin-coating with 30 rpm, 5 min. The thin films were treated with solution of pH 7 (PBS), pH10 (NaOH) and pH 13 (NaOH) for different times (0, 30, 60, 120, 300 min). Degradation was performed at the room temperature. To remove salt residues from the surface of PLA films, the films were rinsed twice with Milli-Q water and dried with nitrogen before scanning. AFM (Nanoscope IV Dimension tm 3100, USA) experiments were performed using contact mode in the air with a V-shaped silicon cantilever (force constant 0.35 N/m, tip curvature radius <10.0 nm, and a cone angle of 20°) equipped with a dimension hybrid XYZ SPM scanner head (Veeco, New York, USA). The scanned surface area for each image was 5×5 µm, and at least three replicates were tested. The roughness parameters Ra (arithmetic mean roughness) and Rq (root mean square (RMS) roughness) were obtained.

4.2.3 QCM detection of degradation.

Quartz crystal microbalance with dissipation monitoring (QCM-D), is an extension of QCM, the parameter D is the dissipation factor, which provides real-time information on the softness of the adsorbed layer on the

sensor surface. QCM-D is a sensitive technique to monitor properties of polymer films in real-time. This method can detect changes of mass, thickness, and viscoelasticity of films on the surface of quartz oscillators. Hence, many researchers have used this tool to observe the degradation of polymer films.[12,37] A Q-Sense E4 module (Q-sense, Gothenburg, Sweden) containing four sensors, to run four samples in parallel, was used. Sensors and flow cells were cleaned before each experiment as follows: sensors were immersed in a mixture of 3:1:1 of Milli-Q water, ammonia (25%), and hydrogen peroxide (30%) at 75 ℃ for 5 min. Then, the sensors were rinsed with Milli-Q water, dried with nitrogen, and treated with UV/ozone for 10 min. The flow cells were cleaned with 2 wt% of sodium dodecyl sulfate and Milli-Q water for 10 min, respectively. Afterward, the PLA pellets were dissolved in chloroform to a concentration of 5mg/mL. Then, Au-coated sensors were attached to the holder of the spin-coating device and 50 µL of PLA solution was pipetted onto the quartz plate. The holder was spun slowly at 30 rpm for 5min to ensure that the film was dried completely. The whole process was carried out under a fume hood. Before the QCM-D measurement, a stable baseline was established by Milli-Q water for several minutes until the frequency was constant. Then sensors coated with PLA films were exposed to solutions at pH 7(0.01M PBS), pH10 and pH 13(NaOH solution) to accelerate degradation. Changes in resonance frequency (ΔF) and dissipation (ΔD) were recorded within 360 min (25 ℃, 50 µL/min) from 3 sensors simultaneously. The linear Sauerbrey relation (equation (1)) was used to convert Δf to adsorbed or desorbed matter.[38]

$$\Delta m = -(C/n)\,\Delta F \qquad (1)$$

Where Δm means change in mass, C is a mass constant, 17.7 ng/ cm^2/Hz for a 4.95 MHz crystal, related to the properties of quartz and n is the overtone number (n=3, 5,7, 9 etc). The film thickness (δ) was calculated by using the density of PLA (ρ = 1210 kg/m^3) and equation (2).

$$\delta = \Delta m/\rho \qquad (2)$$

4.2.4 Fourier-transform infrared spectroscopy (FTIR) characterization.

Functional groups of polymers can be identified by FTIR. The films were prepared by spin-coating. The difference is that the Teflon Petri dish was used as a substrate, and then films were detached from the dish after

complete drying. The degradation time points of FTIR were set to 0, 30, 60, 120, 300 min. The infrared spectra of initial and degraded films were collected by a Cary 600 series FTIR Spectrometer (Agilent Technologies, Santa Clara, CA, USA) within 400-4000 cm^{-1} wavelengths. The total number of scans was set to 32 for a single spectrum with a spectral resolution of 4 cm^{-1}. The transmission (T) scan type was used when infrared spectroscopy was performed. The absorbance (A) was calculated using the following logarithmic function (equation (3)) between transmission and absorbance:

$$A = \log_{10} (1/T) \quad (3)$$

The degradation of the PLA film was assessed by calculating an absorbance ratio (equation (4)) as follows:

$$\text{Absorbance ratio} = A\ \text{peak}(x)/A_{ref}\ \text{peak}(1455cm^{-1}) \quad (4)$$

The X stands for different peaks related to the PLA degradation process and 1455cm^{-1} band (methyl absorption peak) can be represented by the simple equation.

$$Apeak = AC\text{-}BC \quad (5)$$

where BC is the height of baseline, AC depicted the absolute intensity of the functional group band related to the reference group.

4.2.5 T1 measurements.

Here, we used a specific type of diamond magnetometry measurements called T1 or relaxometry measurements. 1 mg/mL FNDs stock solution was mixed into 5 mg/mL of PLA in chloroform solution to produce a 0.1% weight ratio of FNDs. 50 ul of the mixture were dropped onto the 35 mm plastic Petri dishes. The polymer films with FNDs were prepared by spin-coating with 30 rpm for 5 min until the solution was completely evaporated. Experiments were carried out by adding degradation solution of pH 7, 10 or 13 with 10nM Gadolinium chloride. The experiments were conducted on a home-made magnetometry similar to instruments used in the field and described earlier.[39] For light collection we used a 100x magnification oil objective (Olympus, UPLSAPO 100XO).To perform a T1 measurement, specific defects called nitrogen vacancy centers in nanodiamonds are excited with a green laser. As a result, they are pumped in the brighter m_s=0 state of the ground state. Over time, the NV^-

centers relax back to the less bright thermal equilibrium. This can be detected optically by measuring brightness after a varying dark time. The relaxation process occurs faster in presence of spin noise (in this case from gadolinium ions). We implemented the ability to pulse the laser with an acousto-optical modulator (Gooch & Housego, model 3350-199) to conduct the pulsing sequence that is shown in Figure 2. More specifically, a train of 5 µs green laser pulses (532 nm) with dark times between 200 ns to 10 ms was used to excite the NV centers. For detection we used a 550 nm long-pass filter to eliminate unaltered laser light and an avalanche photodiode (APD) (Excelitas, SPCM-AQRH). We repeated the pulse sequence 10000 times for each T1 measurement to reduce noise. While a single measurement only lasts a few hundred microseconds, the entire sequence including repetitions lasts around 16 minutes. The optically detected T1 signals obtained in the measurement are equivalent to T1 signals in conventional magnetic resonance imaging (MRI) but for nanoscale voxels. The data were analysed by using a two-exponential model.[22] In short, this model assumes that an ensemble of NV centers can be approximated as a part with short T1 and a part with long T1. The model reveals 2-time constants for these two sub-ensembles. We used the longer time constant since it has proven to be more sensitive to changes in the environment. A calibration which links T1 with a gadolinium concentration can be found in.[22]

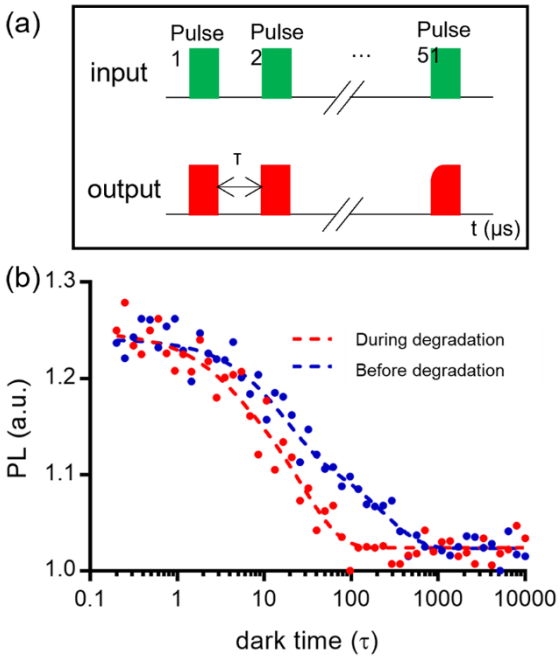

Figure 2. *T1 relaxation measurements: (a) Pulsing sequence for a T1 measurement. The green pulse indicates that the laser is turned on. During the pulse the NV- centers are initialized into the bright ms = 0 state of their ground state. Between laser pulses the NV- centers are allowed to relax during a variable dark time τ. During this time NV- centers return to the darker equilibrium between ms = 0 and ms = ±1. The read out is shown in red and has a different shape depending on the distribution of the ms states. In presence of spin noise (from Gd in this case) the decay in photoluminescence (PL) shown in (b) occurs faster. (b) shows an example of a T1 curve before and after degradation of the PLA film. In the blue decay curve the diamond is further away from* Gd^{3+} *before the degradation of PLA then in the red curve after degradation.*

4.2.6 Nanodiamond tracking.

After identifying a particle via its fluorescence, the tracking algorithm was started. The algorithm consists of scanning the known area in a set window (10x10 µm) with a set number of pixels (50x50). This gives us an image of the FND. The intensity is projected on the x axis and a gaussian is fitted through this intensity profile. Based on the gaussian, the voxel with the highest intensity in x is determined. The same is done in the y direction. This gives a new location for the particle in x and y. Afterwards the point at the maximum is scanned in the z-direction. The point with the highest intensity is taken as the corrected z. This process is repeated for a set

number of repetitions to fit the time window. During degradation, the particle is increasingly mobile which can be seen by an increase in movement. This is measured by calculating the diffusion coefficient (D, μm/s) for the complete track. The diffusion coefficient is calculated as explained in [40]. The diffusion coefficient depends on the mean square displacement, velocity of the particle and the α coefficient. The exact relation depends on the type of motion the particle undergoes at the time. The type of motion is determined by fitting the mean square displacement with the different types of motion and selecting the type of motion with the best fit.

4.2.7 Incorporation of FNDs into polymer nanoparticles.

PLA nanoparticles loaded FNDs were prepared using the solvent emulsion evaporation method. PLA was dissolved in chloroform to a concentration of 10 mg/mL. Then 70 nm FNDs (2%, w(FNDs)/w(PLA)) were mixed with chloroform containing PLA. PVA (1%, w/v) was dissolved in Milli-Q water under 90 degree, which is used as the dispersant to stabilize emulsion and form nanoparticles. The organic phase and aqueous phase were mixed, and then tip-sonication for 3 minutes over an ice bath. Then the emulsion was magnetically stirred overnight at room temperature while the chloroform was evaporated. Subsequently, nanoparticles were collected and washed three time with Milli-Q water via centrifugation at 10000 rpm for 15 minutes and removing the supernatant. Nanoparticles were re-suspended in water and stored at 4˚C until usage.

4.2.8 Statistics.

All data were presented as mean ± standard deviation. Statistical significance was determined with Graphpad Prism 8.0.1 by a one-way ANOVA or ordinary two-way ANOVA, followed by Tukey's multiple comparison test. $P < 0.05$ is considered statistically significant (*$P < 0.05$, **$P < 0.01$, ***$P < 0.001$, and ****$P < 0.001$). The AFM images processing and the roughness evaluation of films were performed with Nanoscope analysis version 1.80. Origin pro 9.0 software (Origin Lab Corporation, Northampton, MA, USA) was used to plot FTIR graphs and measured peak height.

4.3 Results and discussion

4.3.1 PLA film surface morphology and roughness.

AFM can characterize the sample surface, allowing the measurement of parameters such as roughness and uniformity of the sample surface. It has become an important tool for the characterization of polymer degradation.[41,42] The PLA film surface and roughness during degradation was observed by AFM. Figure 3 shows 3D images as well as height profiles of PLA samples after 0, 30, 60, 120, 360 min incubation at pH 13. We can see a dramatic change in surface morphology from AFM images and corresponding Ra (arithmetic mean roughness) and Rq (root mean square (RMS) roughness) results over increasing incubation times. The roughness Ra and Rq of the film, shown in Figure 4, before degradation was 2.7±0.37 nm and 3.3±0.43 nm respectively, while Ra and Rq increased significantly to 7.3±1.0 nm and 12.2±1.17 nm after 30 min of degradation. 60 min after degradation Ra and Rq were 11.5±3.10 nm and 16.7±3.65 nm. This shows that the degradation of pH 13 increases surface roughness within 60 minutes. After 120 min or 240 min degradation, the film is completely degraded. For pH 7 and pH 10, film morphology images and roughness value after degradation were similar to the untreated surface (see supplementary information Figure S1 (A)and (C)). Statistically, roughness Ra and Rq value have no significant difference each other (to see Figure S1(B) and (D)), which indicated that the film barely degraded in neutral and weakly alkaline environment. The degradation times determined from these experiments were used during the remained of the manuscript.

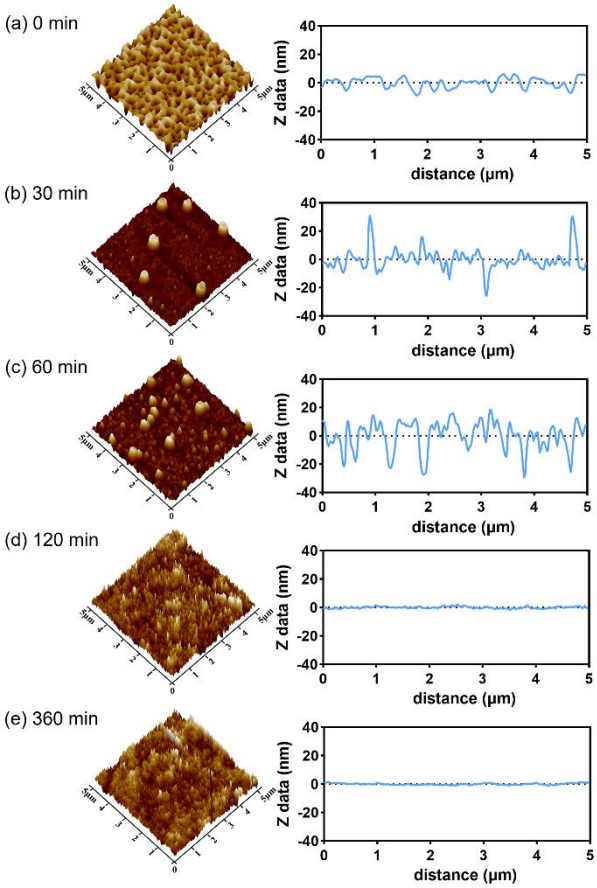

Figure 3. *Contact mode AFM images of PLA film surfaces (the left column) and profilograms along a line across the surface (the right column). (a) shows the PLA film before degradation at pH 13, (b) after 30 min, (c) 60 min, (d) 120 min and (e) 360 min of degradation, respectively.*

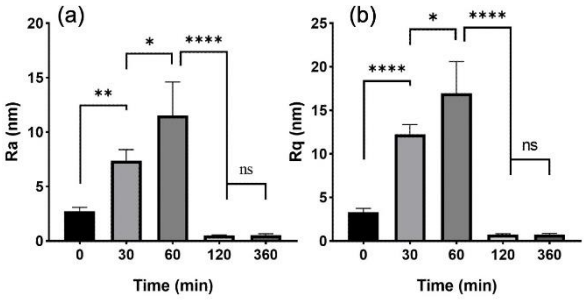

Figure 4. *Corresponding surface roughness parameters, arithmetic mean roughness Ra values (a) and RMS roughness Rq (b) were calculated from the AFM images before and after incubation in degradation medium at pH 13 for different times.*

4.3.2. QCM-D analysis of PLA thin film degradation.

The progress of degradation was further confirmed by QCM as shown in Figure 5. The raw data for ΔF and ΔD are shown in Figure S2. Figure S3 shows the conversion of these data into mass changes. The mass was further converted into a film thickness considering PLA's density using equation (2). Similarly to the AFM experiments, the PLA films were treated with solutions at different pH for 360 minutes, and the real-time changes of resonance frequency (ΔF) and dissipation (ΔD) were monitored at different overtones (3, 5, 7, 9, 11). The ΔF 3 data was used to analyze film mass and thickness, because in the 3rd overtone of the quartz crystal can be performed the best energy trapping.[43] No significant changes occurred when the initial Milli-Q water was replaced with PBS at pH 7. Throughout the experiment, the mass and thickness remained constant which proved that the film was not softened and did not degradation in pH 7. When Milli-Q water in the QCM cell was replaced with pH 13 solution, the film thickness first increased slightly, which was probably due to swelling. Afterwards, a rapid decrease of thickness was observed until the curve levelled off for incubation longer than 120 minutes. At the same time, the dissipation first increased and then decreased, indicating that the film softened first and was totally degraded during the degradation. At pH 10 the decrease in frequency was less pronounced indicating a slow degradation. Hence, the variation of surface morphology and roughness of the film observed by AFM was consistent with the thickness and mass changes of QCM.

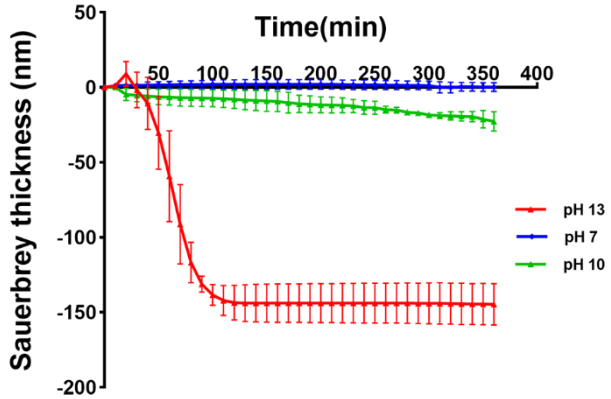

Figure 5. *The thickness versus time plot at pH 7, pH 10 and pH 13 solutions at 25℃. The thickness was obtained using the Sauerbrey equation (2). Corresponding ΔF and ΔD and Δm data are shown in Figure S2 and Figure S3 in the Supplementary Information.*

4.3.3 FTIR spectrum characterization.

To determine the chemical composition of the films incubated in degradation solution over time, we compared spectra (0 min) of non-degraded and degraded films at different times. The results are shown in supporting Figure S4. We found that spectra of non-degraded films show the expected absorbance bands. During the course of degradation, the spectra remained similar. All of them have the following typical absorption bonds: C-H stretching (asymmetric and symmetric band) at 2998 and 2944 cm^{-1}, C=O carbonyl stretching at 1750 cm^{-1}, CH_3 stretching at 1454 cm^{-1}, C-H deformation vibration at 1382 and 1362 cm^{-1}, and -CH-O- and -O-C=O stretching of C-O bands at 1185 and 1090 cm^{-1}.[44,45] According to Araque et al, the carbon of the ester groups in PLA chains is attacked by the hydroxyl ions in the basic condition,[46] and then the ester linkage will finally produce carboxylic and hydroxyl end-group, the schematic diagram is shown in Figure 6. This way the alkaline conditions can accelerate the degradation rate by rendering the PLA film more hydrophilic. Therefore, the C=O peak in 1750 cm^{-1}, C-O peaks at 1185 and 1090 cm^{-1} were related to film degradation. The intensity of peak ratio was evaluated to follow the degradation of polymer. Methyl at 1454 cm^{-1} was used as the internal reference peak of PLA. Figure 7 shows the changes of peak ratios for these three peaks. We found that all ratio intensities (1750 cm^{-1}, 1185 cm^{-1}, 1090 cm^{-1}) suffered a significant decrease only when exposed to the pH 13

solution, and the degradation tendency decreased rapidly from 0 to 120 minutes, and then remained stable. This agrees with AFM and QCM results where we found similar degradation times.

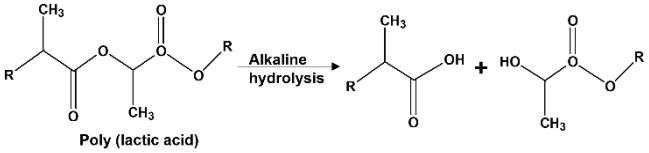

Figure 6. *The scheme for alkaline hydrolysis of PLA, the ester linkage on PLA backbone chains is cleaved into carboxylic and hydroxyl ended chains.*

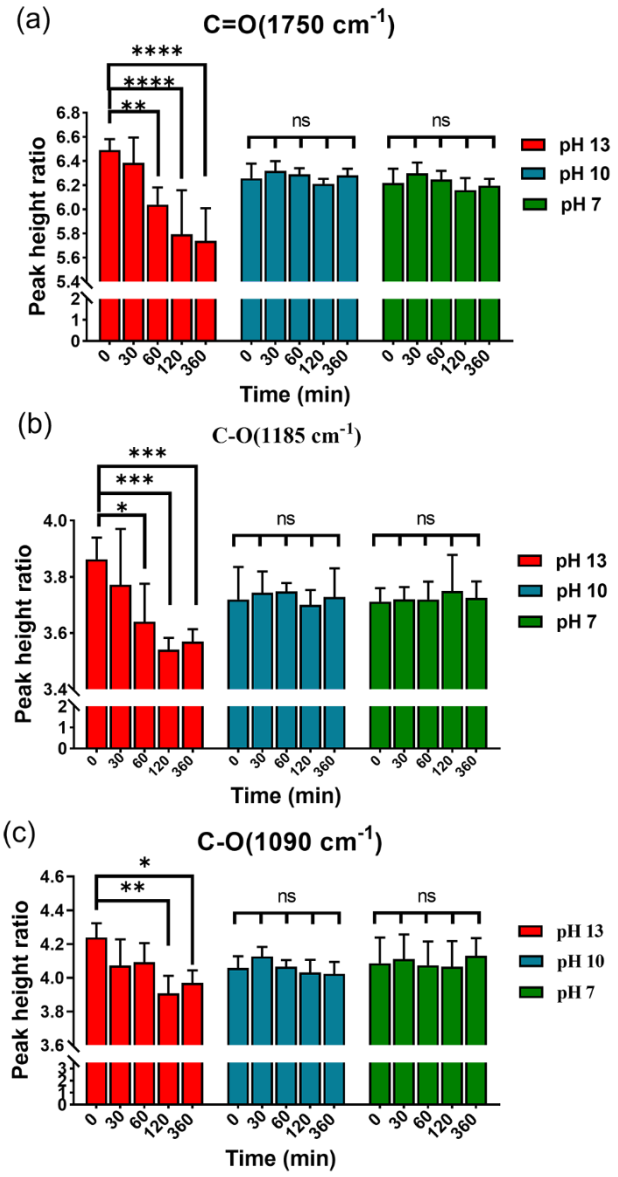

Figure 7. *Absorbance height ratio of different characteristic bands related to degradation determined by FTIR.*

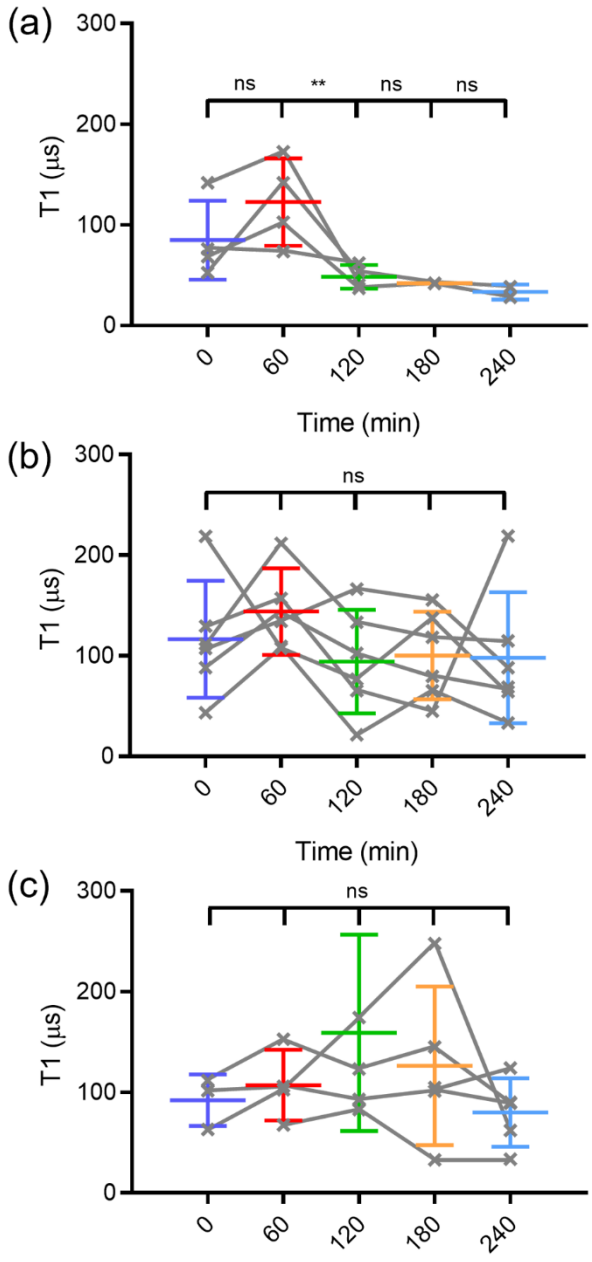

Figure 8. *T1 results for degradation of the PLA films at pH 13 (a), pH 10 (b), and pH 7 (c). Grey lines indicate individual particle results while the colored bars show averages. The error bars represent standard deviations.*

4.3.4 T1 relaxation measurements.

To assess PLA degradation using T1 measurements, 0.1wt% FNDs were mixed into the polymer prior to film formation. This small concentration of FNDs was sufficient to obtain clear readout. A confocal picture of FNDs inside of the PLA film, confirming homogeneous distribution of particles, is shown in supplementary figure S5. To determine whether 0.1wt% of 70 nm FNDs will affect the degradation of a PLA film, we followed the degradation of a PLA film with FNDs and PLA film without FNDs in pH13 solution for 360 minutes by QCM (shown in Figure S6). We observed that the resonance frequency (ΔF) behaved almost the same in both polymers with no significant

difference between the two curves. Then we measured the T1 of several FNDs twice every hour. We degraded the polymer by adding 20uL of a degradation solution at pH 7, 10 or 13 with 10nM Gadolinium chloride. The gadolinium ions (Gd^{3+}) acts as a spin noise source, therefore reducing the T1 when in the vicinity of the FND. The polymer itself forms a barrier between the FND and Gd^{3+}. Due to the subsequent degradation of the polymer, Gd^{3+} can approach the FND. Figure 8 shows the T1 value at different time points of the polymer degradation over the course of 4 hours. Figure 8 (a) shows that the T1 clearly decreased over time in the solution with pH=13 but becomes more stable near the end. The increase of T1 in 60 minutes may be due to swelling of the film after adding the solution, which reduces the signal which FNDs feel from Gd^{3+}. We did the same experiment with pH 10 and pH 7 solution, as shown in Figure 8 (b) and (c). The graphs do not show a trend and there is no significant change visible at pH 10 and pH 7. This indicates that the polymer film was difficult to degrade rapidly under both conditions. These results are in a good agreement with the standard methods in terms of degradation timings. However, the results obtained here are in real time (unlike results from AFM) and local at the nanoscale (unlike QCM). It has to be noted that at this point there is quite some variability in T1 values. The uncertainty from variation between nanodiamonds and their location in the film. The variation between nanodiamonds is something that is known within the community and actively researched. Potential approaches to reduce the variability include size separation to improve size uniformity, altering the surface chemistry to be more uniform as well as optimizing the fabrication

process itself. There are for instance ways to produce more uniformly shaped nanodiamonds or control the environment of the NV centers.[47] But such particles are not available yet. There are a few things that we already do. We use relatively large particles containing ensembles. This greatly reduces variability. Additionally, we select particles with similar counts. This way we ensure that we pick particles of a similar size. The other source of variability (which is greater than the previous one) is the location in the film. At this point the only way to achieve this was choosing particles at a similar height, but this approach is of course limited by the confocal resolution.

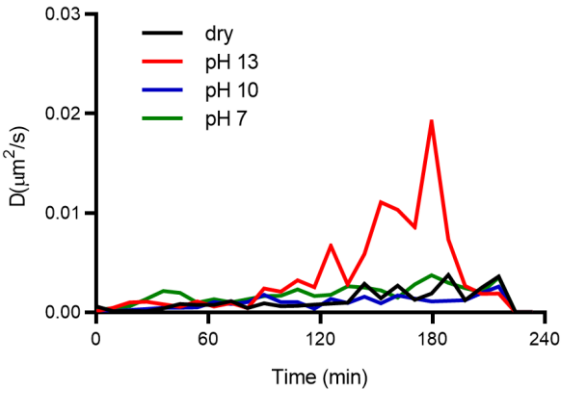

Figure 9. *The diffusion coefficient of FNDs in the polymer films under different degradation conditions. The 4 different conditions are shown in different colors: dry in black, pH 13 in red, pH 10 in blue and pH 7 in green. For each condition, 5 different particles were tracked continuously over 220 minutes.*

4.3.5 Nanodiamond tracking.

We also followed polymer degradation by assessing the mobility of the nanodiamond during degradation. To track the particle, we first identified a FND in the film. Ideally, this FND was not too large (around 1 to 5 million counts/seconds), but the particle was easy to identify compared to the background. After identification, the algorithm to track the FND was started. Immediately either nothing (to measure systematic drift), pH 7 solution as a control or different degradation media (pH 10 and pH13) were added. The FND was tracked for 360 min. During this time, the location in x, y and z directions were recorded. We calculated the diffusion coefficient as

a measure of how freely the particle moves for different degradation conditions for 5 different films. The results are shown in Figure 9 as well as Figures S7, S8 and S9 in the supplementary information. We show clearly that the particles in the strong degradation condition (pH 13, red) increase in freedom of movement for the first three hours compared to the other conditions. After that we observed a drop in D. The reason is that particles eventually sink to the bottom or go into solution (in this case we lose the particle since our tracking algorithm is not fast enough to track a freely floating particle). These results agree with the methods mentioned before. However, we obtain slightly different information here since this method reveals how freely particles can move in the polymer which can complement T1 measurements.

4.3.6 Degradation of PLA nanoparticles.

In order to demonstrate the capabilities of nanoscale sensing we performed measurements in PLA nanoparticles. Figure 10 shows the relaxometry results before and after the polymer particles have experienced degradation. In this configuration, it is possible to obtain information from single particles. Also in this case we were able to observe the expected decrease in T1 after degradation.

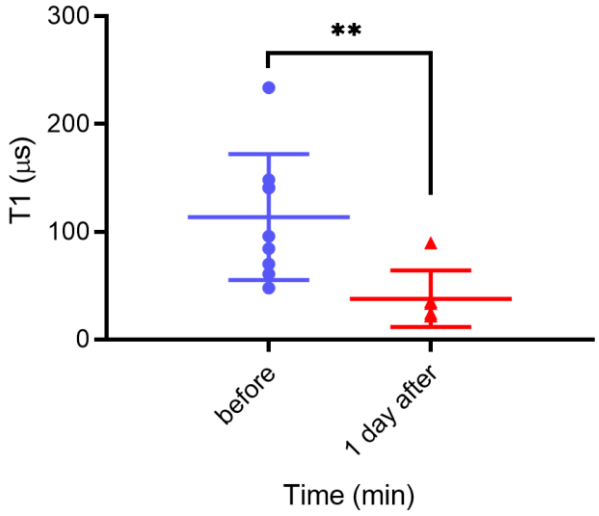

Figure 10. *T1 results of the degradation of PLA nanoparticles containing 70 nm FNDs before and after degradation at pH 4.5 for one day at 1 µM Gd3+. The data were analyzed using student's t test, and statistical significance was accepted at *p ≤ 0.05, **p ≤ 0.01.*

4.4 Conclusions

In this study, relaxometry measurements as well as diamond particle tracking was applied for the first time in the field of polymer degradation studies. Using very small amounts of diamond nanoparticles (0.1wt%), we were able to follow the degradation of PLA under different alkaline conditions. We also compared the T1 or magnetometry data with conventional methods including AFM, QCM, and FTIR. Using these techniques, we observed the changes in polymer film thickness, mass loss and chemical groups. Unlike the conventional methods relaxometry provides local measurements with nanoscale resolution. In addition, due to the stability of nanodiamond fluorescence this method allows long term tracking. T1 and tracking diamonds are expected to be also applicable in the degradation of other polymers, and even to explore changes in the polymers being endocytosed within the cells.

Acknowledgements

We would like to thank M. Wlodarczyk-Biegun for support with supervision and editing. RS acknowledges financial support via an ERC

starting grant (ERC STG – 714289) and a VIDI grant (016.Vidi.189.002). RL is thankful for a CSC scholarship from the Chinese government. AM is thankful for an LPDP scholarship from the Indonesian government.

References

1. Göpferich A. Mechanisms of polymer degradation and erosion. *Biomaterials.* **1996,** *17,* 103-14.

2. Nguyen, M. K.; Lee, D. S. Injectable biodegradable hydrgels. *Macromol Biosci.* **2010,** *10,* 563-79.

3. Chiellini, E.; Solaro, R. Biodegradable polymeric materials. *Adv. Mater.* **1996,** *8,* 305-313.

4. Li, Z.; Tan, S.; Li, S.; Shen, Q.; Wang, K. Cancer drug delivery in the nano era: An overview and perspectives. *Oncol. Rep.* **2017,** *38,* 611-624.

5. Alonso, M. J.; Cohen, S.; Park, T. G.; Gupta, R. K.; Siber, G. R.; Langer, R. Determinants of release rate of tetanus vaccine from polyester microspheres. *Pharm. Res.* **1993,** *10,* 945-53.

6. Gref, R.; Minamitake, Y.; Peracchia, M. T.; Trubetskoy, V.; Torchilin, V.; Langer, R. Biodegradable long-circulating polymeric nanospheres. *Science.* **1994,** *263,* 1600-3.

7. Gopferich, A.; Gref, R.; Minamitake, Y.; Shieh, L.; Alonso, M. J.; Tabata, Y.; Langer, R. Drug delivery from bioerodible polymers: systemic and intravenous administration. ACS Symposium Series 567; *American Chemical Society: Washington, DC,* **1994,** *15,* 242−277.

8. Kost, J.; Langer, R. Responsive polymer systems for controlled delivery of therapeutics. *Trends. Biotechnol.* **1992,** *10,* 127-31.

9. Mitragotri, S.; Lahann, J. Physical approaches to biomaterial design. *Nat. Mater.* **2009,** *8,* 15-23.

10. Fishbein, I.; Chorny, M.; Rabinovich, L.; Banai, S.; Gati, I.; Golomb, G. Nanoparticulate delivery system of a tyrphostin for the treatment of restenosis. *J. Control. Release.* **2000,** *65,* 221-9.

11. Brekke, J. H.; Olson, R. A.; Scully, J. R.; Osbon, D. B. Influence of polylactic acid mesh on the incidence of localized osteitis. *Oral. Surg. Oral. Med. Oral. Pathol.* **1983,** *56,* 240-5.

12. Yamashita, K.; Kikkawa, Y.; Kurokawa, K.; Doi, Y. Enzymatic degradation of poly(L-lactide) film by proteinase K: quartz crystal microbalance and atomic force microscopy study. *Biomacromolecules.* **2005,** *6,* 850-857.

13. Kearney, L. T.; Howarter, J. A. QCM-based measurement of chlorine-induced polymer degradation kinetics. *Langmuir.* **2014,** *30,* 8923-30.

14. Kister, G.; Cassanas, G.; Bergounhon, M.; Hoarau, D.; Vert, M. Structural characterization and hydrolytic degradation of solid copolymers of d, l-lactide-co-ε-caprolactone by Raman spectroscopy. *Polymer.* **2000,** *41,* 925-932.

15. Schirhagl, R.; Chang, K.; Loretz, M.; Degen, C. L. Nitrogen-vacancy centers in diamond: nanoscale sensors for physics and biology. *Annu. Rev. Phys. Chem.* **2014,** 65, 83-105.

16. Mamin, H. J.; Kim, M.; Sherwood, M. H.; Rettner, C. T.; Ohno, K.; Awschalom, D. D.; Rugar, D. Nanoscale nuclear magnetic resonance with a nitrogen-vacancy spin sensor. *Science.* **2013,** *339,* 557-60.

17. Maletinsky, P.; Hong, S.; Grinolds, M. S.; Hausmann, B.; Lukin, M. D.; Walsworth, R.L.; Loncar, M.; Yacoby, A. A robust scanning diamond sensor for nanoscale imaging with single nitrogen-vacancy centres. *Nat. Nanotechnol.* **2012,** *7,* 320-4.

18. Le Sage, D.; Arai, K.; Glenn, D. R.; DeVience, S. J.; Pham, L. M.; Rahn-Lee, L.; Lukin, M. D.; Yacoby, A.; Komeili, A.; Walsworth, R. L. Optical magnetic imaging of living cells. *Nature.* **2013,** *496,* 486-9.

19. Kaufmann, S.; Simpson, D. A.; Hall, L. T.; Perunicic, V.; Senn, P.; Steinert, S.; McGuinness, L. P.; Johnson, B. C.; Ohshima, T.; Caruso, F.; Wrachtrup, J.; Scholten, R. E.; Mulvaney, P.; Hollenberg, L. Detection of

atomic spin labels in a lipid bilayer using a single-spin nanodiamond probe. *Proc. Natl. Acad. Sci. U. S. A.* **2013,** *110,* 10894-8.

20. Gorrini, F.; Giri, R.; Avalos, C. E.; Tambalo, S.; Mannucci, S.; Basso, L.; Bazzanella, N.; Dorigoni, C.; Cazzanelli, M.; Marzola, P.; Miotello, A.; Bifone, A. Fast and Sensitive Detection of Paramagnetic Species Using Coupled Charge and Spin Dynamics in Strongly Fluorescent Nanodiamonds. *ACS. Appl. Mater. Interfaces.* **2019,** *11,* 24412-24422.

21. Ermakova, A.; Pramanik, G.; Cai, J. M.; Algara-Siller, G.; Kaiser, U.; Weil, T.; Tzeng, Y. K.; Chang, H.C.; McGuinness, L. P.; Plenio, M. B.; Naydenov, B.; Jelezko, F. Detection of a few metallo-protein molecules using color centers in nanodiamonds. *Nano. Lett.* **2013,** *13,* 3305-9.

22. Perona, Martínez, F.; Nusantara, A, C.; Chipaux, M.; Padamati, S. K.; Schirhagl, R. Nanodiamond Relaxometry-Based Detection of Free-Radical Species When Produced in Chemical Reactions in Biologically Relevant Conditions. *ACS. Sens.* **2020,** *5,* 3862-3869.

23. Simpson, D. A.; Morrisroe, E.; McCoey, J. M.; Lombard, A. H.; Mendis, D. C.; Treussart, F.; Hall, L. T.; Petrou, S.; Hollenberg, L. C. L. Non-Neurotoxic Nanodiamond Probes for Intraneuronal Temperature Mapping. *ACS. Nano.* **2017,** *11,* 12077-12086.

24. Kucsko, G. Maurer, P. C.; Yao, N. Y.; Kubo, M.; Noh, H. J.; Lo, P. K.; Park, H.; Lukin, M. D. Nanometre-scale thermometry in a living cell. *Nature.* **2013,** *500,* 54-8.

25. McGuinness, L. P.; Yan, Y.; Stacey, A.; Simpson, D. A.; Hall, L. T.; Maclaurin, D.; Prawer, S.; Mulvaney, P.; Wrachtrup, J.; Caruso, F.; Scholten, R. E.; Hollenberg, L. C. Quantum measurement and orientation tracking of fluorescent nanodiamonds inside living cells. *Nat. Nanotechnol.* **2011,** *6,* 358-63.

26. Morita, A.; Nusantara, A. C.; Martinez, F. P. P.; Hamoh, T.; Damle, V. G.; van, der, Laan, K. J.; Sigaeva, A.; Vedelaar, T.; Chang, M.; Chipaux, M.;

Schirhagl, R. Quantum monitoring the metabolism of individual yeast mutant strain cells when aged, stressed or treated with antioxidant. *arXiv* **2020,** *arXiv:2007.*16130.

27. Nie, L.; Nusantara, A. C.; Damle, V. G.; Sharmin, R.; Evans, E. P. P.; Hemelaar, S. R.; van, der, Laan, K. J.; Li, R.; Perona, Martinez, F. P.; Vedelaar, T.; Chipaux, M.; Schirhagl, R. Quantum monitoring of cellular metabolic activities in single mitochondria. *Sci. Adv.* **2021,** *7,* eabf0573.

28. Behler, K. D.; Stravato, A.; Mochalin, V.; Korneva, G.; Yushin, G.; Gogotsi, Y. Nanodiamond-polymer composite fibers and coatings. *ACS. Nano.* **2009,** *3,* 363-9.

29. Rendler, T.; Neburkova, J.; Zemek, O.; Kotek, J.; Zappe, A.; Chu, Z.; Cigler, P.; Wrachtrup, J. Optical imaging of localized chemical events using programmable diamond quantum nanosensors. *Nat. Commun.* **2017,** *8,* 14701.

30. Rehor, I.; Mackova, H.; Filippov, S. K.; Kucka, J.; Proks, V.; Slegerova, J.; Turner, S.; Van, Tendeloo, G.; Ledvina, M.; Hruby, M.; Cigler, P. Fluorescent Nanodiamonds with Bioorthogonally Reactive Protein-Resistant Polymeric Coatings. *Chempluschem.* **2014,** *79,* 21-24.

31. Huynh, V. T.; Pearson, S.; Noy, J. M.; Abboud, A.; Utama, R. H.; Lu, H.; Stenzel, M. H. Nanodiamonds with surface grafted polymer chains as vehicles for cell imaging and cisplatin delivery: enhancement of cell toxicity by POEGMEMA coating. *ACS Macro Letters,***2013,** *2,* 246-250.

32. Neburkova, J.; Vavra, J.; Cigler, P. Coating nanodiamonds with biocompatible shells for applications in biology and medicine. Curr. Opin. Solid. State. Mater. Sci. 2017, 21, 43-53.

33. Shenderova. O. A.; Shames, A.I.; Nunn, N. A.; Torelli, M. D.; Vlasov, I.; Zaitsev, A. Synthesis, properties, and applications of fluorescent diamond particles. *J. Vac. Sci. Technol. B. Nanotechnol. Microelectron.* **2019,** *37,* 030802.

34. Ong, S. Y.; Chipaux, M.; Nagl, A.; Schirhagl, R. Shape and crystallographic orientation of nanodiamonds for quantum sensing. *Phys. Chem. Chem. Phys.* **2017,** *19,* 10748-10752.

35. Hemelaar, S. R.; de, Boer, P.; Chipaux, M.; Zuidema, W.; Hamoh, T.; Martinez, F. P.; Nagl, A.; Hoogenboom, J. P.; Giepmans, B. N. G.; Schirhagl, R. Nanodiamonds as multi-purpose labels for microscopy. *Sci Rep.* **2017,** *7,* 720.

36. Yamashita, K.; Kikkawa, Y.; Kurokawa, K.; Doi, Y. Enzymatic degradation of poly(L-lactide) film by proteinase K: quartz crystal microbalance and atomic force microscopy study. *Biomacromolecules.* **2005,** *6,* 850-7.

37. Clegg, J. R.; Ludolph, C. M.; Peppas, N. A. QCM-D assay for quantifying the swelling, biodegradation, and protein adsorption of intelligent nanogels*. J. Appl. Polym. Sci.* **2020,** *137,* 48655.

38. Sauerbrey, G. Use of quartz crystals for weighing thin layers and for microweighing. *Zeitschrift. Für. Physic.* **1959,** *155,* 206-222.

39. Morita, A.; Hamoh, T.; Martinez, F. P. P.; Chipaux, M.; Sigaeva, A.; Mignon, C.; Laan, K. J. V.; Hochstetter, A.; Schirhagl, R. The Fate of Lipid-Coated and Uncoated Fluorescent Nanodiamonds during Cell Division in Yeast. *Nanomaterials (Basel).* **2020,** *10,* 516.

40. Levi, V.; Gratton, E. Exploring dynamics in living cells by tracking single particles. Cell. *Biochem. Biophys.* **2007,** 1-15.

41. Kikkawa, Y.; Fujita, M.; Abe, H.; Doi, Y. Effect of water on the surface molecular mobility of poly(lactide) thin films: an atomic force microscopy study. *Biomacromolecules.* **2004,** *5,* 1187-93.

42. Schusser, S.; Menzel, S.; Bäcker, M.; Leinhos, M.; Poghossian, A.; Wagner, P.; Schöning, M. J. Degradation of thin poly (lactic acid) films: Characterization by capacitance–voltage, atomic force microscopy,

scanning electron microscopy and contact-angle measurements. *Electrochim. Acta.* **2013,** *113,* 779-784.

43. Johannsmann, D. Viscoelastic, mechanical, and dielectric measurements on complex samples with the quartz crystal microbalance. *Phys. Chem. Chem. Phys.* **2008,** *10,* 4516-34.

44. Agarwal, M.; Koelling, K. W.; Chalmers, J. J. Characterization of the degradation of polylactic acid polymer in a solid substrate environment. *Biotechnol. Prog.* **1998,** *14,* 517-26.

45. Choi, K. M.; Choi, M. C.; Han, D. H.; Park, T. S.; Ha, C. S. Plasticization of poly (lactic acid (PLA) through chemical grafting of poly (ethylene glycol) (PEG) via in situ reactive blending. *Eur. Polym. J.* **2013,** *49,* 2356-2364.

46. Araque-Monrós, M. C.; Vidaurre, A.; Gil-Santos, L.; Bernabé, S. G.; Monleón-Pradas, M.; Más-Estellés, J. Study of the degradation of a new PLA braided biomaterial in buffer phosphate saline, basic and acid media, intended for the regeneration of tendons and ligaments. *Polym. Degrad. Stab.* **2013,** *98,* 1563-1570.

47. Park, S.; Abate, I. I.; Liu, J.; Wang, C.; Dahl, J. E. P.; Carlson, R. M. K.; Yang, L.; Prakapenka, V. B.; Greenberg, E.; Devereaux, T. P.; Jia, C.; Ewing, R. C.; Mao, W. L.; Lin, Y. Facile diamond synthesis from lower diamondoids. *Sci. Adv.* **2020,** *6(8),* 9405.

Supplementary information

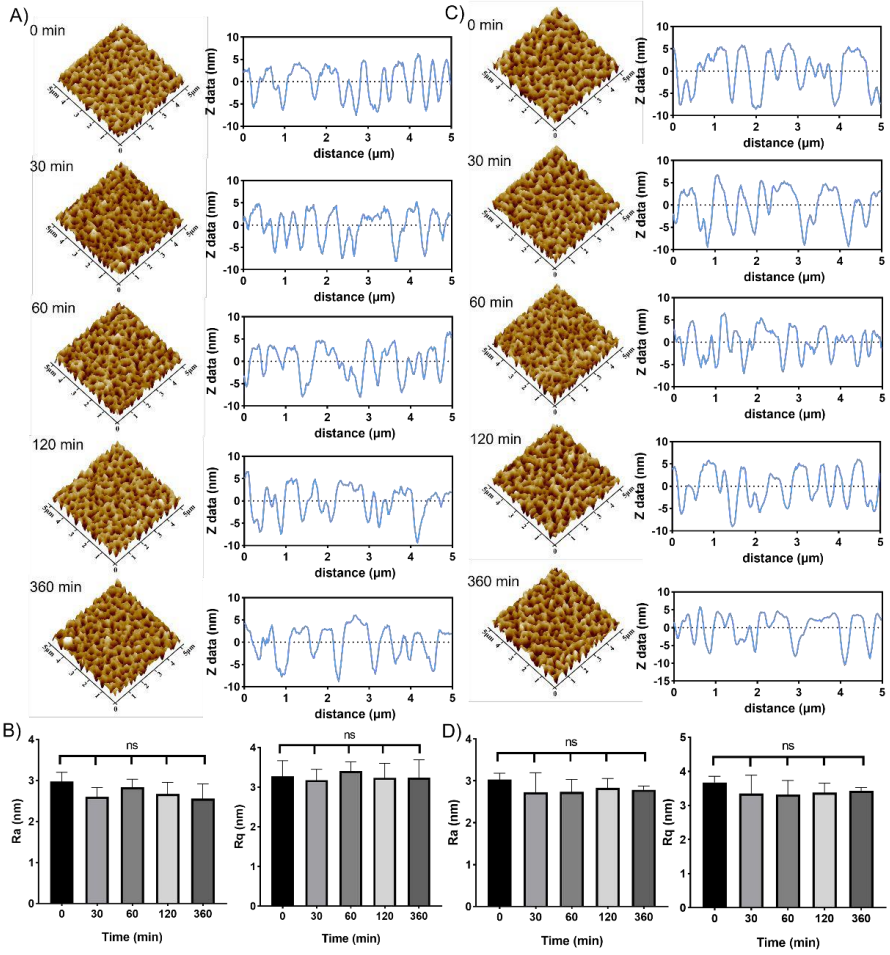

Figure S1. Contacting mode 3D AFM images of PLA film surfaces, z-profiles cross the surface were shown after PLA film was treated with pH 7 and pH 10 solution for 0 min, 30 min, 60 min, 120 min and 360 min. Corresponding surface roughness parameters, including arithmetic mean roughness Ra and RMS roughness Rq were calculated from the AFM images as well. (A) the PLA film before pH 7 solution degradation and the PLA film treated with pH 7 solution. (B) Ra and Rq of AFM images before and after pH 7 treatment. (C) the PLA film before pH 10 solution degradation and the PLA film treated with pH 10 solution. (D) Ra and Rq of AFM images before and after pH 10 treatment.

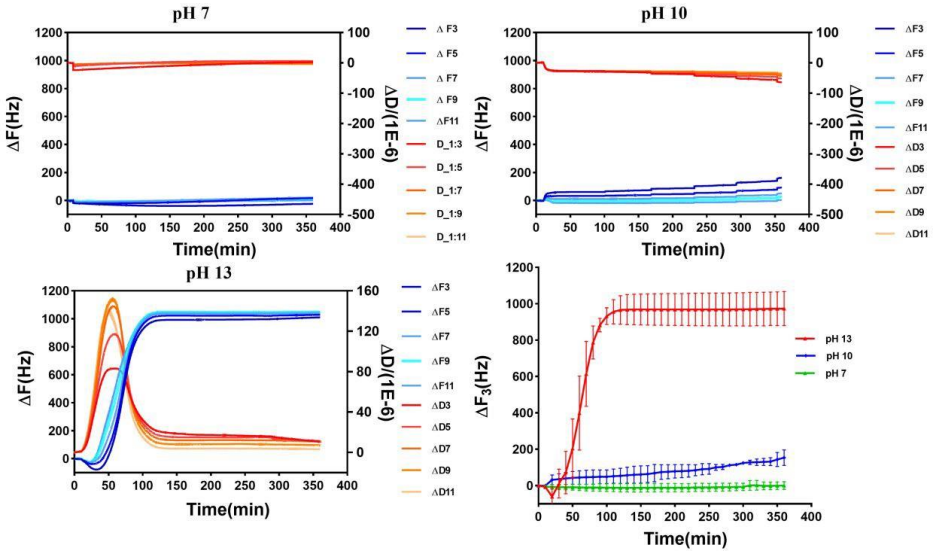

Figure S2. QCM-D monitoring of resonance frequency (ΔF, blue) and dissipation (ΔD, orange) at several overtones (n=3, 5, 7, 9 and 11) were obtained over time during pH 7 (a), pH 10 (b) and pH 13 (c) solutions at 25 °C. ΔF3 as a normalized frequency were compared in different experimental sets (d).

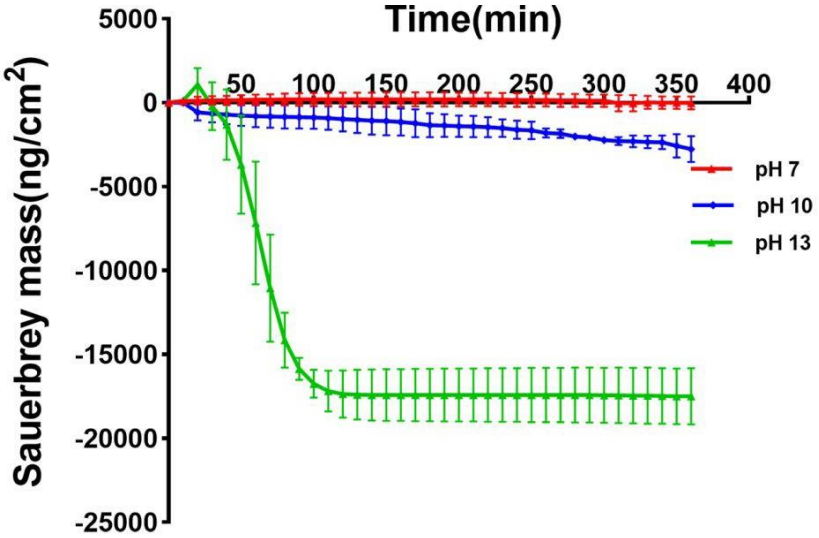

Figure S3. The mass versus time plot at pH 7, pH 10 and pH 13 solution at 25 °C, respectively. The mass data were obtained using the Sauerbrey equation (1) from ΔF data.

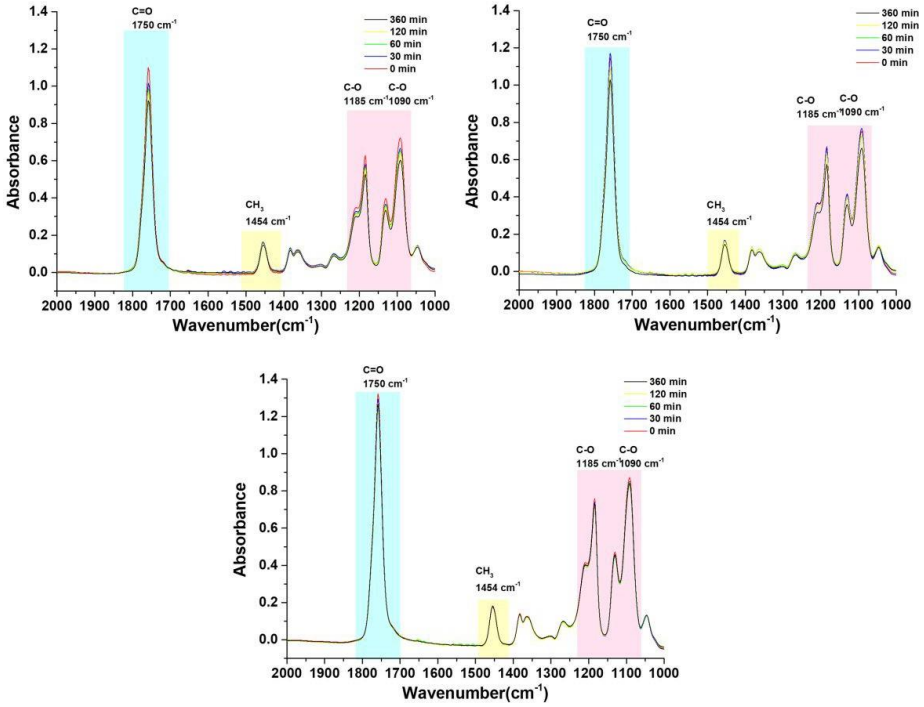

Figure S4. FTIR spectra during degradation was obtained from PLA thin films exposed to pH 13 (a), pH 10 (b) and pH 7 (c). The red line represents before degradation, the blue line, green line, yellow line, and black line represent 30, 60, 120, and 360 minutes after degradation, respectively.

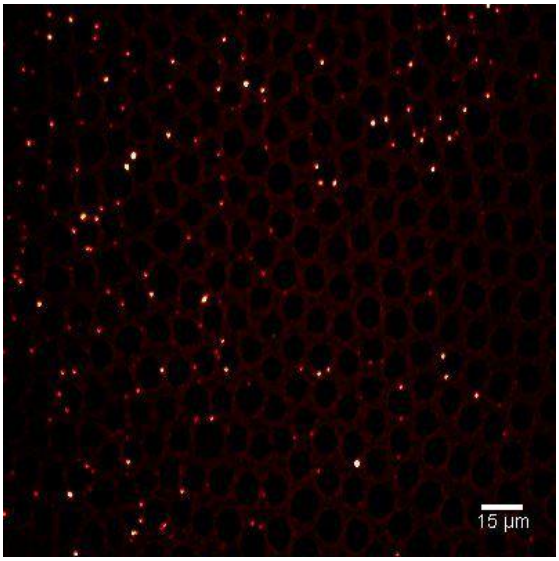

Figure S5. The PLA thin film mixed with 0.1wt% FNDs, red-white dots are FNDs, evenly distributed in the film.

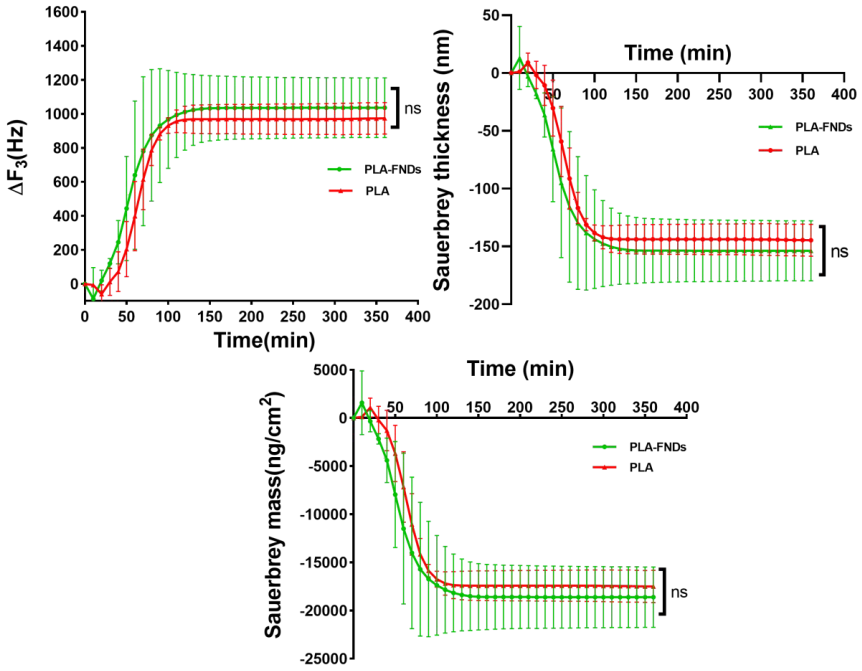

Figure S6. Comparison of degradation of PLA film and PLA with FNDs film after treatment of pH 13 solution, including changes in ΔF, Sauerbrey mass and Sauerbrey thickness. (Statistics were evaluated using Graphpad Prism 8.0.1 by multiple t tests, and $p \leq$ values 0.05 were considered as significant differences.)

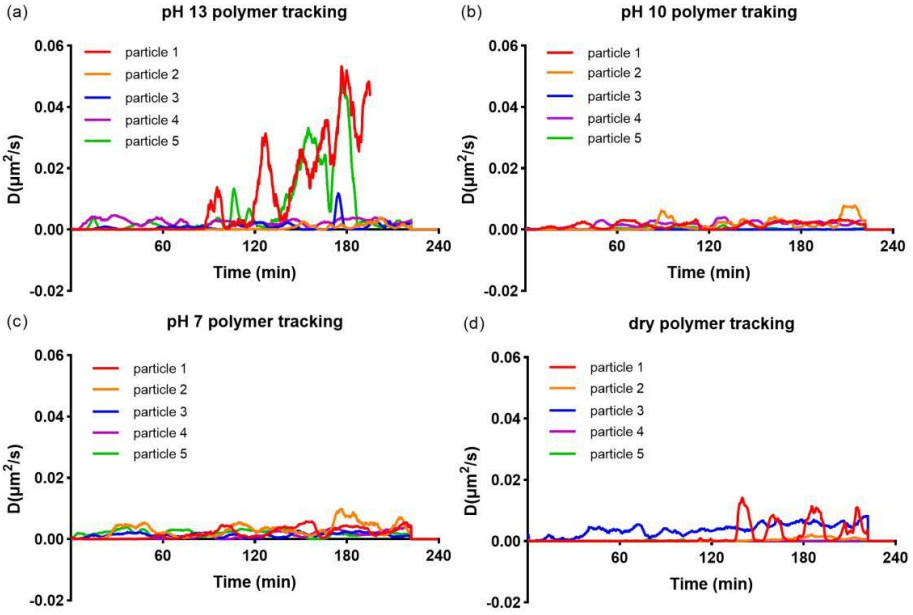

Figure S7. The diffusion coefficients of five FNDs tracking in each polymer film under pH 13 (a), pH 10 (b) and pH 7 (c), and dry film (d).

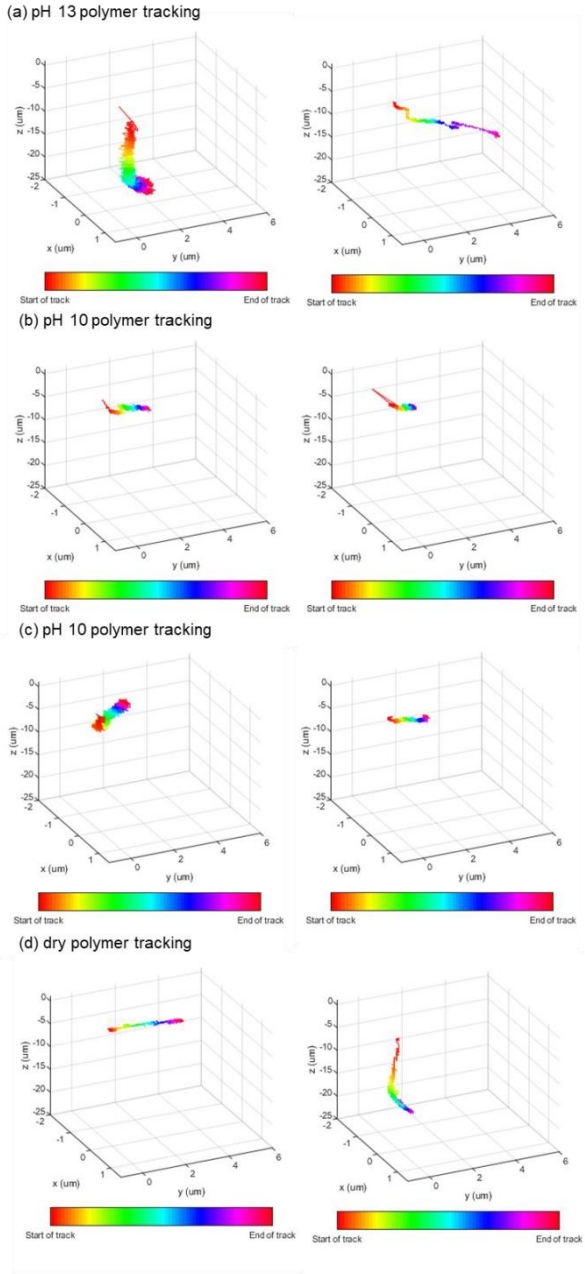

Figure S8. 3D trajectories for particle tracking, two typical FNDs trajectories of the polymer film were shown under pH 13 (a), pH 10 (b) and pH 7 (c), and dry film (d).

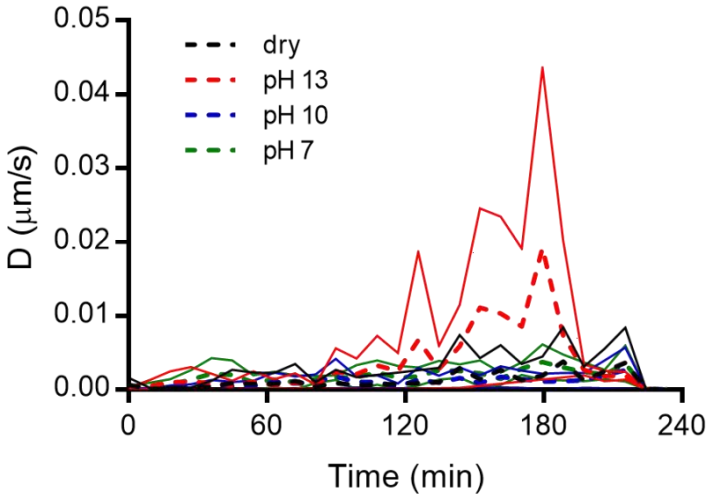

Figure S9. FNDs tracking results with error boundaries. The dotted lines represent the average of the tracks with the solid lines as the error boundaries based on the standard deviation.

Chapter 5

Applying NV center-based quantum sensing to study intracellular free radical response upon viral infections

Kaiqi Wu[+], **Thea A. Vedelaar[+]**, Viraj G. Damle, Aryan Morita, Julie Mougnaud, Claudia Reyes San Martin, Yue Zhang, Denise P.I van der Pol, Heidi Ende-Metselaar, Izabela Rodenhuis- Zybert and Romana Schirhagl

[+] These authors equally contributed to this work

Redox Biology, 2022, 52, 102279

https://doi.org/10.1016/j.redox.2022.102279

Abstract

Although viruses are known to modify the free radical composition in infected cells, the exact spatiotemporal and quantitative information of such change remains unknown. Although this information is important to understand the virus pathogenesis and design better anti-viral drugs or vaccines, obtaining it with the conventional free radical/ROS detection techniques is impossible. Here, we elucidate the utility of diamond relaxometry for studying the free radical response of baby hamster kidney-21 cells upon Semliki Forest virus infection. Specifically, we optically probe the alterations in free radical composition near infectious viruses via measuring the spin–lattice relaxation (T_1) of NV defect ensembles embedded in intracellular nanodiamonds. We performed measurements both at random locations as well as close to the virus entry by conjugating viruses to nanodiamond sensors. We observed alterations of T_1, which represent the intracellular free radical concentration during the viral replication process. Moreover, relaxometry is also used to monitor real-time free radical variation during the early infectious process.

Keywords: fluorescent nanodiamonds, free radicals, viral infections, diamond relaxometry, NV centers, ROS

5.1 Introduction

The pandemic of SARS-CoV-2 has once again highlighted the importance of virology research as it claimed millions of lives, affected billions of people and brought almost the entire world to a standstill. Redox imbalance in viral infections is an extensively studied topic. Most studies on oxidative stress in viral infections do not differentiate between paramagnetic and non-paramagnetic reactive molecules. But they assess the net amount of the reactive molecules in cells or evaluate their overall molecular and enzymatic response to probe the infection induced redox imbalance. However, this approach is not always useful and sometimes type/nature of an individual reactive species needs to be taken into account. For instance, although the amount of oxygen radical upon influenza virus infection has been shown to increase[1] similar effects for hydroxyl radicals have not been reported[2]. Another example would be the non-universal anti-viral activity of nitric oxide which changes depending on the virus it is interacting with[2]. Free radicals play a key-role during infection, virus mutation and disease pathogenesis[1-8]. Free radicals are extremely short lived[9] and are generated in small concentrations, which complicates studying them. Therefore, a method capable of real-time detection of the radical-specific variation in free radical amount with high spatial resolution can significantly boost virology research.

Conventionally, fluorescence-based assays[10, 11] or UV-VIS absorption spectroscopy techniques[12] utilizing a wide array of molecular probes are deployed to measure the amount of intracellular free radicals. Here, the amount of fluorescence or absorbance is directly correlated with the concentration of free radicals. In all such methods, conducting real-time, kinetic studies is impossible due to bleaching and irreversible reactions between the probes and the free radicals. Another approach is detecting the expression of genes encoding enzymes involved in coping with the oxidative stress (such as superoxide dismutase or catalase) using quantitative polymerase chain reactions (qPCR)[13]. Although this method can be specific for certain radicals, it does not provide any information on the spatial and temporal evolution of the free radical response of an individual host cell upon infection. Electron paramagnetic resonance (EPR) and magnetic resonance imaging (MRI), methods routinely used for studying

free radicals in chemistry, has never been used to study the cellular free radical/ROS response. The reason is that they are limited in sensitivity. This is especially crucial when high spatial resolution is required or only limited amounts of sample are available (inside of a cell for example).

Here, we demonstrate that diamond relaxometry can be an excellent technique to study intracellular free radicals upon viral infection. In free radical detection, this method offers distinct advantages in terms of biocompatibility, sensitivity[14], resolution, relatively low-cost equipment and lack of complex chemistries. Most importantly, internalized FNDs do not get consumed or bleached in a reaction, which makes real-time long-duration measurements possible. Moreover, this is the only method that simultaneously detects the real-time impact of viral infection on cytoplasmic transport via tracking the nanodiamond movement inside the cell. In this method, an optical readout of the magnetic environment can be acquired using the quantum sensing properties of the Nitrogen- Vacancy (NV) defect center in a diamond crystal[15-17]. Hence diamond relaxometry has a great potential to optically investigate the amount of intracellular free radicals. Unpaired electrons of free radicals offer magnetic noise to the NV centers embedded in fluorescent nanodiamonds (FNDs) ingested by cells. In fact, detecting free radical generation in wild-type and mutant yeast has recently been achieved[18].

Here, we optically probe the free radical response of host baby hamster kidney-21 (BHK-21) cells upon Semliki Forest virus (SFV) infection by measuring the relaxation time (T_1) of NV ensembles embedded in an intracellular FND conjugated to SFV as well as bare FNDs. Moreover, the location and duration of host cellular radical response during viral infection, and the impact of viral infection on the cytoplasmic transport is elucidated for the first time.

5.2 Materials and methods

5.2.1 Diamond relaxometry experiments to measure T_1 relaxation

Diamond relaxometry setup

To perform diamond relaxometry, we utilized a home-made relaxometry setup. The setup is in principle a confocal microscope with a few changes as described below. First, we implemented an acousto-optical modulator (Gooch & Housego, model 3350-199) to conduct the pulsing sequence shown in **Figure 1**. For focusing and light collection we used a 100x magnification oil-immersion objective (Olympus, UPLSAPO 100XO). 50 µW laser power measured on top of the objective lens was the optimal laser power for avoiding damage to the cells while being high enough to polarize the NV centers. The photons emitted by an FND are detected using an avalanche photodiode (Excelitas, SPCM-AQRH) after passing through a 600 nm long-pass filter.

Selecting an intracellular FND for T_1 measurements

Using a bright field camera (Thorlabs) we selected FND particles (Adámas Nanotechnologies, Inc., USA) well inside a cell with a brightness > 2 million photon counts/s. These nanodiamonds are very well characterized in the literature[21-23]. To avoid artifacts, we made sure, that there were no significant differences between the count rates of the different experimental groups. Such bright particles are clearly visible on background fluorescence originating from the biological material. This is different from commonly used diamond crystals that contain single NV defects[19,20]. While properties of selected NV centers are superb, there is a large variation in single defect quality and thus usually a preselection is needed. This approach is not practical for measurements in a biological system since we cannot reuse a particle as a sample is typically discarded after every experiment. Most importantly this would also make it impossible to compare different experiments on different cells and different particles. Hence FND containing ensembles of ~500 NV centers are used in this work. Thus, we always measure the sum of responses of many different NV centers in our measurements, which makes measurements more robust and repeatable.

Experimental protocol

To experimentally determine the T_1, we use the spin relaxometry protocol developed by Tetienne *et al*.[20] In short, during this sequence we pump the NV centers to the bright state and probe after different dark times if it is still there. The biggest advantage of this sequence is that it does not require microwaves. In biological samples, the water in the cell culture medium absorbs the microwaves. This not only deteriorates the signal but also leads to thermal dissipation. During a T_1 measurement we first polarize the NV centers ensemble in the 70 nm FND ingested by the BHK-21 cells using 5 µs pulse of a 532 nm laser. Then, we turn the laser off for a predefined time interval, known as dark time, which varies between 0.2 µs to 10^6 µs. The laser pulse sequence used in this work for exciting the NV ensemble is shown in **Figure 1** (green). After exciting the NV ensemble, photons emitted from an FND are collected using a photodetector. The number of photos hitting the detector is plotted against the dark time as shown in **Figure 1** (red). Each individual measurement takes some hundreds of microseconds. However, to improve the signal to noise ratio we repeated the measurement 10,000 or 85,000 times depending on the experiment. To record the location and to avoid losing the particle we automatically pause every 5 seconds to track and recenter the particle. The entire sequence takes around 10 min for 10,000 and 85 min for 85,000 repetitions.

Data analysis

Once the data acquisition is complete, the data was processed further to quantify the T_1. The model we used to fit the T_1 data was established earlier[21] and is described by

$$PL(t) = I_{inf} + C_a e^{-t/Ta} + C_b e^{-t/Tb} \text{ where } T_1 = \max(Ta, Tb)$$

Technically there are hundreds of NV centers in every particle. To simplify the fitting procedure the relaxation time of the ensemble is approximated to have two components: the NV centers with shorter (Ta, closer to the surface or in a more disturbed environment) and one with longer T_1 ((Tb) deeper in the crystal or less perturbed)[22]. Between the two constants, the longer T_1 time was selected for quantification because it is more sensitive to changes of the NVs' surrounding. This model and some of the experimental parameters was determined by Perona Martinez et al.[21]

by testing the model's ability to determine known concentration in a controlled environment.

5.2.2 Cell and virus model

BHK-21 cells were maintained in Roswell Park Memorial Institute (RPMI)-1640 medium (Life Technologies, Breda, The Netherlands) supplemented with 10% fetal bovine serum (FBS), 1% Penicillin/streptomycin and 1% Glutamax at 37°C and 5% CO_2. All the culture medium components were purchased from Gibco, Life Technologies, the Netherlands. We used active Semliki Forest Virus (SFV) (clone SFV4 produced as in[23]) and inactivated viruses. Inactivated SFV was obtained by UV irradiating (Miller) the SFV stock solution for 2 h. The inactivation was confirmed using a $TCID_{50}$ assay where the virus titer was found to be below the detection limit of the assay.

To prepare the fluorescently-labeled virus, sucrose purified SFV ($TCID_{50}$ titer: 2.8×10^{10} $TCID_{50}$/mL) was labeled with 3,3'-Dioctadecyloxacarbocyanine perchlorate (DiO) (Vybrant, Thermo Fisher Scientific, the Netherlands) following the protocol described by Hoornweg *et al*.[24] Specifically, 25 µl of SFV stock solution was mixed with 2 µL 1mM of DiO cell-labeling solution in a final volume of 50 µL. After 10 minutes of incubation at room temperature in the dark, the unattached dye was removed by a Sephadex G-50 Fine column (Pharmacia). HNE buffer (5 mM HEPES, 150 mM NaCl, 0.1 mM EDTA, pH 7.4) was used to equilibrate the column. DiO-labeled virus was stored at 4°C and used within 2 days. The effect of DiO labeling on the virus titer was determined using the fifty-percent tissue culture infective dose ($TCID_{50}$) assay where the titer was found to be 2×10^8 $TCID_{50}$/mL post labeling. Individual virus particles labeled with DiO were further characterized by fluorescence microscopy (Delta Vision Elite). For the microscopic analysis, 100 µl of 100-times diluted DiO-labeled SFV (DiO-SFV) solution were added to one quarter of the glass bottom petri dish and imaged with a 488 nm laser. Emission was collected by a 100× oil immersion objective with a numerical aperture of 1.40 and imaged through a FITC filter and a charge-coupled-device camera. Image analysis (intensity-particle number) was carried out by using Particles Analyzer plugin of ImageJ (Fiji, fiji.sc/) as shown in the **Figure S1a**.

5.2.3 SFV-FND conjugates

The biotin-streptavidin technique was used to achieve SFV conjugation with FNDs because of its specificity and robustness[25-28]. Specifically, 50 µL of SFV stock solution was mixed with 1 µL freshly prepared 5 mM of Sulfo-NHS-LC-Biotin (EZ-Link, ThermoFisher Scientific) solution for 2 h at room temperature. Unbound biotinylation agent was removed by micro-dialysis (3.5K MWCO, Pierce, Thermo Scientific) against HNE buffer for 4 h at room temperature. Subsequently, 10 µL biotinylated SFV ($TCID_{50}$ titer: 3×10^7 $TCID_{50}$/mL) was added to 10 µL SA-FND (100 nm, 1mg/mL in PBS, Adámas Nanotechnologies, Inc., USA), then the mixture was incubated at 25℃ for 2 h. The SFV-FND conjugates were used for further experiments without further purification. To examine the conjugating efficiency of SA-FND with biotinylated SFV, the SFV was firstly modified by Biotin, then labeled by DiO. The resulting DiO labeled biotinylated SFV was then conjugated SA-FND using the same protocol. After this, the mixture (DiO-SFV-FND) was diluted 10 times by PBS and examined by fluorescent microscope (DeltaVision Elite) through FITC and A594 filters, followed by image analysis using FIJI.

5.2.4 Virus titer quantification

Virus titer of the SFV (infectious, inactivated, fluorescent-labeled) stock solution was determined using the $TCID_{50}$ assay. $TCID_{50}$ is the dilution of the virus stock required to infect 50% of the given cell population. In this assay, 40,000 cells plated in flat-bottom 96 well plates (Corning Costar) were infected with 10^{-1} through 10^{-12} dilution of SFV stock solution made with 2% (FBS) RPMI medium. At 1-hour post infection (hpi), 150 µl of 10% (FBS) medium was added over the cells. Every 24 hours until 72 hpi, the cells were examined for signs of SFV induced cytopathological effects (CPE) using a light microscope (Leica DMIL LED). The numbers of live and dead wells were counted and further used to calculate the $TCID_{50}$ of the initial virus stock solution by the Spearman-Kärber algorithm given by Hierholzer and Killington[29].

5.2.5 Measuring free radical response of BHK-21 cells to SFV infection at discrete timepoints

The general intracellular free radical response of BHK-21 cells was measured by sequentially incubating FND and SFV with host cells. One day before the experiment, 1 µg/ml 70 nm FND suspension (10% FBS + 90% RPMI-1640 medium) was added to 20,000 cells in one quarter of a glass bottom petri dish (Greiner bio-one, Germany). The FND suspension was made using a protocol established in our group[19-20]. Then host cells having intracellular FNDs were infected with SFV with a multiplicity of infection (MOI = number of virus particles / number of cells ratio) of 20. Specifically, cells were covered with 100 µL infection medium (2% FBS + 98% RPMI-1640 medium + virus particles). We made five such dishes for every experiment. In addition, we prepared another petri dish where cells were treated with medium alone without any virus particles. This was treated as a control sample. Here we used three experimental groups where cells were treated with (i) infectious SFV, (ii) UV-inactivated SFV and (iii) plain medium at the 0 hour timepoint.

To investigate the intracellular free radical response near the viral particles, virus-diamond conjugates (SFV-FND) were used to infect host cells. 40,000 BHK-21 plated in a four-quartered glass-bottom petri dish (Greiner bio-one, Germany) was incubated with SFV-FND with the MOI (MOI=20). In this experiment, SA-FND without viral particles treated BHK-21 cells was set as a control group. Here three experimental groups were cells treated with (i) infectious SFV-FND, (ii) inactivated SFV-FND and (iii) SA-FND at the 0 hour time point.

At 1 hpi, infection medium was removed, and cells were supplemented with 400 µl of 10% medium. After this, cells were maintained in the incubator except during the treatment or the T_1 measurement. At every timepoint (control, 2, 4, 6, 8, 10 hpi), we removed one petri dish from the incubator and measured T_1 relaxation on four different FNDs ingested by four different cells in the same petri dish. Three measurements on a single petri dish were completed within a maximum of one hour after removing it from the incubator. Such an experiment was repeated three independent times per group.

5.2.6 Investigating pseudo real-time variation in intracellular free radical amount post SFV infection

The real-time variation of intracellular free radicals near viral particles was investigated by two steps. First, seeded BHK-21 cells were incubated with 100 µL SFV-FND (MOI=20, SFV equiv.) for 45 minutes at 4°C. Later, unattached SFV-FND were removed by washing the cells three times with cold RPMI. BHK-21 cells were kept on an ice bath with cold cell culture medium until further experiments. Then we applied the T_1 measurement cycle for 85,000 times in 85 min using the same particle (as described in **Section S8**). For comparison, a rolling window experiment was also performed on the inactive SFV-FND conjugates or only SA-FND attached BHK-21 cells. Each experimental group was repeated 9 times.

The data were analyzed using a "moving window algorithm" to determine the temporal evolution of T_1 in healthy and treated cells. Details of the algorithm are explained in **section 4.3.8**. The output of the algorithm is smoothened using GraphPad Prism. (GraphPad Software, San Diego, California USA, www.graphpad.com).

5.2.7 Imaging virus entry into the cell

To investigate how much time is required for SFV and SFV-FND to enter the cells, the virus-tracking experiments were performed. Briefly, BHK-21 cells were seeded one day before the experiment. Next day, cells were washed twice with cold phenol-red RPMI. Glucose oxidase (GLOX) was added to prevent photo toxicity as elaborated in the literature[30,31]. Subsequently, 100 µL DiO- SFV or DiO-SFV-FND (~10^7 $TCID_{50}$/ml SFV equiv.) was added to BHK-21 cells and cells were incubated for 45 minutes at 4°C. Later, unattached virus or conjugates were removed by washing the cells three times with cold RPMI. Subsequently, the temperature was rapidly elevated to 37 °C using a thermostatic stage. This temperature was maintained constant throughout the experiment. The moment of the temperature shift to 37 °C is referred to as 0 minute time point. DiO-SFV was detected with a FITC filter, while DiO-SFV-FND was detected with FITC and A594 filters, separately. An image series of the fluorescent emission was recorded with a charge-coupled-device camera at 1 frame per 5s for a total of 25 min. Before and after fluorescence imaging, the localization of

the nucleus and plasma membrane of the cell was determined by differential interference contrast (DIC) imaging. As shown in **Figure S2** and **Figure S3**, the cell shape and position did not change significantly during the fluorescence recording period.

As a negative control, BHK-21 cells were treated with 20 mM ammonium chloride (Sigma) before incubation with virus or virus-diamond conjugates[30,31]. To make sure that the long duration imaging does not bleach the DiO-SFV fluorescence, imaging was also performed on DiO-SFV and DiO-SFV-FND alone. The data produced during the experiments consist of a time series of ~ 300 images that show several fluorescent particles in the same imaging field. To further analyze the change in fluorescence intensity as a function of time, first, we manually found the coordinates of the possible fusion events where fluorescence intensity was observed to increase. Next, a region of interest (ROI) was formed near these coordinates to calculate the intensity value using Fiji (fiji.sc/).

5.2.8 Determining the relative location of DiO-SFV-FND

To obtain the position information of the conjugates, especially the location of FND where we carried out our T_1 experiments on SFV-FND, BHK-21 cells were incubated with DiO-SFV-FND. After different times (0, 2, 4, and 6 hpi) co-culturing, the cells were fixed with 3.7% paraformaldehyde solution for 15 min, followed by staining the endosomes using EEA1 monoclonal antibody (4 μg/mL, ThermoFisher), and goat anti-Rabbit IgG (H+L) cross-adsorbed secondary antibody, Alexa Fluor 350 (5 μg/mL, ThermoFisher), respectively. To be noted, 0 hpi samples were obtained by attaching DiO-SFV-FND on BHK-21 cells on ice bath for 45 min, immediately following by the same fixing and staining protocol. The cells were then imaged using a fluorescent microscope (DeltaVision Elite). Signals from DiO, FND, and stained endosomes were obtained with FITC, A594, and DAPI filters. Images were analyzed using FIJI to determine the relative position for conjugates and endosomes.

5.3 Results and discussion

5.3.1 Using diamond relaxometry, SFV - BHK-21 as a model system

SFV is a positive-stranded RNA virus of the genus Alphavirus of the *Togaviridae* family and one of the least pathogenic alphaviruses for humans[32]. Its popularity stems from its broad host range and similarities to other pathogenic viruses such as chikungunya virus and O`Nyong-Nyong virus. Moreover, SFV grows to high titer in cultured cells and one does not require high containment laboratory facilities to work with it, which makes it a very practical virus[24]. Likewise, BHK-21 is a widely used cell line in virology research and it ingests FNDs without any additional procedure. Moreover, BHK-21 cells have also been shown to be very permissive to SFV by Helenius *et al* and they are commonly used to propagate and to study this virus. It has been shown that the entry of SFV in BHK-21 occurs within an hour after infection and infection proceeds very rapidly as virus progeny can be observed in the medium within three hours post infection[33]. Hence, BHK-21 and SFV is a perfect model system for this work.

Next, we briefly explain the relevance of diamond relaxometry in free radical sensing. A schematic representation of probing general intracellular free radical response and free radical response near viral particles of BHK-21 upon SFV infection is shown in **Figure 1**. The core principle of this method is that the transition between polarized and equilibrium state changes based on the spin noise from radicals in its surrounding. The electron energy level diagram and the detailed photophysics of the NV relaxometry is further explained in supplementary information (S) in **Section S4**.

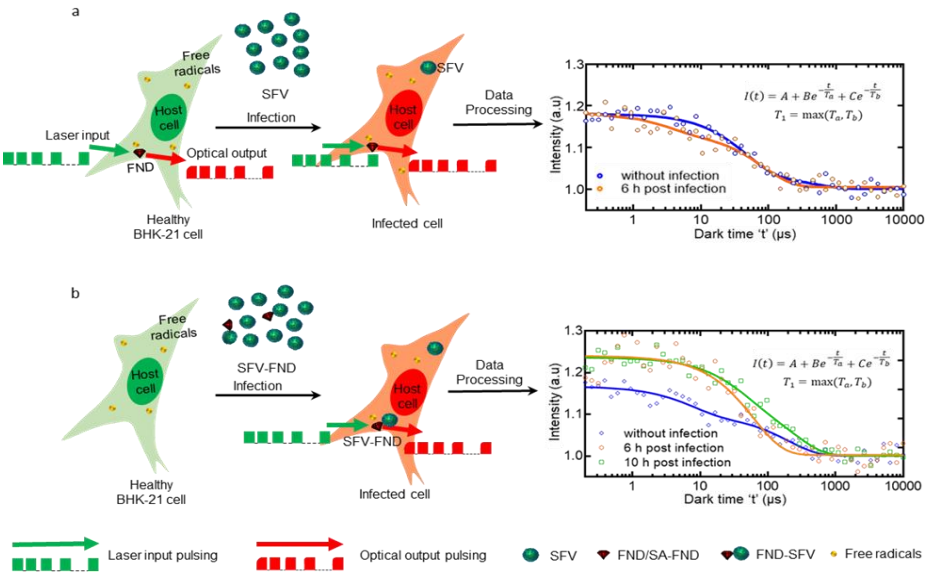

Figure 1. *Schematic representation of probing general intracellular free radical response (a), and free radical response near viral particles (b) of BHK-21 upon SFV infection using relaxometry.*

5.3.2 SFV-FND conjugates

The biotin-streptavidin interaction is widely used in biological experiments, especially in the biohybrid materials field[25-27,34]. Here, we used the interaction between biotin and streptavidin to conjugate SFV and FND (**Figure 2a**). As shown in **Figure 2b**, Biotin-SFV was labeled with DiO (green color), and SA-FND yielded red color. The yellow dots indicate the merged signal of DiO-SFV and SA-FND, which represents the colocalization of SFV and FND. The viral particles are 10-fold excess over FND particles to exclude the influence of free FND on the following T_1 experiment on SFV-FND conjugates. The number of viral and diamond particles was calculated using the methods as described by Hilde et al.[31] and Barton et al.[35], respectively. It can be clearly seen that all the FND particles are colocalized well with SFV, while some free viral particles can be observed individually.

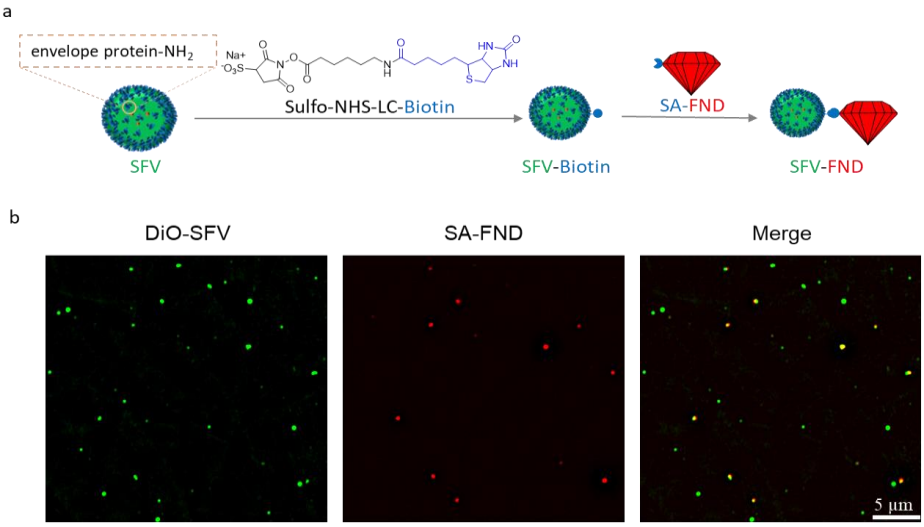

Figure 2. *(a) Schematic representation of SFV-FND formation. (b) Represent fluorescent images of SFV-FND conjugates.*

5.3.3 Kinetics of virus entry into the cell, infection duration and determining the degree of oxidative stress caused by SFV infection

After determining the titer of the virus stock solution to be ~ 2 x 10^9 $TICD_{50}$/mL, we measured how long it takes for a virus particle to enter the BHK-21 cells. Here we used a method previously reported by Hoornweg et al.[36] In particular, we monitored the fluorescence intensity of the DiO-label attached to the sucrose purified SFV that was added over the BHK-21 cells. A time-lapse image sequence in **Figure 3a** shows the sudden burst in fluorescence around ~600 seconds into the experiment. This indicates the virus membrane fusion as the fluorescence intensity increases due to the dilution of the probe in the endosomal membrane. The self-quenching property of DiO dye was proven in **Figure S1c**. **Figure 3b** shows the fluorescence intensity of DiO-labelled virus when cells were treated with NH_4Cl, which inhibits the virus fusion[37]. This is a negative control used to confirm the association between the fluorescence burst and the virus fusion.

In addition, the entrance of virus-diamond conjugates was also performed to check whether the conjugation will affect the entrance events of viral particles. **Figure 3e** shows the sudden increase of the DiO intensity at around 800 seconds. This is around 200 s delay compared with DiO-SFV group. According to Kennie's report that the mean endocytosis and fusion time in SFV-BHK-21 cells model is 10 min and 4 min[38], respectively. The fusion of conjugates happens around 800 seconds, which means the total time for endocytosis and fusion, and this event is in the range of previous reports. While **Figure 3f** shows that NH_4Cl also inhibits the fusion of SFV-FND. In conclusion, the characteristic timing of early infection of the virus is similar for conjugates. There is around 4 times fluorescence increase for DiO-SFV's fusion, while there is only 2 times increase for DiO-SFV-FND group (**Figure 3d, h**). One possible reason is that viral particles were modified with some biotin reagent before DiO staining, this step may decrease the staining effect. Additionally, the attached particle reduces the space that is available for the label as well. Furthermore, it was confirmed that optical bleaching of the DiO does not occur under the experimental conditions we used (**Figure 3c & g**).

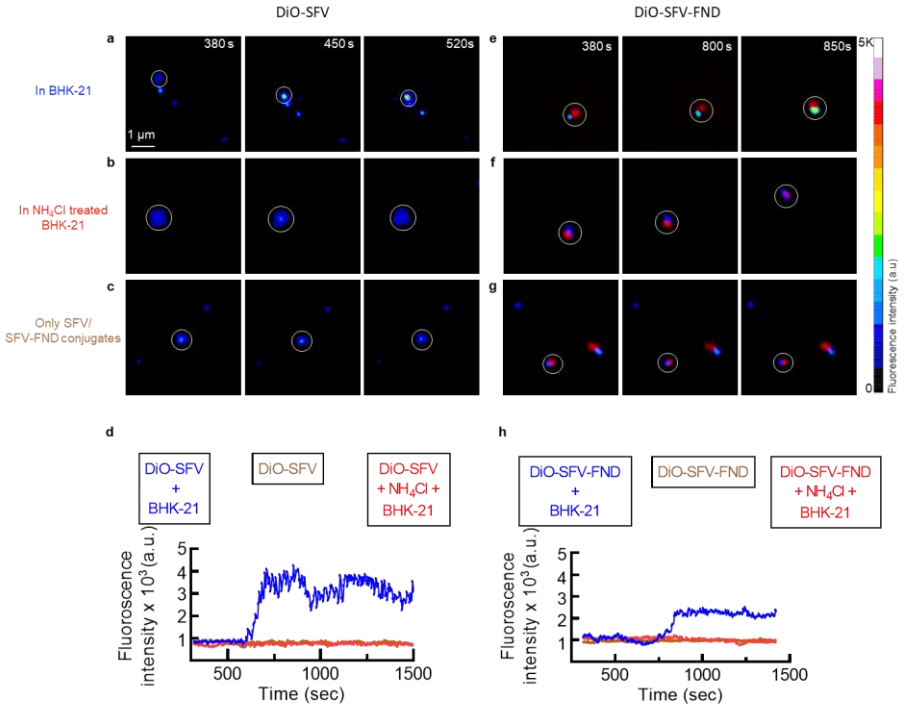

Figure 3. *The time required for SFV and SFV-FND to enter the cell. Representative time-lapse image sequences demonstrating the change in intensity of the DiO fluorescence after (a-c) adding the DiO-SFV or (e-g) DiO-SFV-FND to the cells. In (b) and (f) we show the time series when the uptake is inhibited with NH_4Cl. (c) and (g) show the respective particles in an empty Petri dish (control). Change in normalized fluorescence intensity with respect to time. (d) and (h) show the data for DiO-SFV and DiO-SFV-FND respectively. (a complete time series is shown in the supplementary material in* ***Section S2****).*

5.3.4 Measuring free radical response of BHK-21 cells to SFV infection at discrete timepoints at random locations

Next, we investigated the general free radical response of BHK-21 cells during SFV infection at a random location. Here, we infected the cells which already contained intracellular FNDs with SFV with a MOI of 20. MTT and morphology assays (**Figure S11a-d**) showed that this infectious condition has no influence on cell viability before 10 hours post infections. We did not observe any significant changes in radical loads in random locations of untreated cells (negative control), cells incubated with UV-inactivated virus particles, and cells challenged with infectious virus particles.

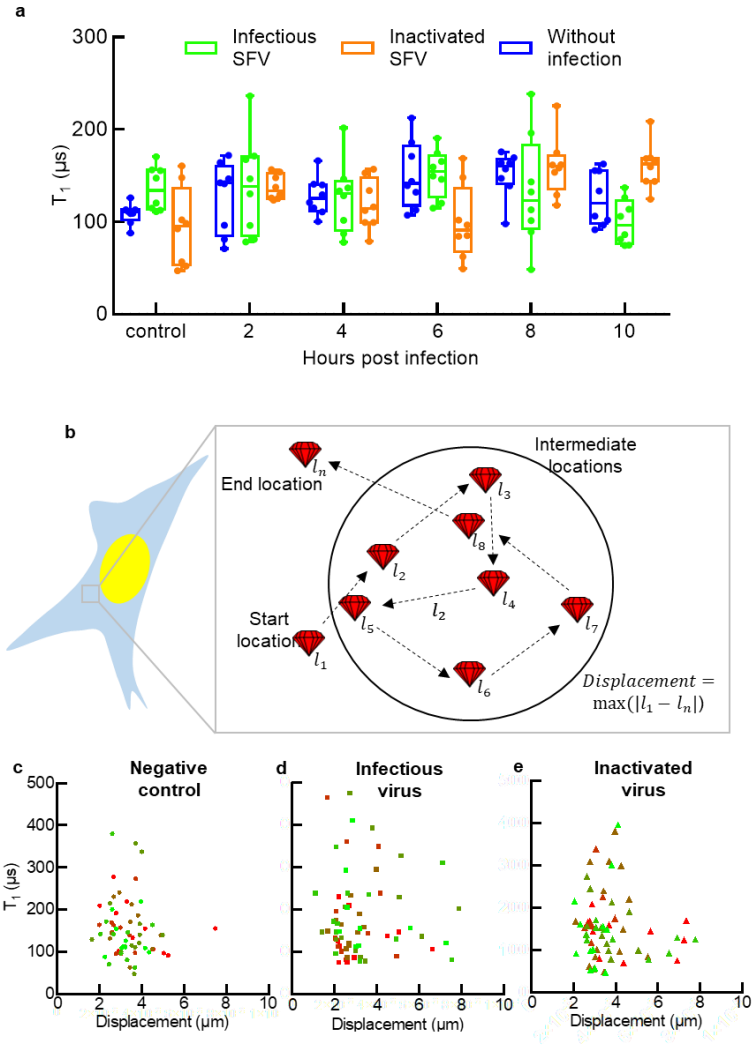

Figure 4. Individual T_1 measurements recorded every 2 h post infection (hpi) till 10 hpi in untreated cells (negative control), incubated with inactivated SFV and challenged with infectious SFV. All the timepoints across all the groups have at least 8 independent measurements. (b) Graphical representation of the FND movement within the cell cytoplasm to evaluate whether more active areas of greater movements were experiencing different T_1 times. We plot T_1 relaxation correlated with the maximum FND displacement for the cells treated with (c) plain cell-culture medium (negative control), (d) infectious SFV and (e) inactivated SFV group. Green and red color represent 0 hpi (time control) and 10 hpi, respectively. The off-green and red colors indicate the intermediate timepoints. Plots in c-e, have ~ 40 data points each obtained in three independent experiments.

During relaxometry measurements (**Figure 4a**) we did not observe anysignificant differences between radical loads at random locations. While applying the pulsing sequences on an intracellular FND for measuring the relaxation time (T_1), we continuously track the movement of the FND within the cell cytoplasm. Specifically, after every three to five seconds, we scan the fluorescence intensity within the 2 x 2 x 1 µm volume around the last known position of the particle. Subsequently, the new position of the FND is determined in two steps- (i) using a gaussian approximation to determine the brightest voxel in X and Y direction (ii) finding the brightest voxel at different Z coordinates for the X and Y coordinates obtained in the previous step. Tracking FND's movement within the cytoplasm allows us to further investigate the effect of viral infection on cytoplasmic transport. Diffusion of viral genetic material within the cytoplasm has been an important topic of experimental or computational investigation[39-42] as viral genetic material needs to be transported from outside of the cell to the nucleus in order to initiate the viral activity. On the other hand, diffusion of small molecules within the cytoplasm using electron spin resonance[43] or fluorescence-based imaging methods[44,45] has also been a topic of great interest. Most of the experimental work in these areas utilizes fluorescent labels, which are prone to bleaching. Moreover, these studies focus on movement of a single small molecule in the cytoplasm and no studies explore the systemic alterations in the cytoplasmic transport caused by the external stimulus (viral infection in this case).

Cytoplasmic transport can be assessed by a variety of ways such as quantifying the particle velocity, diffusion rate or displacement. Here, we quantify the maximum diamond displacement within the cell as shown in **Figure 4b**. First, we manually identified the particle, hence it's coordinates at the starting position l_1, within the cell at the beginning of the experiment. Then we optically followed the particle to track its coordinates li while the T_1 measurements were being recorded. Then we calculated the maximum distance traveled by the particle with respect to the initial position. The plots in **Figure 4c-e** depict T_1 relaxation against the maximum displacement determined for every individual FND for all measured timepoints. The idea behind this was to see whether areas with increased activity (indicated by displacement) would differ in T_1. From the results it can be clearly seen that all the points form a dense cluster for the negative control group where T_1

and the maximum displacement varies between 100 – 200 μs and 2 – 4 μm respectively. On the other hand, two components influencing the maximum displacement are (i) physical movement of an FND and (ii) an uncertainty in optical refocusing deployed for diamond tracking. We recorded a maximum displacement of ~ 1-2 μm even for a stationary particle placed in a dry petri dish. A similar cluster was observed for the inactivated virus and infectious virus group. Interestingly, the data points in those two groups were found to be more scattered compared to the negative control group indicating that FND movement in the cytoplasm is elevated upon introduction of the external stimulus. In **Figure 4c–e**, green and red color represent the control and 10 hpi timepoint respectively whereas color shades in between green and red indicate the intermediate timepoints. From **Figure 4c-e** it is clear that, T_1 x displacement plane is not divided in "distinct colors" which mean that no correlation between FND movement and the hpi can be drawn.

This method can easily be extended to both quantitatively and qualitatively investigate the cytoplasmic transport. Due to FND's photostable fluorescence, the same FND can be tracked continuously before and up to ~24 hours (based on the work in our group) after adding the virus. Uncertainty in optical refocusing can also be minimized by suitably modifying the tracking algorithm. Such measurements can potentially reveal the diffusion rate and particle velocities at high time resolution.

5.3.5 Position of SFV-FND conjugates

In the previous section we investigated free radical generation at a random location which is not necessarily close to the point of virus entry. Here, virus-diamond conjugates were formed to investigate the intracellular free radical response near viral particles, as diamond can detect the magnetic noise within 10 nm range. To clarify the position of SFV-FND conjugates and the location where we carried out our T_1 experiments, BHK-21 cells were incubated with DiO-SFV-FND for different times, followed by a fixing and staining process. For the control group, the uptake of DiO-SFV-FND conjugates was blocked when the temperature was lowered to and kept at 4 ℃ for 1 h. As shown in **Figure 5a** (0 hpi), the conjugates (red and green dots) are not colocalized with the endosomes (blue dots), and the location of conjugates is closer to the cell membrane. This is consistent with

previous literature which report the timing of virus entrance[38]. The conjugates can be found in the endosomes at 2, 4, and 6 hours post infection. As shown in **Figure 5a** (2, 4, and 6 hpi), FND, endosomes, and part of SFV colocalized well. Also, part of the green signals appears out of the endosome. This could be some DiO dye interacting with other intracellular lipids after membrane fusion occurred. FNDs are always colocalized well with endosomes. It is worth noting that replication of alphaviruses, including SFV, takes place in cytoplasmic viral factories at the outside surface of endosomes after membrane fusion[46]. To conclude, we can investigate the free radical response of BHK-21 cells when replication of genome happens by using SFV-FND, as demonstrated in **Figure 5c**.

5.3.6 Measuring the free radical response of BHK-21 cells to SFV-FND infection at discrete timepoints near viral particles

We investigated the intracellular free radical response near viral particles using SFV-FND conjugates at discrete time points post SFV infection with MOI 20. Comparing with **Section 4.3.4** where measurements were conduct on bare FND at random intracellular locations, measurements on SFV-FND reveal the radical response near viral particles. As a result, T_1 values detected using SFV-FND are more affected by the infectious events. **Figure 5b** indicates the relatively lower T_1 value at 2 hpi (145 μs), compared with 0 hpi (220 μs). The complete infectious process of SFV on BHK-21 cells (**Section S3**) showed that 2 hpi is the time when SFV is completely uncoating. The latent period during the growth of SFV was 3 h. However, the traditional method based on RNA or protein techniques cannot detect the potential crisis, as viral replication and other activities can evade detection of immune responses from host cells, while relaxometry is sensitive to relatively early processes of radical formation. **Figure 5b** also shows the lowest T_1 values (highest radical load) at 6 hpi (91 μs). This is also the timing when the viral load is greatest as described by Kaariainen et al.[47]. According to Akaike's work[7], viral replication directly leads to the production of iNOS (inducible NO* synthase), resulting in NO* (nitric oxide) overproduction. NO* is a gaseous nitrogen-centered radical is induced during viral infections. This radical is also a source of cellular oxidative stress (as described in **Figure S4C**). Our findings support the hypothesis that

RNA viruses may utilize oxidative stress induced during infection to help temporally control genome RNA capping and genome replication[48].

From 6 hpi to 10 hpi the radical load is decreasing. One possible reason is that the virus-producing rate decreases. The other reason is that the cells gradually lose their ability to produce radicals at a high viral load, and the radicals produced in 6 hpi gradually transformed into non-paramagnetic ROS. This is also proven by the DCFDA assay (to measure both paramagnetic and non-paramagnetic ROS) in **Section S5.** As shown in **Figure S7b-c,** DCFDA treated infectious BHK-21 cells at 10 hpi are brighter than at 5 hpi.

UV irradiation can damage the genome of the virus, which will inhibit viral replication. However, not only the viral replication but the viral components can also induce NO overproduction, this makes cells' response to UV-inactivated SFV-FND conjugates similar to infectious SFV-FND. A similar response is seen also in inactivated viral vaccines where cells also respond without the actual infection. As a comparison, the control group, where BHK-21 cells were incubated with SA-FND without infected by SFV, did not show any significant changes (**Figure 5b**). The same is true for bare FNDs which are not measuring at the location of virus entry. This indicates that the radical response to viruses is localized rather than throughout the entire cells.

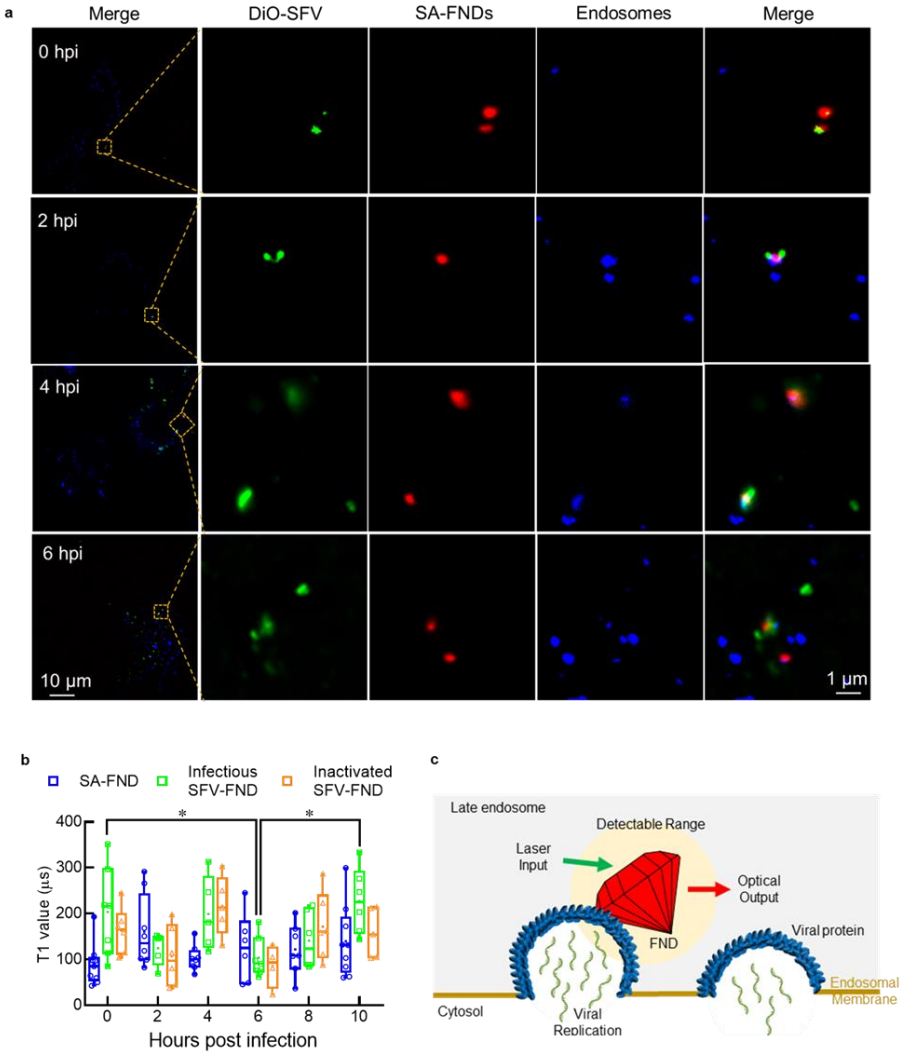

Figure 5. *(a) Representative fluorescent images of SFV-FND conjugates in BHK-21 cells at different incubation times. 0 hpi represents DiO-SFV-FND conjugates and BHK-21 cells were co-cultured at 4 ℃ for 1 h; 2, 4, and 6 hpi represent DiO-SFV-FND conjugates and BHK-21 cells co-cultured for 2, 4, and 6 hours at 37 ℃, 5% CO2, followed by fixing and staining. (b) T_1 measurements recorded every from 0 hpi to 10 hpi when cells were incubated with infectious SFV-FND and inactivated SFV-FND. Cells treated with SA-FND were set as negative control group. All the timepoints across all the groups have at least 8 independent measurements. (c) Representation of the location and events that diamond particles are detecting by using virus-diamond particles. * indicates statistical significance as determined by the one-way Anova test. A two-way Anova with post-hoc test (Sidak) indicates that infectious time is the only significant vibration factor (P= 0.0229, *).*

5.3.7 Investigating pseudo real-time variation in intracellular free radical amount post SFV infection

After probing the intracellular free radical composition in BHK-21 cells every two hours post SFV infection and the corresponding FND movement, we evaluated the "pseudo real-time" free radical response of host cells to the intruding virus. In "pseudo real-time" experiments, we apply the T_1 measurement cycle for 85,000 times in 85 min. Then we deployed the "moving window algorithm" to analyze the collected data to investigate the pseudo real-time evolution of the T_1 relaxation which is explained in **Figure 6a**. Instead of using output of all of the T_1 measurement cycles for quantifying the T_1 value, its small subset was used for quantifying the T_1. Therefore, this analytical method does not necessarily improve the temporal resolution in a conventional sense, but it does provide the evolution of T_1 as a function of time (**Figure 4a** and **Figure 5b**).

SFV-FND conjugates were used to investigate the radical response at the place of virus entry. The variation in T1 obtained from BHK-21 cells treated with infectious SFV-FND (green, **Figure 6b–c**) is significantly different from SA-FND treated cells (blue, **Figure 6b–c**). We observed a decrease of T_1 between 10 and 15 min (from 248 to 133 µs) and during 30-40 min (from 270 to 130 µs) when cells were treated with infectious SFV-FND. This decrease did not occur in the control group. Interestingly, these changes in radical load are occurring during the fusion and uncoating period in the early SFV infectious process (see pseudo real-time scale **Figure 6a**). Normally, the whole endocytosis process takes around 30 min to internalize all the prebound viral particles, and uptake of the half amount viral particles is around 10 min[38,49]. Membrane fusion and uncoating (with a mean time of 5 min) takes place immediately after endocytosis. According to Mark et. al.[49], the most fusion events of SFV take place during ~7-25 min, which indicates a higher possibility of observing a membrane fusion event should be during this period when individual virus particle is studied. The dropping period (10-15 min) is also consistent with the fusion time (around 800 seconds) for SFV-FND which we investigated in the entrance experiment described in **Section 4.3.3 (Figure 3e).** Moreover, stress granules (SG) formation occurs transiently after viral uncoating but before viral mRNA

transcription to shut the host protein synthesis off[50,51]. One of inducers of SG formation is oxidative stress[52]. As a result, the decreasing T_1 at 10-15 min can probably be attributed to the fusion event, while the decreasing T_1 at 30-40 min is probably due to the SG formation after fusion and uncoating. The variations were also shown in inactivated SFV-FND treated cells, but with less amplitude comparing the red and green curve in **Figure 6b-c**.

Viral membrane fusion and uncoating process are interesting process in the early-phase infections. Widely-used methods to detect this processes are electron microscopy[53,54] and fluorescent microscopy[31,36] based on self-quenching dyes (as shown in **Figure 3**). From our results we hypothesize a relation between radical response and viral membrane fusion and uncoating.

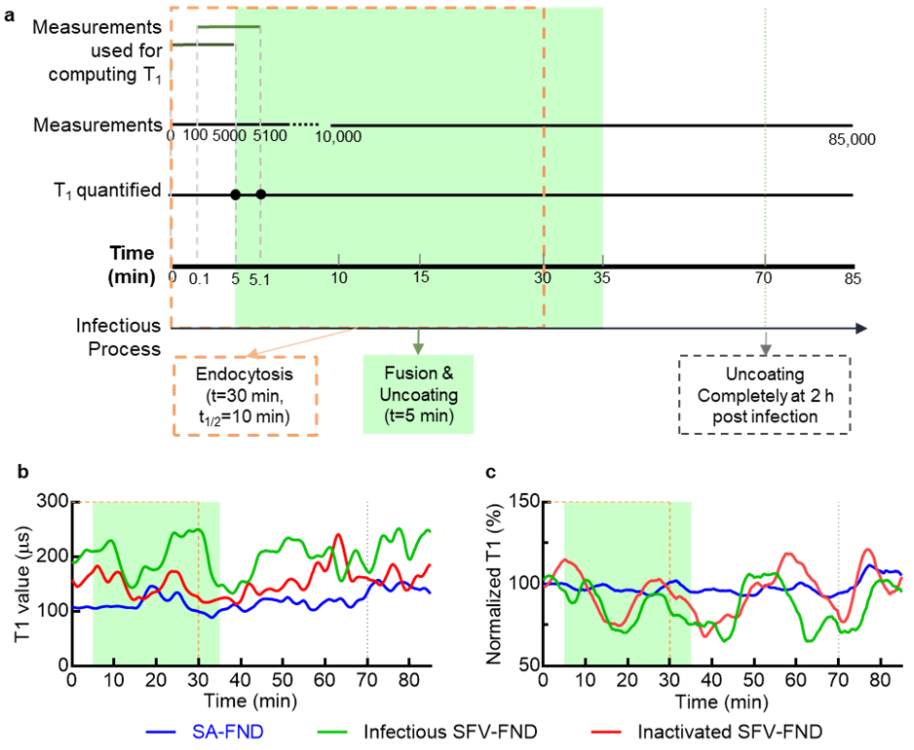

Figure 6. (a) Graphical representation of the 'moving window' algorithm used for analyzing the data to deduce pseudo real-time variation in the intracellular free radical concentration near viral particles. Time-dependent early viral infection process was superimposed to 'moving window' algorithm. The orange dash square represents the endocytosis process, and green square represents the fusion & uncoating process, respectively. Experimental results (b) and normalized T_1 results (c) obtained for cells treated with infectious SFV-FND, inactivated SFV-FND, and SA-FND (negative control). The data was shown as median of at least 8 independent measurements for each group. Two-way Anova with post-hoc test (Turkey) indicates the significant difference between infectious SFV-FND and SA-FND groups ($P<0.001$, *).

5.3.8 Influence of pH, temperature, viscosity and other factors on T1 relaxation

Last year, Fujisaku and co-workers demonstrated how the T_1 relaxation of 50-100 nm FND alters upon the change in its pH environment. In fact, the authors proposed a diamond relaxometry based pH-metry to measure pH changes in the range of 3 – 11. On the other hand, virus

infection has been shown to alter the intracellular[55,56] and extracellular[57] pH by up to a unit (from pH of ~7.4). Although, the necessity of low pH for SFV fusion is discussed in the literature[33,58], whether SFV infection actively modifies the intracellular pH is not yet clear. However, from our previous measurements of pH versus T_1 we conclude that T_1 was not influenced by pH significantly in the relevant pH range[59].

Similar to pH, temperature also affects the coherence time of the NV centers embedded in a diamond crystal. Moreover, the application of NV-based thermometer for the intracellular temperature sensing was also demonstrated[60]. In addition, molecular interaction, solvent, or solvent viscosity affect the NV coherence as well[61]. However, all these factors are unlikely to change drastically enough to cause a shift in T_1 inside a cell due to the viral infection. Hence, their effect on changes in T_1 observed during our measurements can be disregarded. Furthermore, it has been shown that ROS is often involved in the signaling pathway while cells cope with the photo illumination[62,63]. Therefore, cellular phototoxicity might also be a factor to be considered if pseudo real-time T_1 data is to be acquired over longer durations. In fact, as certain cell types are more susceptible to phototoxicity than others[64], cellular phototoxicity might still be a relevant factor even for a short T_1 measurements depending on the experimental design (cell type, laser power, etc). However, artifacts generated due to photo-induced free radical formation were safely dealt with simply by including a control sample (where only time was passed and no interventions were made).

5.4 Conclusions

Here we have demonstrated the utility of diamond relaxometry to study unprecedented details of the free radical response of host cells upon viral infection. Using SFV and BHK-21 as a model system, we probed the free radical response of the cells until 10 hpi. The general intracellular radical response was investigated by treating host cells with FND and SFV separately, and intracellular radical response near viral particles was investigated by virus-diamond conjugates (SFV-FND).

(i)When BHK-21 cells were treated with FND and SFV separately, we found that the free radical concentration in infected host cells is not

uniform across the cell volume and there are discrete pockets of relatively higher or lower free radical concentration. This indicates that signals detected by the intracellular FND is dependent on the location of the particle rather than the nature of the external stimulus. Moreover, we reveal the unique potential of this method to probe the systemic alterations in the cytoplasmic transport. Here, SFV infection was found to elevate the FND movement within the cytoplasm as quantified in terms of maximum particle displacement.(ii) By using SFV-FND, relaxometry is able to monitor the radical variation at the site of viral production during viral replication and even in the early infectious process. We observed alterations of T_1, which represent the intracellular free radical concentration near viral particles, is related to viral replication and other viral components. Immunostaining was used to confirm the locations where we conduct the T_1 measurements. Moreover, pseudo real-time technique based on diamond relaxometry and virus-diamond conjugates can used to detect the viral membrane fusion and uncoating events from cellular radical response. Obtaining such information with the conventional techniques is impossible.

Going forward, diamond relaxometry as an emerging technology used in biology, efforts need to be taken to (1) efficiently track the movement of the FND (2) implement sophisticated pulsing techniques such as double electron-electron resonance measurements for identifying specific free radical species and enhancing specificity and (3) reduce the FND-to-FND variation in its quantum sensing properties. Finally, we hope that this novel and powerful method will enable researchers to discover and/or redefine the fundamentals of the viral infection and thereby contribute to the design of strategies to combat them.

Acknowledgements

This work is financially supported by RS's European Research Commission grant (ERC STG-714289), a FOM projectruimte grant (G-36), and a grant from the De Cock-Hadders stichting (2022-30). Additionally, Viraj G Damle, Kaiqi Wu, and Aryan Morita are supported by Marie Curie Individual Fellowship (DLV-838494), CSC scholarship, and LPDP grant respectively. Part of the imaging from this work was performed at the UMCG Imaging and Microscopy Center (UMIC).

References

1. T. Oda, T. Akaike, T. Hamamoto, F. Suzuki, T. Hirano, H. Maeda, Oxygen Radicals in Influenza-Induced Pathogenesis and Treatment with Pyran Polymer-Conjugated Sod. *Science.* 1989, *244* (4907), 974-976. https://doi.org/10.1126/science.2543070.

2. T. Akaike, Role of Free Radicals in Viral Pathogenesis and Mutation. *Rev. Med. Virol.* 2001, *11* (2), 87-101. https://doi.org/10.1002/rmv.303.

3. T. Akaike, Y. Noguchi, S. Ijiri, K. Setoguchi, M. Suga, Y. M. Zheng, B. Dietzschold, H. Maeda, Pathogenesis of Influenza Virus-Induced Pneumonia: Involvement of Both Nitric Oxide and Oxygen Radicals. *Proc. Natl. Acad. Sci. U. S. A.* 1996, *93* (6), 2448-2453. https://doi.org/10.1073/pnas.93.6.2448.

4. T. Akaike, M. Ando, T. Oda, T. Doi, S. Ijiri, S. Araki, H. Maeda, Dependence on O2-Generation by Xanthine Oxidase of Pathogenesis of Influenza Virus Infection in Mice. *J. Clin. Invest.* 1990, *85* (3), 739-745. https://doi.org/10.1172/JCI114499.

5. T. Akaike, S. Fujii, A. Kato, J. Yoshitake, Y. Miyamoto, T. Sawa, S. Okamoto, M. Suga, M. Asakawa, Y. Nagai, Viral Mutation Accelerated by Nitric Oxide Production During Infection in Vivo. *FASEB J.* 2000, *14* (10), 1447-1454. https://doi.org/10.1096/fasebj.14.10.1447.

6. T. Akaike, M. Suga, H. Maeda, Free Radicals in Viral Pathogenesis: Molecular Mechanisms Involving Superoxide and No. *Exp. Biol. Med.* 1998, *217* (1), 64-73. https://doi.org/10.3181/00379727-217-44206.

7. T. Akaike, H. Maeda, Nitric Oxide and Virus Infection. *Immunology.* 2000, *101* (3), 300-308. https://doi.org/10.1046/j.1365-2567.2000.00142.x.

8. H. Maeda, T. Akaike, Oxygen Free Radicals as Pathogenic Molecules in Viral Diseases. *Proc. Soc. Exp. Biol. Med.* 1991, *198* (2), 721-727. https://doi.org/10.3181/00379727-198-43309C.

9. A. Phaniendra, D. B. Jestadi, L. Periyasamy, Free Radicals: Properties, Sources, Targets, and Their Implication in Various Diseases. *Indian J. Clin. Biochem.* 2015, *30* (1), 11-26. https://doi.org/10.1007/s12291-014-0446-0.

10. Kalyanaraman, V. Darley-Usmar, K. J. Davies, P. A. Dennery, H. J. Forman, M. B. Grisham, G. E. Mann, K. Moore, L. J. Roberts II, H. Ischiropoulos, Measuring Reactive Oxygen and Nitrogen Species with Fluorescent Probes: Challenges and Limitations. *Free Radic. Biol. Med.* 2012, *52* (1), 1-6. https://doi.org/10.1016/j.freeradbiomed.2011.09.030.

11. C. Winterbourn, The Challenges of Using Fluorescent Probes to Detect and Quantify Specific Reactive Oxygen Species in Living Cells. *Biochim. Biophys. Acta - Gen. Subj.* 2014, *1840* (2), 730-738. https://doi.org/10.1016/j.bbagen.2013.05.004.

12. K.-I. Lin, P. Pasinelli, R. H. Brown, J. M. Hardwick, R. R. Ratan, Decreased Intracellular Superoxide Levels Activate Sindbis Virus-Induced Apoptosis. *J. Biol. Chem.* 1999, *274* (19), 13650-13655. https://doi.org/10.1074/jbc.274.19.13650.

13. S. R. Hemelaar, B. Saspaanithy, S. R. L'Hommelet, F. P. Perona Martinez, K. J. Van der Laan, R. Schirhagl, The Response of Hela Cells to Fluorescent Nanodiamond Uptake. *Sensors.* 2018, *18* (2), 355. https://doi.org/10.3390/s18020355.

14. F. Jelezko, Ultrasensitive Diamond Magnetometers. *Physics.* 2014, *7*, 43. https://doi.org/10.1103/Physics.7.43.

15. J. M. Taylor, P. Cappellaro, L. Childress, L. Jiang, D. Budker, P. R. Hemmer, A. Yacoby, R. Walsworth, M. D. Lukin, High-Sensitivity

Diamond Magnetometer with Nanoscale Resolution. *Nat. Phys.* 2008, *4* (10), 810-816. https://doi.org/10.1038/nphys1075.

16. A. Gruber, A. Dräbenstedt, C. Tietz, L. Fleury, J. Wrachtrup, C. Von Borczyskowski, Scanning Confocal Optical Microscopy and Magnetic Resonance on Single Defect Centers. *Science.* 1997, *276* (5321), 2012-2014. https://doi.org/10.1126/science.276.5321.2012.

17. G. Balasubramanian, I. Chan, R. Kolesov, M. Al-Hmoud, J. Tisler, C. Shin, C. Kim, A. Wojcik, P. R. Hemmer, A. Krueger, Nanoscale Imaging Magnetometry with Diamond Spins under Ambient Conditions. *Nature.* 2008, *455* (7213), 648-651. https://doi.org/10.1038/nature07278.

18. Morita, A. C. Nusantara, F. P. P. Martinez, T. Hamoh, V. G. Damle, K. J. van der Laan, A. Sigaeva, T. Vedelaar, M. Chang, M. Chipaux, Quantum Monitoring the Metabolism of Individual Yeast Mutant Strain Cells When Aged, Stressed or Treated with Antioxidant. 2020, http://arxiv.org/abs/2007.16130.

19. L. Rondin, J. P. Tetienne, S. Rohart, A. Thiaville, T. Hingant, P. Spinicelli, J. F. Roch, V. Jacques, Stray-Field Imaging of Magnetic Vortices with a Single Diamond Spin. *Nat. Commun.* 2013, *4*, 5. https://doi.org/10.1038/ncomms3279.

20. J.-P. Tetienne, T. Hingant, L. Rondin, A. Cavaillès, L. Mayer, G. Dantelle, T. Gacoin, J. Wrachtrup, J.-F. Roch, V. Jacques, Spin Relaxometry of Single Nitrogen-Vacancy Defects in Diamond Nanocrystals for Magnetic Noise Sensing. *Phys. Rev. B.* 2013, *87* (23), 235436. https://doi.org/10.1103/PhysRevB.87.235436.

21. F. Perona Martínez, A. C. Nusantara, M. Chipaux, S. K. Padamati, R. Schirhagl, Nanodiamond Relaxometry-Based Detection of Free-Radical Species When Produced in Chemical Reactions in Biologically Relevant Conditions. *ACS Sensors.* 2020, *5* (12), 3862-3869. https://doi.org/10.1021/acssensors.0c01037.

22. J. A. Rioux, I. R. Levesque, B. K. Rutt, Biexponential Longitudinal Relaxation in White Matter: Characterization and Impact on T1 Mapping with Ir-Fse and Mp2rage. *Magn. Reson. Med.* 2016, *75* (6), 2265-2277. https://doi.org/10.1002/mrm.25729.

23. R. Bron, J. M. Wahlberg, H. Garoff, J. Wilschut, Membrane Fusion of Semliki Forest Virus in a Model System: Correlation between Fusion Kinetics and Structural Changes in the Envelope Glycoprotein. *Embo J.* 1993, *12* (2), 693-701. https://doi.org/10.1002/j.1460-2075.1993.tb05703.x.

24. G. J. Atkins, B. J. Sheahan, P. Liljeström, The Molecular Pathogenesis of Semliki Forest Virus: A Model Virus Made Useful? *J. Gen. Virol.* 1999, *80* (9), 2287-2297. https://doi.org/10.1099/0022-1317-80-9-2287.

25. S.-L. Liu, Z.-L. Zhang, E.-Z. Sun, J. Peng, M. Xie, Z.-Q. Tian, Y. Lin, D.-W. Pang, Visualizing the Endocytic and Exocytic Processes of Wheat Germ Agglutinin by Quantum Dot-Based Single-Particle Tracking. *Biomaterials.* 2011, *32* (30), 7616-7624. https://doi.org/10.1016/j.biomaterials.2011.06.046.

26. S. L. Liu, Z. L. Zhang, Z. Q. Tian, H. S. Zhao, H. B. Liu, E. Z. Sun, G. F. Xiao, W. P. Zhang, H. Z. Wang, D. W. Pang, Effectively and Efficiently Dissecting the Infection of Influenza Virus by Quantum-Dot-Based Single-Particle Tracking. *ACS Nano.* 2012, *6* (1), 141-150. https://doi.org/10.1021/nn2031353.

27. F. X. Zhang, Z. H. Zheng, S. L. Liu, W. Lu, Z. F. Zhang, C. L. Zhang, P. Zhou, Y. Zhang, G. Long, Z. K. He, D. W. Pang, Q. X. Hu, H. Z. Wang, Self-Biotinylation and Site-Specific Double Labeling of Baculovirus Using Quantum Dots for Single-Virus in-Situ Tracking. *Biomaterials.* 2013, *34* (30), 7506-7518. https://doi.org/10.1016/j.biomaterials.2013.06.030.

28. M. S. Chan, R. Landig, J. Choi, H. Y. Zhou, X. Liao, M. D. Lukin, H. Park, P. K. Lo, Stepwise Ligand-Induced Self-Assembly for Facile Fabrication of Nanodiamond-Gold Nanoparticle Dimers Via Noncovalent Biotin-

Streptavidin Interactions. *Nano Lett.* 2019, *19* (3), 2020-2026. https://doi.org/10.1021/acs.nanolett.9b00113.

29. J. Hierholzer, R. Killington, Virus Isolation and Quantitation. In *Virology Methods Manual*, 1996; pp 25-46 https://doi.org/10.1016/b978-012465330-6/50003-8.

30. N. V. Ayala-Nuñez, J. Wilschut, J. M. Smit, Monitoring Virus Entry into Living Cells Using Did-Labeled Dengue Virus Particles. *Methods.* 2011, *55* (2), 137-143. https://doi.org/10.1016/j.ymeth.2011.07.009.

31. H. M. van der Schaar, M. J. Rust, B.-L. Waarts, H. van der Ende-Metselaar, R. J. Kuhn, J. Wilschut, X. Zhuang, J. M. Smit, Characterization of the Early Events in Dengue Virus Cell Entry by Biochemical Assays and Single-Virus Tracking. *J. Virol.* 2007, *81* (21), 12019-12028. https://doi.org/10.1128/jvi.00300-07.

32. J. M. Smit. Mutational Analysis of Receptor Interaction and Membrane Fusion Activity of Sindbis Virus. 2002. https://research.rug.nl/en/publications/mutational-analysis-of-receptor-interaction-and-membrane-fusion-a%20.

33. A. Helenius, J. Kartenbeck, K. Simons, E. Fries, On the Entry of Semliki Forest Virus into Bhk-21 Cells. *J. Cell Biol.* 1980, *84* (2), 404-420. https://doi.org/10.1083/jcb.84.2.404.

34. B. M. Dundas, D. Demonte, S. Park, Streptavidin–Biotin Technology: Improvements and Innovations in Chemical and Biological Applications. *Appl. Microbiol. Biotechnol.* 2013, *97* (21), 9343-9353. https://doi.org/10.1007/s00253-013-5232-z.

35. J. Barton, M. Gulka, J. Tarabek, Y. Mindarava, Z. Y. Wang, J. Schimer, H. Raabova, J. Bednar, M. B. Plenio, F. Jelezko, M. Nesladek, P. Cigler, Nanoscale Dynamic Readout of a Chemical Redox Process Using Radicals Coupled with Nitrogen-Vacancy Centers in Nanodiamonds. *Acs*

Nano. 2020, *14* (10), 12938-12950. https://doi.org/10.1021/acsnano.0c04010.

36. T. E. Hoornweg, M. K. van Duijl-Richter, N. V. Ayala Nuñez, I. C. Albulescu, M. J. van Hemert, J. M. Smit, Dynamics of Chikungunya Virus Cell Entry Unraveled by Single-Virus Tracking in Living Cells. *J. Virol.* 2016, *90* (9), 4745-4756. https://doi.org/10.1128/JVI.03184-15.

37. A. Helenius, M. Marsh, J. White, Inhibition of Semliki Forest Virus Penetration by Lysosomotropic Weak Bases. *J. Gen. Virol.* 1982, *58* (JAN), 47-61. https://doi.org/10.1099/0022-1317-58-1-47.

38. K. U. Dee, D. A. Hammer, M. L. Shuler, A Model of the Binding, Entry, Uncoating, and Rna-Synthesis of Semliki-Forest-Virus in Baby Hamster-Kidney (Bhk-21) Cells. *Biotechnol. Bioeng.* 1995, *46* (5), 485-496. https://doi.org/10.1002/bit.260460513.

39. Holcman, Modeling DNA and Virus Trafficking in the Cell Cytoplasm. *J. Stat. Phys.* 2007, *127* (3), 471-494. https://doi.org/10.1007/s10955-007-9282-4.

40. S. Cohen, S. Au, N. Pante, How Viruses Access the Nucleus. *Biochim. Biophys. Acta - Mol. Cell Res.* 2011, *1813* (9), 1634-1645. https://doi.org/10.1016/j.bbamcr.2010.12.009.

41. G. Seisenberger, M. U. Ried, T. Endreß, H. Büning, M. Hallek, C. Bräuchle, Real-Time Single-Molecule Imaging of the Infection Pathway of an Adeno-Associated Virus. *Science.* 2001, *294* (5548), 1929-1932. https://doi.org/10.1126/science.1064103.

42. S. M. Lyi, M. J. A. Tan, C. R. Parrish, Parvovirus Particles and Movement in the Cellular Cytoplasm and Effects of the Cytoskeleton. *Virology.* 2014, *456*, 342-352. https://doi.org/10.1016/j.virol.2014.04.003.

43. A. M. Mastro, M. A. Babich, W. D. Taylor, A. D. Keith, Diffusion of a Small Molecule in the Cytoplasm of Mammalian-Cells. *Proc. Natl. Acad.*

Sci. U. S. A. 1984, *81* (11), 3414-3418. https://doi.org/10.1073/pnas.81.11.3414.

44. R. G. Sadovsky, S. Brielle, D. Kaganovich, J. L. England, Measurement of Rapid Protein Diffusion in the Cytoplasm by Photo-Converted Intensity Profile Expansion. *Cell Rep.* 2017, *18* (11), 2795-2806. https://doi.org/10.1016/j.celrep.2017.02.063.

45. T. Kuhn, T. O. Ihalainen, J. Hyvaluoma, N. Dross, S. F. Willman, J. Langowski, M. Vihinen-Ranta, J. Timonen, Protein Diffusion in Mammalian Cell Cytoplasm. *PLoS One.* 2011, *6* (8), https://doi.org/10.1371/journal.pone.0022962.

46. K. J. Ertel, D. Benefield, D. Castano-Diez, J. G. Pennington, M. Horswill, J. A. den Boon, M. S. Otegui, P. Ahlquist, Cryo-Electron Tomography Reveals Novel Features of a Viral Rna Replication Compartment. *eLife.* 2017, *6*, https://doi.org/10.7554/eLife.25940.

47. L. Kaariainen, P. J. Gomatos, A Kinetic Analysis of Synthesis in Bhk 21 Cells of Rnas Specific for Semliki Forest Virus. *J. Gen. Virol.* 1969, *5*, 251-265. https://doi.org/10.1099/0022-1317-5-2-251.

48. R. C. Gullberg, J. J. Steel, S. L. Moon, E. Soltani, B. J. Geiss, Oxidative Stress Influences Positive Strand Rna Virus Genome Synthesis and Capping. *Virology.* 2015, *475*, 219-229. https://doi.org/10.1016/j.virol.2014.10.037.

49. M. Marsh, E. Bolzau, A. Helenius, Penetration of Semliki Forest Virus from Acidic Prelysosomal Vacuoles. *Cell.* 1983, *32* (3), 931-940. https://doi.org/10.1016/0092-8674(83)90078-8.

50. M. D. Panas, N. Kedersha, G. M. McInerney, Methods for the Characterization of Stress Granules in Virus Infected Cells. *Methods.* 2015, *90*, 57-64. https://doi.org/10.1016/j.ymeth.2015.04.009.

51. Valiente-Echeverria, L. Melnychuk, A. J. Mouland, Viral Modulation of Stress Granules. *Virus Res.* 2012, *169* (2), 430-437. https://doi.org/10.1016/j.virusres.2012.06.004.

52. L. H. Chen, B. D. Liu, Relationships between Stress Granules, Oxidative Stress, and Neurodegenerative Diseases. *Oxid. Med. Cell. Longev.* 2017, *2017*, https://doi.org/10.1155/2017/1809592.

53. S. Halldorsson, S. Li, M. Q. Li, K. Harlos, T. A. Bowden, J. T. Huiskonen, Shielding and Activation of a Viral Membrane Fusion Protein. *Nat. Commun.* 2018, *9*, https://doi.org/10.1038/s41467-017-02789-2.

54. N. H. Acheson, I. Tamm, Replication of Semliki Forest Virus - an Electron Microscopic Study. *Virology.* 1967, *32* (1), 128-&. https://doi.org/10.1016/0042-6822(67)90261-9.

55. A. Helenius, Virus Entry: What Has Ph Got to Do with It? *Nat. Cell Biol.* 2013, *15* (2), 125-125. https://doi.org/10.1038/ncb2678.

56. L. L. Moore, D. A. Bostick, R. F. Garry, Sindbis Virus Infection Decreases Intracellular Ph: Alkaline Medium Inhibits Processing of Sindbis Virus Polyproteins. *Virology.* 1988, *166* (1), 1-9. https://doi.org/10.1016/0042-6822(88)90139-0.

57. H. J. Liu, H. Maruyama, T. Masuda, A. Honda, F. Arai, The Influence of Virus Infection on the Extracellular Ph of the Host Cell Detected on Cell Membrane. *Front. Microbiol.* 2016, *7*, 8. https://doi.org/10.3389/fmicb.2016.01127.

58. S. Glomb-Reinmund, M. Kielian, The Role of Low Ph and Disulfide Shuffling in the Entry and Fusion of Semliki Forest Virus and Sindbis Virus. *Virology.* 1998, *248* (2), 372-381. https://doi.org/10.1006/viro.1998.9275.

59. L. Nie, A. C. Nusantara, V. G. Damle, R. Sharmin, E. P. P. Evans, S. R. Hemelaar, K. J. van der Laan, R. Li, F. P. Perona Martinez, T. Vedelaar,

M. Chipaux, R. Schirhagl, Quantum Monitoring of Cellular Metabolic Activities in Single Mitochondria. *Adv. Sci.* 2021, *7* (21), eabf0573. https://doi.org/10.1126/sciadv.abf0573.

60. Kucsko, P. C. Maurer, N. Y. Yao, M. Kubo, H. J. Noh, P. K. Lo, H. Park, M. D. Lukin, Nanometre-Scale Thermometry in a Living Cell. *Nature.* 2013, *500* (7460), 54-U71. https://doi.org/10.1038/nature12373.

61. T. Sekiguchi, S. Sotoma, Y. Harada, Fluorescent Nanodiamonds as a Robust Temperature Sensor inside a Single Cell. *Biophys. Physicobiol.* 2018, *15*, 229-234. https://doi.org/10.2142/biophysico.15.0_229.

62. V. Marek, S. Melik-Parsadaniantz, T. Villette, F. Montoya, C. Baudouin, F. Brignole-Baudouin, A. Denoyer, Blue Light Phototoxicity toward Human Corneal and Conjunctival Epithelial Cells in Basal and Hyperosmolar Conditions. *Free Radic. Biol. Med.* 2018, *126*, 27-40. https://doi.org/10.1016/j.freeradbiomed.2018.07.012.

63. I. Khan, E. Tang, P. Arany, Molecular Pathway of near-Infrared Laser Phototoxicity Involves Atf-4 Orchestrated Er Stress. *Sci. Rep.* 2015, *5*, 14. https://doi.org/10.1038/srep10581.

64. S. Waldchen, J. Lehmann, T. Klein, S. van de Linde, M. Sauer, Light-Induced Cell Damage in Live-Cell Super-Resolution Microscopy. *Sci. Rep.* 2015, *5*, 12. https://doi.org/10.1038/srep15348.

Supporting Information

S1. Characterization of the DiO-labeled SFV

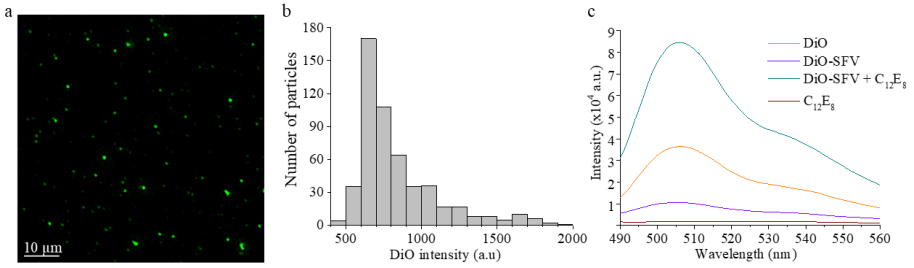

Figure S1. Characterization of DiO-labeled SFV. (a) Representative images showing DiO-labeled SFV particles. (b) The intensity of DiO-labeled SFV was determined with fluorescence microscopy. Particles with low fluorescence intensity (<1000 A.U.) were selected for viral fusion experiments and subsequent image analysis. (c) Fluorescence emission spectra of DiO-labeled SFV. DiO-labeled SFV was mixed with/without $C_{12}E_8$ in HNE buffer. Samples only containing $C_{12}E_8$ or DiO were set as negative or positive control groups, respectively. Emission scans were recorded at wavelengths 490 to 560 nm with excitation at 480 nm.

DiO, a self-quenched dye, was used to investigate the early infection process, including the membrane fusion properties. First, SFV were labeled with a relatively high surface density of the fluorescent probe DiO in the viral membrane. This way, its fluorescence was largely quenched but still allowed single virus particles to be clearly detected (**Figure S1a, b**). Membrane fusion of virus particles labeled were observed as fluorescence dequenching due to the dilution of the DiO probe into the target membrane. A significant increase in DiO fluorescent intensity was observed when the viral membrane was dissolved by the addition of $C_{12}E_8$ detergent (a nonionic detergent) with respect to the dequenching of DiO (**Figure S1c**).

S2. Increase in fluorescence intensity of the DiO upon viral fusion as observed with fluorescence microscope

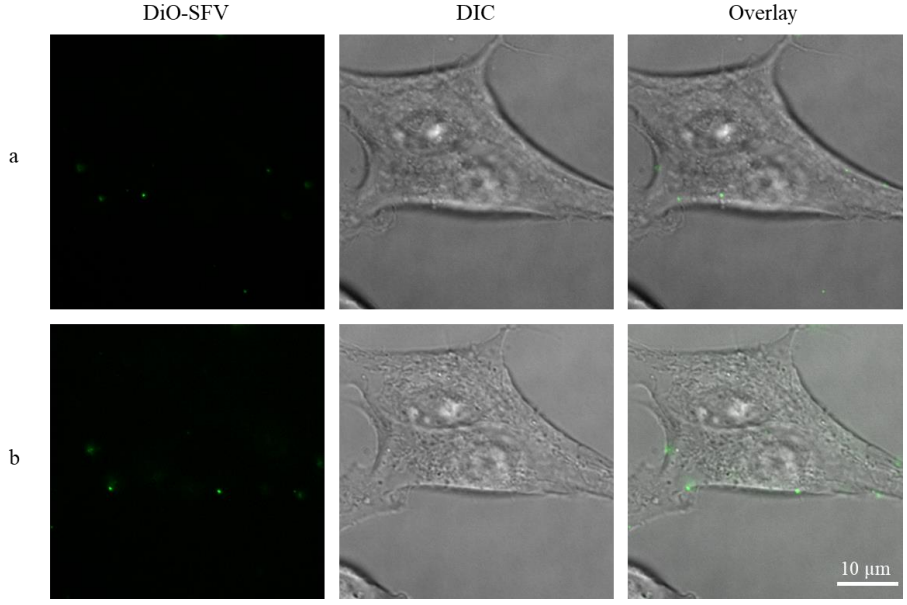

Figure S2. Viral fusion assay of DiO-SFV. Snapshots of BHK-21 cells recorded (a) after 45 minutes infection at 4°C and (b) after another 30 minutes infection by DiO-SFV at 37°C. Increase in fluorescence intensity is clearly visible after 30 minutes of incubation at the elevated temperature. The DiO signal was recorded in the FITC channel of fluorescent microscope (DeltaVision Elite). Cellular morphology was also recoded before and after viral fusion to access cellular health. The scale bar indicates 10 µm.

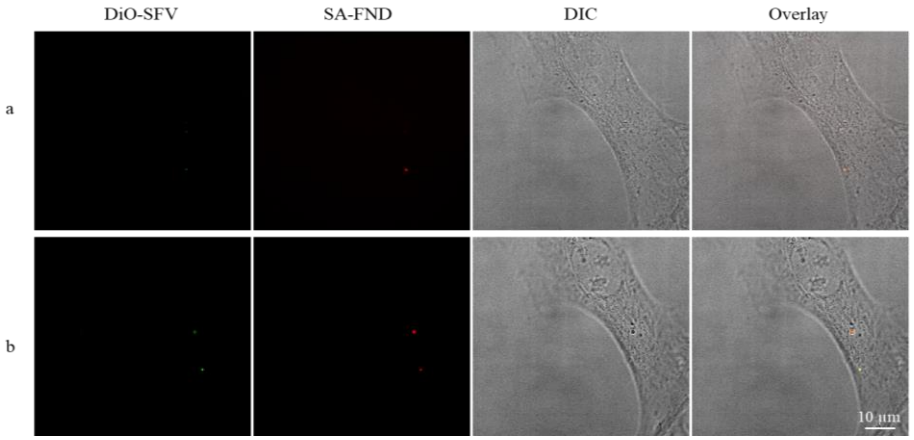

Figure S3. Viral fusion assay of DiO-SFV-FND. Snapshots of BHK-21 cells recorded (a) after 45 minutes at 4°C and (b) after another 30 minutes of infection by DiO-SFV-FND at 37°C. An increase in fluorescence intensity is clearly visible after 30 minutes of incubation at the elevated temperature. Signals for DiO and SA-FND were recorded in the FITC and A594 channels of a fluorescent microscope (DeltaVision Elite). Cellular morphology was also recoded before and after viral fusion to access cellular health. The scale bar indicates 10 µm.

Videos are available online which highlight the variation in DiO fluorescence intensity when cells were treated with DiO-SFV/DiO-SFV-FND, first with NH_4Cl followed by DiO-SFV/DiO-SFV-FND, and DiO-SFV/DiO-SFV-FND without cells.

(https://www.sciencedirect.com/science/article/pii/S2213231722000519)

S3. Summarized process of BHK-21 infected by SFV and mechanisms of cellular oxidative stress in virus infection

The SFV-BHK-21 infectious system is a well-studied model in virology. The whole infection process includes both a latent period and a viral replication process. The latent period consists of viral particles binding on the cell membrane, entering into cells by endocytosis, membrane fusion and uncoating, and releasing of genetic materials into the cytoplasm. Within 2 h post infections viruses are completely uncoated. Virus concentrations increase exponentially from 3.5-4 h post infections, and the greatest yields were reached between 6 and 7 h post infections (**Figure S4a, b**). **Figure S4c** shows how virus infection induces cellular oxidative stress. Specifically, viral replication and other viral components directly lead to the production of iNOS (inducible NO* synthase), resulting in NO* overproduction, which is the source of infected cellular oxidative stress.

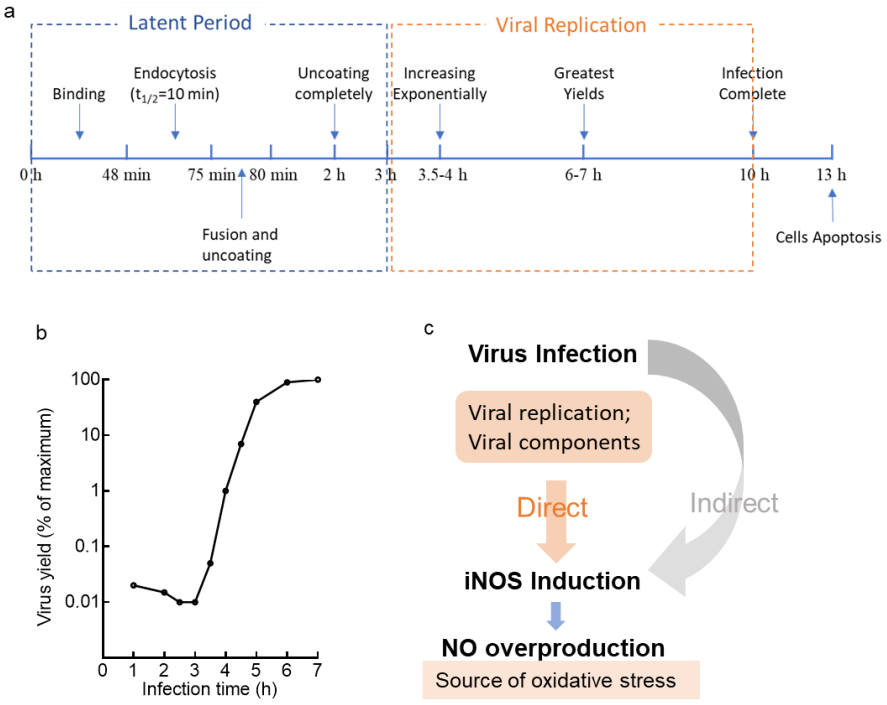

Figure S4. (a) Summarized timescales for BHK-21 infection by SFV. (b) Growth curve of SFV in BHK-21 cells infected at a MOI=20. (c) Mechanisms of cellular oxidative stress in virus infection.

S4. Principle of relaxometry relevant to the intracellular free radical sensing upon viral infection

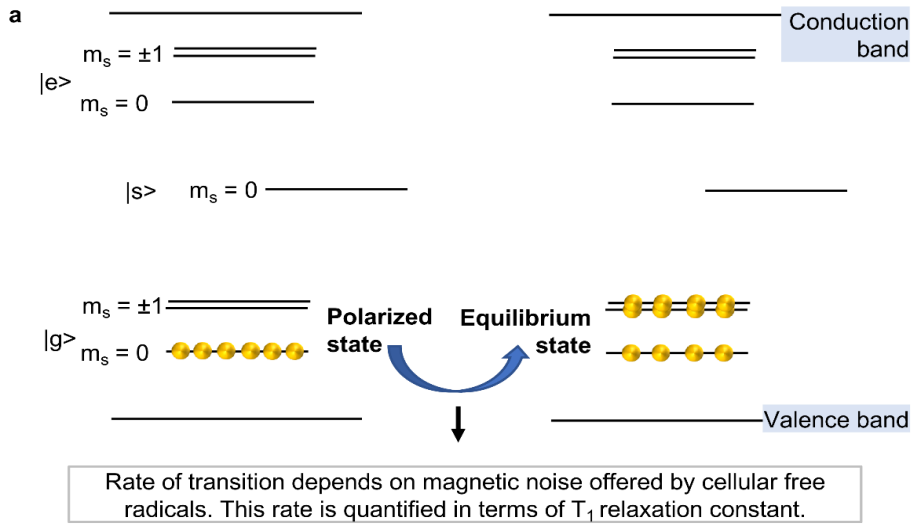

Figure S5. Photophysics of relaxometry.

Basic photophysics of relaxometry that is relevant for this work is explained using **Figure S5**. NV defects embedded in FNDs can be pumped into the optically brightest polarized state under a continuous laser illumination where most of the electrons are populated in the $|g\ m_s = 0$ energy state. Once the laser is turned off, the optically brightest polarized state of the NV center is lost and electrons transition back to their original equilibrium states $|g\ m_s = 0$ and $m_s = \pm 1$. The time required for the transition from the polarized state to the initial unpolarized equilibrium state is dependent on the magnetic noise around the NV defect. As unpaired free electrons of intracellular free radicals offer magnetic noise, they alter this transition time. In particular, the higher the free radical concentration around the NV center, the higher is the magnetic noise hence shorter is the transition time and vice versa. As a result, the transition time is a direct measure for the amount of cellular free radicals in the vicinity of the NV center. We quantify the transition time between polarized and equilibrium state via measuring spin-lattice or T_1 relaxation.

S5. Fluorescence assay-based evaluation of SFV infection induced oxidative stress in BHK-21 cells

S5.1. Experimental method

Oxidative stress in BHK-21 cells at different timepoints (0, 5, and 10 hpi) in the SFV infection cycle was probed using the DCFDA fluorescence assay (Thermofisher, Netherlands). The experimental groups used in this experiment at different timepoints are shown in **Figure S6**a and **Figure S6b** indicates the timeline of the experiment. In short, 40,000 BHK-21 cells were plated in 35 mm glass bottom petri dishes (Greiner bio-one, Germany) one day before the experiment. Approximately seven hours post seeding, we incubated the cells with 1 µg/ml 70 nm FND suspension. After overnight incubation, the FND suspension was replaced either with 500 µl fresh medium or with 100 µl of 2% infection medium. For the infection groups, 10% RPMI medium was added over the cells one hour post infection. At different timepoints, cells were first washed with the washing solution (2% FBS in PBS) three times and then incubated with 100 µl of 10 µg/mL DCFDA for one hour. The positive control group was subsequently treated with 0.01% H_2O_2 (in washing solution). The positive control group was treated with DCFDA one hour prior to the rest of the groups so that all the groups can be imaged at the same time. We note that, cells were maintained in the incubator at all times. At the end, cells were washed and imaged using a laser scanning confocal microscope (Zeiss LSM780, Germany) at the excitation wavelength of 488 nm. The same image acquisition settings (Gain 700 and laser power 2.1) were applied while imaging different groups at different timepoints. At every timepoint, at least four images of every group were recorded. This entire experiment was repeated two independent times to collect eight images per group per timepoint.

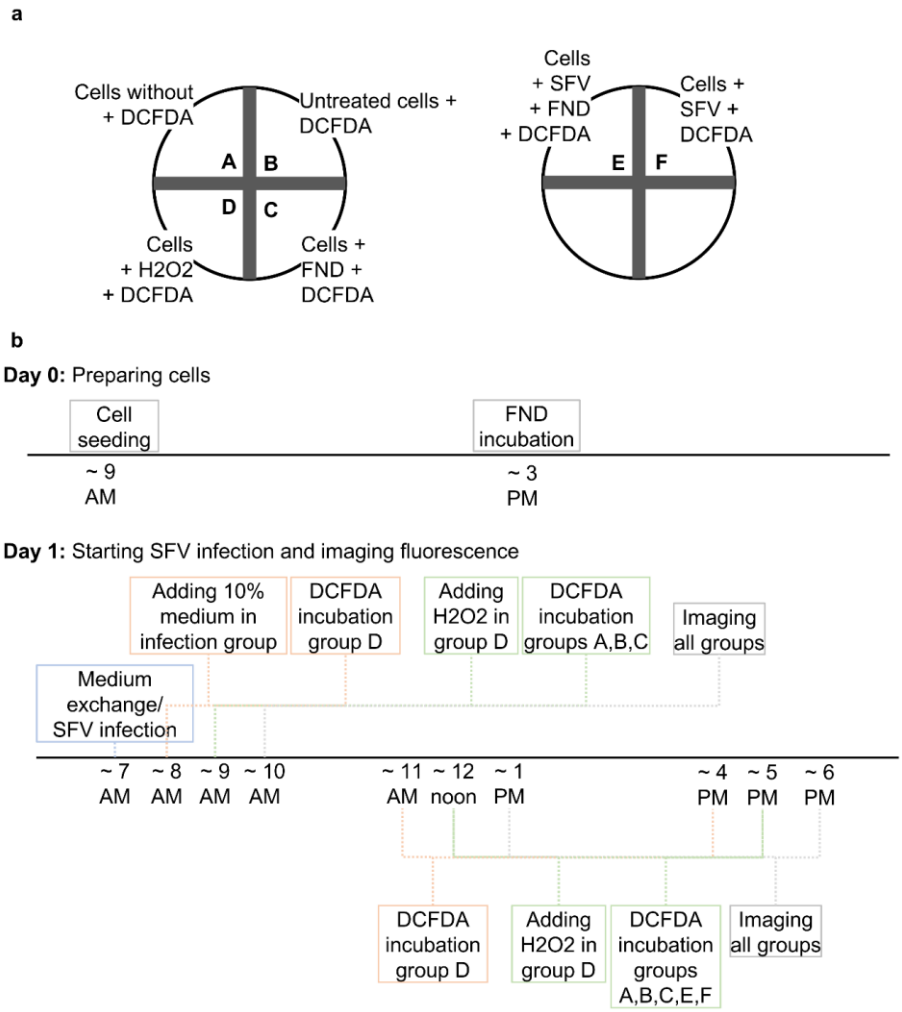

Figure S6. (a) Different groups used and (b) the timeline followed during the DCFDA ROS assay.

S5.2. Result and discussion

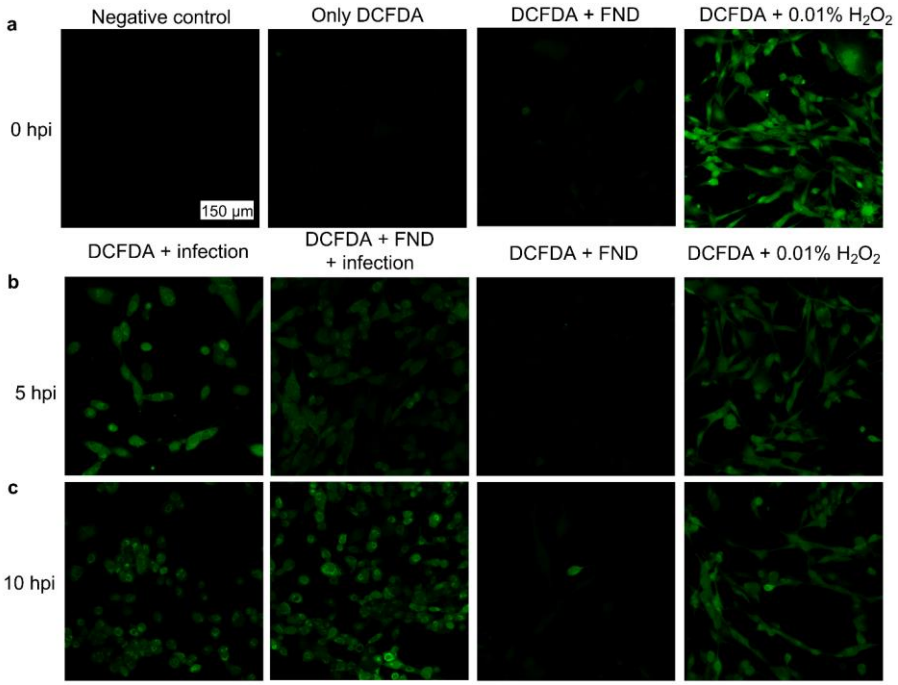

Figure S7. Results of fluorescence-based oxidative stress assay. Examples of images collected at (a) 0 hpi, (b) 5 hpi and (c) 10 hpi.

In this assay, non-fluorescent DCFDA molecules are converted into fluorescent molecules after reacting with ROS. Hence the amount of fluorescence is directly correlated with the amount of intracellular ROS. This assay measures the total amount of ROS produced within the cell during the incubation period whereas relaxometry specifically measures only the amount of free radicals at a given time. Although these two assays measure different entities, we performed the DCFDA assay to investigate the redox imbalance of the cells upon infection. We performed the DCFDA assay at 0, 5 and 10 hpi. At 0 hpi, untreated cells and cells having internalized FNDs did not show any fluorescence. This indicates that BHK-21 cells don't trigger any ROS response upon internalizing FNDs.

Contrary to these two groups, almost all the cells in the positive control group, which were treated with 0.01% H_2O_2 showed bright fluorescence highlighting the oxidative stress caused by the H_2O_2. Results obtained for cells with internalized FNDs and positive control group at 5 and 10 hpi are very comparable to those corresponding groups at 0 hpi. However, the infected cells with and without FNDs show bright fluorescence at both 5 and 10 hpi, which is similar to the positive control. This indicates high degree of oxidative stress caused by the SFV infection.

S6. Determining the optimal concentration of paraquat and N-acetylcysteine

S6.1. Experimental methods

The optimal concentration of paraquat and N-acetylcysteine for experiments elaborated in **Section S6** was determined by analyzing the metabolic activity level of cells using an MTT assay. In the literature, Lin and coworkers reported that 250 µM paraquat induced intracellular superoxide production in the cells[65] whereas 0.1-80 mM N-acetylcysteine (NAC) was used for blocking oxidant production[66]. Using these concentrations as a reference, we explored a range of concentrations of these chemicals. Specifically, concentration of 50 µM, 100 µM, 250 µM, 500 µM, 750 µM, 1 mM, 2 mM, 5 mM, 7,5 mM, and 10 mM of paraquat were used. For N-acetylcysteine, we investigated the following concentrations- 0.1 mM, 0.5 mM, 1 mM, 2.5 mM, 5 mM, 10 mM, 25 mM, 50 mM and 75 mM. For every concentration we tested the metabolic activity of cells using an MTT assay.

For the MTT assay, 20,000 cells were plated in flat bottom 96-well plates followed by 24h of incubation at 37°C and 5% CO_2. Then, the medium over cells was carefully removed and cells were washed with sterile PBS. Next, serum free cell media (RPMI media) were added into well plates followed by adding 5 mg/ml of MTT solution in sterile PBS. Cells were incubated with MTT solution for two hours at 37°C. After incubation, the liquid over cells from every well was collected and 2-propanol was added to dissolve the formazan. The plate was placed on a shaker for ~10-15 minutes. Photoabsorbance was read at 560 nm using a plate reader (Fluostar Optima).

S6.2. Results and discussion

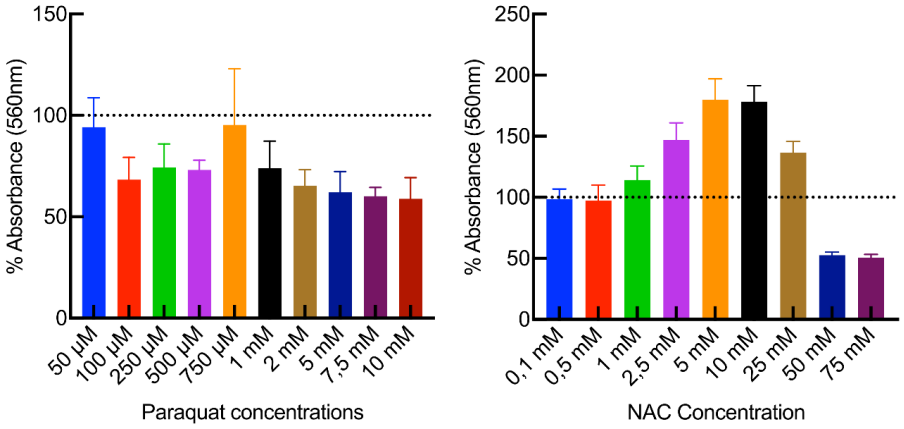

Figure S8. Absorbance was measured which is directly correlated with the cellular metabolic activity, when cells were treated with different Paraquat and NAC concentrations.

The amount of absorbance is directly coupled with the amount of formazan and hence with the metabolic activity of the cells. The concentration of Paraquat and NAC for which the metabolic activity of cells is altered the most compared to the control is determined to be optimal. This is in accordance with the rationale of the next experiment which is to assess the maximum change in the free radical composition under extreme conditions.

S7. Free radical response of BHK-21 cells to oxidative/anti-oxidative stress by chemical treatments

S7.1. Experimental methods

Here, we detected hydroxyl, superoxide and nitric oxide radicals using a commercially available fluorescent probes in three separate assays. Although these three assays were different from each other they had four basic steps- 1. Seeding 20,000 cells/well in a flat bottom 96-well plates (Corning Costar) followed by 24h of incubation at 37°C with 5% CO_2. 2. Removing the old medium carefully and incubating cells with fluorescent probe suspension for one hour 3. Introducing cells to (i) 100 µM paraquat (ii) 5 mM N-acetylcysteine and (iii) 0.01% H_2O_2 for one hour incubation. (iv) Untreated cells and (v) cells incubated overnight with FNDs were also used as controls. 4. Washing cells with a buffer followed by measuring fluorescence intensity using a plate reader operating in bottom mode.

S7.1.1 Hydroxyl radical assay

A hydroxyl radical detection assay was conducted using a mitochondrial hydroxyl radical detection assay kit (Abcam, Netherlands). In the last step, cells were washed with warm sterile PBS and 100 µl assay buffer was added per well. Fluorescence intensity was recorded at 540(excitation)/590(emission) nm.

S7.1.2 Superoxide assay

This assay was performed using a superoxide detection assay (cell based) kit (Abcam, Netherland). 0.5 mM suspension of the probe was prepared using phenol red free RPMI media. Then the suspension was removed and cells were washed with washing buffer followed by adding 100 µl PBS buffer. Fluorescent intensity was measured at 495(excitation)/525(emission) nm.

S7.1.3 Nitric oxide assay

DAF-FM Diacetate (4-Amino-5-Methylamino-2',7'-Difluorofluorescein Diacetate) (Thermofisher, Netherland) was used for detecting nitric oxide formation. 5 µM probe in phenol red free RPMI medium was prepared. In step four, cells were washed with sterile PBS to

remove excess medium. Then we replaced it with fresh phenol red free RPMI followed by 30 minutes incubation to allow complete de-esterification. Fluorescent intensity was measured at 495(excitation)/515(emission) nm.

S7.2. Results and discussion

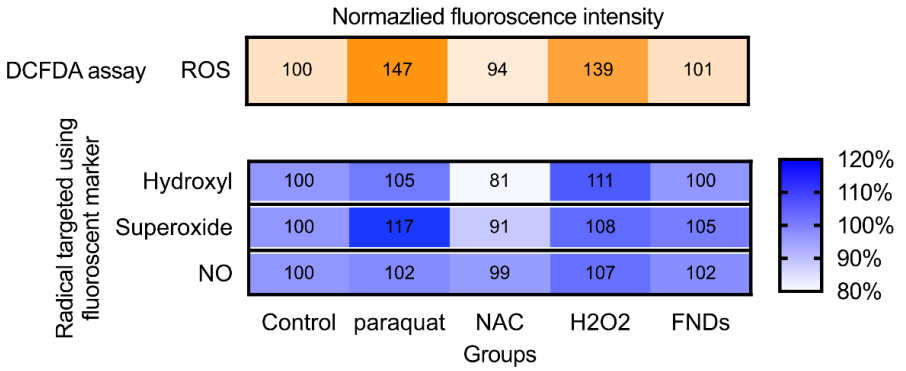

Figure S9. Heat map showing normalized fluorescence of DCFDA and free radical specific fluorescent markers quantified using a plate reader for different groups.

We gauged the maximum extent of the extra free radical production/nullification within BHK-21 cells upon introducing it to an extreme oxidative stress causing a external chemical stimuli or an anti-oxidant. Results shown in **Figure S9** indicate that, FNDs do not trigger a significant free radical production upon exposure to the chemicals. As expected, the superoxide-specific fluorescence probe intensity was maximal when the cells were treated with Paraquat. For the NAC treated cells, the fluorescence intensity was lower for all the free radical species. However, in none of the groups, the fluorescence intensity was higher or lower than 20% compared to the controls, suggesting that intracellular free radical amount do not dramatically fluctuate even after extreme oxidant/anti-oxidant chemical exposure. Interestingly, H_2O_2 which induces significant oxidative stress in cells does not seem to induce high concentration of free radicals. This indicates that the majority of the non-radical entities produced by a cell causing the oxidative stress in response

to the H_2O_2 compared to non-paramagnetic species which do not yield any change in the T_1 signal.

S8. Schematic representation of the experimental scheme to investigate pseudo real-time variation in intracellular free radical amount post SFV infection

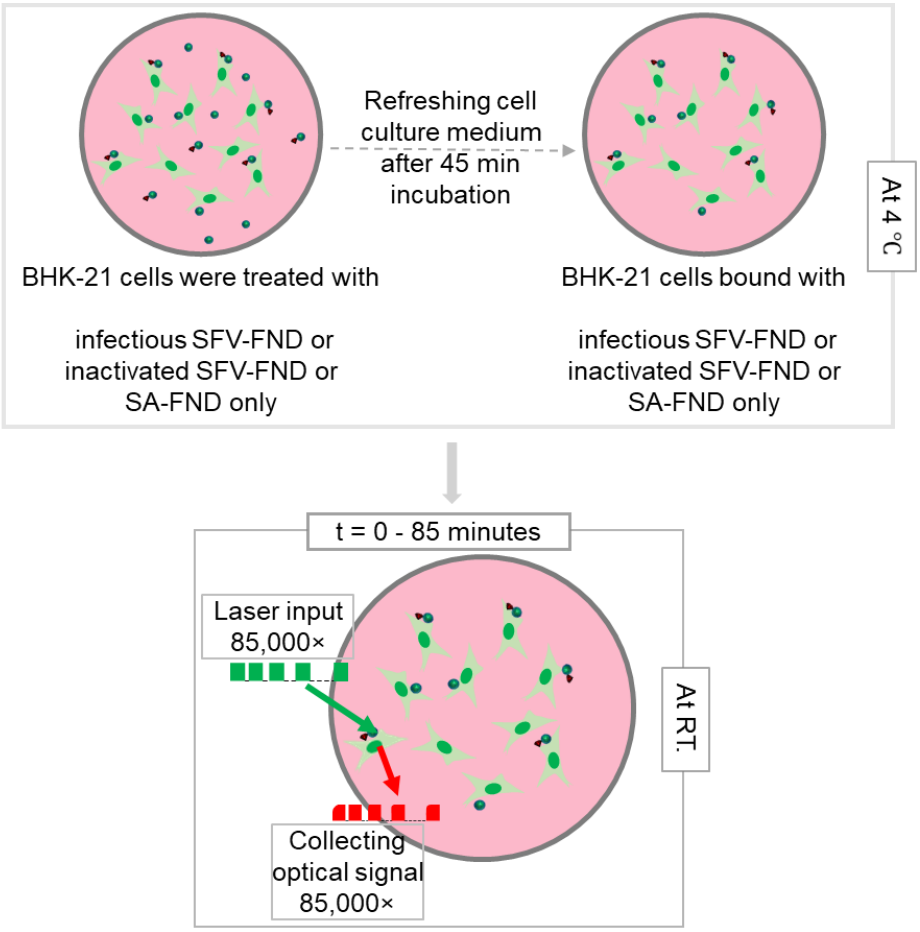

Figure S10. Schematic representation of the experimental scheme to investigate pseudo real-time radical variation using infectious SFV-FND, inactivated SFV-FND, and SA-FND.

S9. Change in cellular morphology and cell viability as a function of time

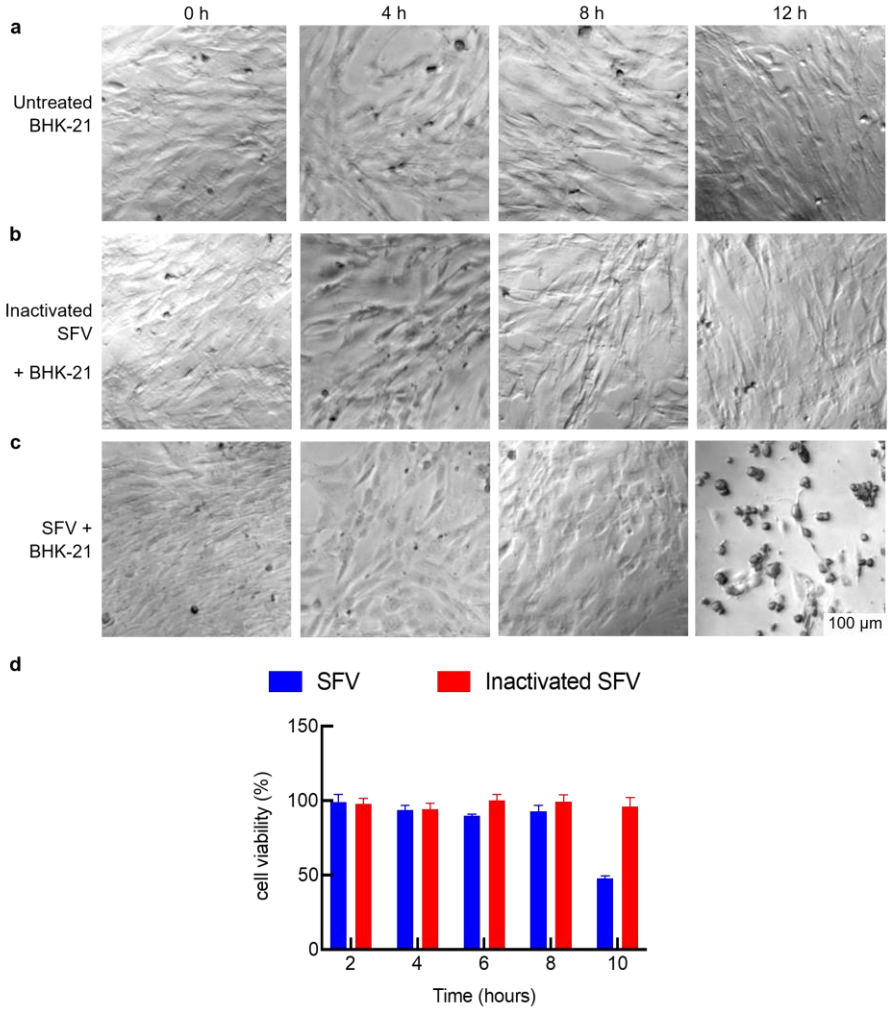

Figure S11. Images of SFV (a), inactivated SFV (b), and RPMI medium (c) treated BHK-21 cells at 0, 4, 8, and 12 hpi. (d) Cell viability of BHK-21 cells at different infection times.

The cell viability of BHK-21 during SFV infection was evaluated using an MTT assay at different infection times, by following the same infection procedure elaborated in the main manuscript. Specifically, SFV (MOI=20)

and inactivated SFV were added to BHK-21 (10,000 cells/well) seeded in 96-well plates. After 0, 4, 8, and 12 hpi, the cells treated with live and inactivated SFV were imaged by differential interference contrast (DIC) microscope (Fig S10a-c). Then 3-(4,5-dimethylthiazol-2-yl)-2,5-diphenyl tetrazolium bromide (MTT) solution (50 µL, 5 mg/mL) in PBS was added to each well, and the cells were cultured for another 3 h. The MTT-formazan generated by BHK-21 cells was dissolved in 150 µL of DMSO, and the absorbance at 570 nm of each well was measured by a plate reader. The absorbance of the wells only containing DMSO was used as a background signal. The relative cell viability was determined by comparing the absorbance at 570 nm with cells cultured in RPMI medium (control group, without exposure to SFV or inactivated SFV). The data in **Figure S11d** mean ± SD (n=4).

The result of cell viability assay is consistent with the morphology study. In the first 8 h post infection by SFV, BHK-21 cells maintain their viability (above 95 %) and morphology. The MTT assay shows that the viability of cells treated with live SFV is around 50 % at 12 hpi, which can also be observed from the bright field images. Around 12 hpi, cells seem to start lysis after being infected by SFV (MOI=20). On the other hand, BHK-21 cells treated with inactivated SFV have similar cell viability and morphology with the control group even at 12 hpi.

S10. Sensitivity of FND, SA-FND, and SFV-FND to $GdCl_3$

Two types of fluorescent nanodiamonds, 70 nm FND and streptavidin modified FND (SA-FND, 100 nm) were used in this work to investigate the intercellular radical response. In order to investigate the radical response near viral particles, SA-FND was further conjugated with SFV to form SFV-FND. A $GdCl_3$ sensitivity experiment was performed to ensure that all kinds of FNDs used in this work (FND, SA-FND, and SFV-FND) show the same sensitivity to magnetic noise. Briefly, FND, SA-FND, and SFV-FND (1 μg FND equiv.) were seeded to 4-quartered glass-bottom petri dishes, respectively. Before the measurement, the $GdCl_3$ solutions with desired concentrations (0, 1, 10…10^6 nM) were added to dishes. T_1 measurements were recorded on 5-6 diamond particles at each concentration according to the procedure described above. **Figure S12** indicates that all the diamond particles and virus-diamond conjugates used in this work have a very similar sensitivity to magnetic noise, and the sensitive range is even less than 1nM Gd^{3+}, which is more sensitive than conventional ESR.

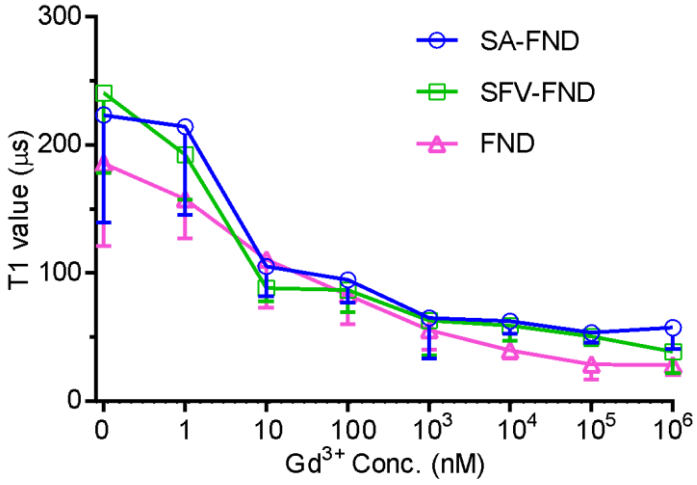

Figure S12. Sensitivity of FND, SA-FND, and SFV-FND to $GdCl_3$. Gd^{3+} was used as a contrast agent. The data was shown as mean ± SD (n=5-6).

Chapter 6

General discussion

The applications of the NV-center in diamonds are numerous and make use of (single) NV-centers in bulk diamonds or single NV centers or ensembles in single digit nanodiamonds. Fluorescent nanodiamonds (FNDs) with ensembles were used in this project to measure free spins from either paramagnetic ions or from free radicals in different environments, all of which are important for biomedical engineering.

Within the field there are several models which are used to fit the T1 relaxation curve. In **chapter 2** we investigated the most common models and developed a quantitative procedure to compare them. The most used models are the single, bi and stretched exponentials or derivations therefrom. The models were compared by applying them to a calibration curve based on increasing concentrations of gadolinium (Gd^{3+})[1]. They were compared based on the residuals of the fit and the signal to noise ratio (SNR) obtained from bootstrap. The residuals show that the single exponential fits the data worse compared to the bi and stretched exponentials, which can be explained by the single exponential being developed for a single NV-center and therefore does not fit ensembles as well. The SNR revealed that the bi and stretched exponentials perform very similarly, but small differences were observed, specifically that the bi exponential performs better at low concentrations while the stretched exponential is better at higher concentrations. It can be argued that this is due to the two exponentials in the bi exponential model predicting the same parameters at high concentrations and therefore not being independent of each other.

Although we compared the existing models, these might not be the best models in the end as the field is far from completely developed. The presented models for ensembles were developed based on the model for a single NV-center and extending the model mathematically. Although we show that these models have a reasonable result, what they describe regarding the ensembles is not as clear. Therefore, it is possible that another model will be developed based on the physical behavior of the ensemble. This new model can be compared to the already existing models using the same methods as done in **chapter 2**.

Besides determining when to use which model, data modelling also consists of improving the data modelling itself. In this work we did this in

three different ways: pulse fitting, bootstrap and rolling window. First, pulse fitting aimed to reduce the noise in the original pulses which are used to construct the T1 curve by fitting a function which describes the polarization of the NV-center under illumination. We showed that it was possible to use this model to fit the pulses reasonably well, often resulting in a small change in T1. However, this model is again based on the behavior of a single NV-center rather than that of the ensemble. Therefore, the model itself can be improved upon to fine tune the fitting itself.

Secondly, we constructed T1 distributions based on naïve bootstrap for all measurements which can be used to compare the most likely T1 value to the original fit. In addition to this, we can confirm the assumptions used during the calculations through assessing the shape of the T1 distribution obtained from bootstrap. Similar to the fitting of the pulses, we see that often the most likely T1 value is similar to the value obtained from fitting the original T1 curve, validating the found T1-value. Also, we used the bootstrap distributions to compute the standard deviation of a single measurement. Here we observed that, compared to the standard deviation obtained from the group of particles, the relative error is comparable at the lower concentrations, but becomes smaller at the higher concentrations. In this work, only the naïve bootstrap has been used, which is the least complex way of performing it. There are other bootstrap methods in which additional information could be obtained, especially due to the measurement having a temporal resolution.

Lastly, the rolling window was used to improve the temporal resolution of the measurement. In our group we try to measure free radicals in cells and chemical reactions. Most free radicals are very short-lived (ns to days) due to them being highly reactive. Each measurement takes on the order of microseconds but to obtain enough statistical power one needs to collect around 10.000 repetitions. The complete measurements last for 10 minutes, so each T1 value found was the average T1 value for these 10 minutes. This shows a mismatch between the measurement time of the experiment and the lifetime of the free radical. Therefore, we used the rolling window to improve the temporal resolution, showed how the method is applied and how a change in concentration looks like with this method. Additionally, the minimum number of repetitions required for a stable T1 value over the duration of the

experiment was determined. However, this so-called window size does depend on the quality of the initial measurement, a measurement with more counts can use a smaller window than one with only a few counts. Additionally, these curves are still quite noisy and are hard to align with when something specific happens in multiple occasions at timings that are not exactly the same in all cells. Furthermore, we managed to reduce the measurement time significantly with a slightly different pulsing sequence, reducing the measurement time from 10 to 1 minute. However, this method can still be applied to this pulsing sequence to increase the temporal resolution even further.

Having all these options to analyze the data, we used the FNDs in **chapter 3** to measure the copper concentration during a fenton like reaction with copper. This experiment aims to proof that it is possible to measure a biologically relevant concentration of paramagnetic copper (Cu^{2+}) in solution. Copper in this specific case is of interest as it can be found within cells and can lead to damage[2], however not all species of copper are paramagnetic. Here H_2O_2 was used to transfer the charge state of the paramagnetic copper as found in the salt ($CuSO_4$) to one which is not paramagnetic (Cu^{1+} or Cu^{3+}). However, during this reaction, another free radical will be formed, which is the *OH radical. We found that we can measure the paramagnetic copper in water, even at nanomolar concentrations. These specific concentrations are very hard or impossible to measure with conventional methods such as EPR and UV-vis absorption. However, the recovery after the addition of H_2O_2 is only visible as a trend, but was not significant. This could be due to errors in producing exact concentrations of *OH or differences between individual particles.

However, we identified that the copper ions are attracted to the FNDs, therefore reducing the T1 even more due to the ions being in a close vicinity to the FNDs. This is likely due to the FNDs being electron-negatively charged due to the different surface groups mainly consisting of oxygen[3,4], and therefore attracting the positive ions. It was shown that this effect was small, but present nonetheless. However, this does imply that the same thing might happen with other ions, therefore designing similar experiments requires some careful considerations. Additionally, the FNDs can be treated to adjust the surface chemistry to be less electron-negative,

however this might also affect some other properties of the FND (such as T1 and aggregation) as well.

The main purpose of the FNDs is to measure a magnetic field, which in the case of measurements of chemical reactions this is the fluctuating magnetic field created by the free electron spin of paramagnetic species, such as Cu^{2+}, Gd^{3+} or OH^{-} radicals. The strength of a magnetic field depends not only on the strength of the source, but also on the distance to the sensor. Therefore, in **chapter 4** FNDs were embedded in a polylactic acid (PLA) polymer film in order to measure the rate at which the film degrades. This is of interest as PLA nanoparticles have a wide range of potential applications[5] The PLA film was degraded with a high pH solution which was enriched with gadolinium ions (Gd^{3+}) as a spin noise source to be sensed. We successfully showed a decrease in T1 over the course of the degradation and were able to track the fate of the FND during the degradation. We showed that there is no movement in the xy-plane, but a somewhat large movement in the z-plane. This was explained by a combination of two phenomenon. The first is the degradation itself, the second is the film detaching from the glass of the petri dish and floating on top of the liquid therefore lifting the particle slightly. The former is the phenomenon that we wanted to observe the latter is an experimental issue that we solved during this project. Additionally, we first observed a strong increase in T1 (the distance to the surface increases) which is explained as the film swelling as also shown by the QCM measurements before it starts degrading, therefore leading to an increase in distance between the FND and the surface. The QCM showed that the swelling of the film was rather minimal, while the T1 increase was somewhat large comparatively. This is mostly due to the rather small sensing distance of the FND.

A large problem observed specifically in this study is the large variation between different baseline measurements. This difference was expected as we cannot define the exact distance to the surface of the FND, therefore increasing the variation for each FND. This variation was only amplified by the difference between individual FNDs themselves. It has been shown that T1 and other variables vary quite drastically for individual FNDs, therefore introducing an intrinsic error to the measurement[6]. However, part of this intrinsic error, the part originating from the variation

between particles, can be reduced by using the same particle during a sequential measurement and using the relative change in T1.

Another potential consideration is that the material itself might affect the T1, however this is a constant error. Therefore, the FNDs can be used not only in polymer materials, but potentially in other materials. As long as a nanodiamond within the material can be reached with the green laser light, they can be used to study different material properties. In this experiment we focused on the change in distance between FNDs and the degradation solution. However other properties can be studied as well, such as the behavior of magnetic fields within specific materials[7]. In addition, FNDs embedded in PLA can be used in biological environments where the degradation happens due to the intercellular medium.

The final application in this work was to actually use the FNDs in cells to sense the production of free radicals. In **chapter 5** we used FNDs to sense the internal environment of cells, here FNDs were taken up by BHK-21 cells after which these cells were infected with the Semliki Forest virus (SFV). This is a common model used to study the effects of viral infections[8]. In this chapter both the T1 and the fate of the FNDs are followed for up to 10 hours after the infection. In addition to just having the FNDs being taken up by the cell, they were also attached to the virus particles, which allowed us to track the fate and T1 at the site of infection. We showed that there are patterns of free radical production at specific times post infection. Additionally, we showed that the movement of the FNDs in the cytoplasm was elevated for cells infected with the virus.

When the FND was linked with the virus, a clear decrease in T1 was observed. This implies that there is an elevation of the free radical concentration at the site of infection, which is not observed with FNDs taken up before the experiment. During the observed time viral membrane fusion and uncoating events occur. This shows that the free radical production is local to where the fusion between the cell and the membrane occurs. This shows a unique ability of the FNDs to measure localized spin noise and magnetic fields at room temperature, something which cannot be done with the conventional methods.

Working in cells brings additional challenges in combination with the previously mentioned limitations. The first being that each cell is slightly

different and nanodiamonds are potentially at different locations within the cell. Although targeting of the FNDs is possible by absorbing targeting moieties onto the surface of the FND, this is not a guarantee that they end up where they are supposed to go. Additionally, this is something which differs between different cell lines and might affect T1 in itself as there is a layer of other materials on the surface of the FND. The cells themselves also have their own preferences on their requirements for health growth and development. Therefore, there are a lot of additional effects that occur that might affect the T1 values found when working with cells. However, working with cells also has certain advantages as cells produce free radicals continuously rather than in bursts as is more common in chemical reactions. Their concentrations are also maintained relatively constant by homeostasis. This allows us to measure the rate at which the free radicals are produced under certain circumstances.

However, this does not limit the potential applications of FNDs within cells, especially if these challenges can be overcome with targeting techniques and more homogeneous particles. When it comes to viral infections, so far, we only tested a single model while there are many more. The changes in free radical concentrations over the course of the infection will help with the development of treatments which might alleviate the negative effects of a viral infection. In addition, there are many more types of diseases and conditions which can be studied with the FNDs.

Although the work presented here shows a wide range of possible applications of the FNDs, a lot of them have not been explored yet. Additionally, some of the work presented here highlighted some clear limitations of the FNDs as they currently are. The most important is the inhomogeneities between the different particles, specifically when it comes to T1. As a result, each T1 measurement starts with an uncertainty especially when the measurements have to be performed on different particles. Either being able to select particles with certain properties or the development of more homogeneous particles will go a long way towards solving the large initial variation. Another way of improving T1 is to improve the temporal resolution even further. Nowadays it is possible to reduce the T1 measurement by reducing the number of dark times probed. Ideally, this can be reduced even further by only probing 2 different dark times. Additionally, other applications can be enabled by also considering the T2

relaxation of the NV-center. This would allow for the identification of specific free radicals by using complex pulsing sequences such as double electron electron resonance (DEER) measurements. Combining these will open a wide range of possibilities for which the T1 so far has proven to be not selective enough.

The field of working with FNDs has expanded greatly over the last few years, shedding light on all potential applications of FNDs in materials, cells and other applications. The work presented in this thesis is only a very small sample of all the potential applications of FNDs. However, it shows that by using them, many more potential applications can be found.

References

1. Perona Martínez, F., Nusantara, A. C., Chipaux, M., Padamati, S. K. & Schirhagl, R. Nanodiamond Relaxometry-Based Detection of Free-Radical Species When Produced in Chemical Reactions in Biologically Relevant Conditions. *ACS Sensors* **5**, 3862–3869 (2020).

2. Yruela, I. Copper in plants: Acquisition, transport and interactions. *Funct. Plant Biol.* **36**, 409–430 (2009).

3. Nagl, A., Hemelaar, S. R. & Schirhagl, R. Improving surface and defect center chemistry of fluorescent nanodiamonds for imaging purposes-a review. *Anal. Bioanal. Chem.* **407**, 7521–7536 (2015).

4. Shenderova, O. A. & McGuire, G. E. Science and engineering of nanodiamond particle surfaces for biological applications (Review). *Biointerphases* **10**, 030802 (2015).

5. Farah, S., Anderson, D. G. & Langer, R. Physical and mechanical properties of PLA, and their functions in widespread applications — A comprehensive review. *Adv. Drug Deliv. Rev.* **107**, 367–392 (2016).

6. Reineck, P. *et al.* Not All Fluorescent Nanodiamonds Are Created Equal: A Comparative Study. *Part. Part. Syst. Charact.* **36**, (2019).

7. Tetienne, J. P. *et al.* Quantum imaging of current flow in graphene. *Sci. Adv.* **3**, (2017).

8. Atkins, G. J., Sheahan, B. J. & Liljeström, P. The molecular pathogenesis of Semliki Forest virus: A model virus made useful? *J. Gen. Virol.* **80**, 2287–2297 (1999).

Summary

Quantum sensing has been rapidly evolving. Nowadays there is a wide range of potential quantum sensors, one of these is the NV-center in diamond. The NV-center senses the random magnetic noise produced by paramagnetic atoms and molecules. Additionally, the NV-center is hosted in diamond it is able to make use of the impressive properties of diamond. This includes the biocompatibility and surface properties, which means that the FNDs can be used in a wide range of materials and bio applications. In this thesis we explored a number of these applications.

The basic properties of FNDs are at the basis of the thesis and were therefore discussed in chapter 1. First the focus was put on the physical properties of diamond to show the unique properties of the host material. Afterwards the uses of the NV-center in nanodiamonds were discussed. Here, a specific focus was put on the application of nanodiamonds for biological and biomedical applications such as quantum sensing of the environment within the cell at room temperature. Lastly, the basic principles of T1 measurements was discussed.

After the introduction of the method, the analysis was discussed. In chapter 2 the most commonly used models were discussed. These models were compared to each other based on a calibration curve of the sensitivity of the fluorescent nanodiamonds to varying concentrations of gadolinium. It was shown that the extensions of the basic single exponential model, the bi and stretched exponentials, explain the varying concentrations best. It was shown that the initial conditions and the expected changes determined which of the models was better.

In addition to comparing the different models, we also showed different methods to improve data analysis. The methods include fitting the pulses to reduce the signal to noise ratio, bootstrap to compute the intrinsic error of the T1 measurement and rolling window to improve the temporal resolution. We found that most of these methods are applicable to the results, however they can be further improved upon.

One application of quantum sensing with the NV-center is to measure the production of paramagnetic species in chemical reactions. In chapter 3 we produced a fenton reaction with copper in which the

paramagnetic species of copper(Cu^{2+}) are transformed to non-paramagnetic ones (Cu^{3+}) and OH radicals are produced. Because of this the T1 in water could be compared to the situation with paramagnetic copper and the recovery in the presence of non-paramagnetic copper due to the addition of H_2O_2. Which is also what we saw, however the recovery was not as stable due to the reaction being not continuous.

Another application is tracking degradation of polymers. In chapter 4 we embedded the FNDs in a thin film of PLA. The degradation solution was enriched with Gadolinium to supply a spin contrast agent. It was shown that we could both track the particle in the film during degradation and perform T1 measurements in the film. As the film degrades the gadolinium ions can approach the FNDs in the film. Due to this, we show that the T1 decreases over time. However, it was shown with both the conventional methods and with T1, that the film first swells before it starts degrading.

The last application discussed in this thesis (chapter 5) was using T1 to track the changes in free radicals produced in cells over the course of a virus infection. In this study a standardized model of BHK-21 cells infected with Semliki Forest virus was used. The free radicals were tracked both at the site of the infection and in the cytoplasm in the cells. Additionally we tracked the mobility of the FNDs during the measurements and have shown that there is a difference between cells with and without infection. In addition we showed that there is a change in free radical concentration at the site of infection.

In the final chapter (chapter 6) we discuss the advantages and disadvantages of each of the studies presented in this thesis. We also discuss some of the obstacles which are still to be overcome within the method of quantum sensing with FNDs.

Samenvatting

Kwantum metingen heeft zich snel ontwikkeld. Er is nu een ruim aanbod aan mogelijke kwantum sensoren, waarvan de NV-center in diamant er één is. De NV-center meet de magnetische ruis die geproduceerd wordt door paramagnetische atomen en moleculen. Daarnaast is de NV-center gehost in diamant waardoor het gebruik kan maken van de indrukwekkende eigenschappen van diamant. Hiertoe behoort de bio-comptabiliteit en oppervlakte eigenschappen, wat betekent dat de FNDs gebruikt kunnen worden in talloze materialen en biologische toepassingen. In deze proefstelling hebben we een aantal van deze toepassingen onderzocht.

De basis eigenschappen van de FNDs vormen de basis van dit proefschrift en zijn daarom besproken in hoofdstuk 1. Als eerste werd de focus gelegd op de fysieke eigenschappen van diamant om de unieke eigenschappen van het host materiaal te laten zien. Daarna werden de toepassingen van de NV-center in nanodiamanten besproken. Hier werd specifiek gefocust op de applicaties van nanodiamanten voor biologische en biomedische applicaties zoals kwantum metingen van de omgeving in de cel op kamer temperatuur. Als laatste werden de basis principes van de T1 meting besproken.

Na de introductie van de methode werd de analyse besproken. In hoofdstuk 2 werden de meest frequent gebruikte modellen uiteengezet. Deze modellen werden met elkaar vergeleken op basis van een kalibratie curve van de gevoeligheid van de FNDs voor variërende concentraties van gadolinium. We lieten zien dat de uitbreidingen van de simpele single exponentieel model, de bi en gestrekte exponentiële modellen, verklaren de variaties in contracties het best. Het was aangetoond dat de initiële conditie en de verwachte veranderingen bepalend zijn voor het selecteren van het beste model.

Naast het vergelijken van de verschillende modellen keken we ook naar verschillende methodes om de data analyse te verbeteren. De besproken methodes waren: het fitten van de pulsen om de signaal om ruis ratio te verbeteren, bootstrap om de intrinsieke fout in de T1 meting te berekenen en rollend raam om de temporale resolutie te verbeteren. We

vonden dat deze methodes gebruikt kunnen worden op de resultaten, echter de methodes kunnen verbeterd worden.

Eén van de applicaties van kwantum metingen met de NV-center die besproken werd in dit proefschrift was het meten van de productie van paramagnetische species tijdens een chemische reactie. In hoofdstuk 3 produceerden we een fenton reactie met koper waarin de paramagnetische vorm van koper (Cu^{2+}) werd omgezet naar de niet paramagnetische vorm (Cu^{3+}) en OH radicalen werden gevormd. Doordat dit gebeurt kan de T1 in water vergeleken worden met situaties met paramagnetische koper en het herstel wanneer de koper wordt omgezet naar de niet paramagnetische vorm door het toevoegen van H_2O_2. Dit is ook wat we hebben geobserveerd, echter het herstel was niet stabiel doordat de reactie niet continue was.

Een andere applicatie was het volgen van de degradatie van polymeren. In hoofdstuk 4 hebben we nanodiamanten ingesloten in een dunne PLA film. De degradatie solutie was verrijkt met Gadolinium om een spin contrast toe te voegen. Het was aangetoond dat we zowel de deeltjes kunnen volgen als de T1 metingen kunnen doen tijdens de degradatie van de film. Terwijl de film degradeert kunnen de gadolinium ionen dichterbij de FNDs in de film komen en daardoor T1 verlagen. Ondanks dat T1 tot dusverre de degradatie nog niet actuele tijd kan laten zien, geeft het wel een correcte tijdsvenster waarin de degradatie plaats vindt. Daarnaast zijn kleine veranderingen opgeblazen in de T1 metingen zoals te zien is tijdens het zwellen van film aan het begin van de degradatie.

De laatste toepassing besproken in dit proefschrift (hoofdstuk 5) was het meten van de verandering van vrije radicalen met T1 tijdens een virus infectie. In dit onderzoek werd een gestandaardiseerd model voor een virus infectie gebruikt, namelijk de infectie van BHK-21 cellen met het Semliki Forest virus. De vrije radicalen werden gemeten zowel op de plaats van de infectie en in het cytoplasma van de cel. Daarnaast werd de mobiliteit van de FNDs bijgehouden tijdens de metingen en hebben laten zien dat er een verschil is tussen cellen met en zonder infectie. Daarnaast hebben we laten zien dat er een verandering is in de concentratie van vrije radicalen op de locatie van de infectie.

In het laatste hoofdstuk (hoofdstuk 6) werden de voor en nadelen van elk onderzoek in dit proefschrift besproken. We bespraken ook een aantal van de obstakels die nog overwonnen moeten worden met de methode van kwantum metingen met FNDs.

Acknowledgements

A long and amazing journey has come to an end and it was one that I didn't experience alone. These 4 years would not have been possible or as amazing without my great collegues, friends and collaborators. Therefore I want to express my sincere appreciation for all the people who have been with me during this time.

First of, I want to thank **Romana Schirhagl** for accepting me into the group. I remember going tot he lab as part of the interview and being extremely nervous, but still you gave me the opportunity to work in the group. As a supervisor you were always ready to help with questions and you were always so patient. You were also willing to go with a slight sidestep for a project which allowed me to follow my own curiosities. I couldn't have wished for a more supportive supervisor and I want to thank you for being that.

Secondly I want to thank my co-supervisor **Viraj Damle**, we worked together so much for the virus project and I learned so much from you. You have an amazing work attitude and you thought me valuable skills during this time. I want to thank you for being my co-supervisor.

I also want to thank my reading comittee, **prof. Thorben Cordes, prof. Petra Rudolf, prof. Peter Olinga and dr. Malgorzata Wlodarczyk** for taking the time to read my thesis and give valueable feedback.

The diamond group consists of amazing people whom I was blessed to meet over the years. Before I even joined the group I met **Yori**, you showed me the lab and were an amazing collegue whith who I shared my first conference. If things went wrong you were always ready to help. When I joined the group **Felipe** tought me everything I had to know about the setups and how to do the experiments. I will be forever grateful for the time you took to answer all my questions. During the time I was learning, **Thamir** was with me while trying to fix a problem. I always enjoyed working towards solutions with you and you were always ready to help even when I didn't notice I needed the help. When I didn't fully understand or simply didn't know something about the (electronic parts of the) setups I could always ask **Ari**. At times you seemed willing to drop anything you were doing to help me and although we didn't fully finish implementing T2, I

want to thank you for the experience. I also want to thank you for being my paranymph. When it coems to working together on projects I want to thank both **Runrun and Sandeep** as my experiences working together with you both were amazing. **Sandeep**, you were always so insightful. Admittingly, chemistry is not my best subject, but you made everything understandable. And when it came to tackling a though problem you never gave up. Also, thank you for being part of my reading comittee. **Runrun**, there is so much more I want to say than I can say here. But most of all, you're an amazing friend and always able to be positive, even if things are bad. You're practical and I'm so happy to have been able to meet you and work with you as much as we did. Another great collegue I had the honor of working together with was **Kaiqi**. Everytime something had to be aranged I could trust you would do it. I sincerely enjoyed working together with you and you have an amazing set of skills. I was also happy to get the opportunity to work together with **Xixi**, for the longest time we didn't meet, but you were always willing to provide information and to get more if it was needed. Another great collaborator I looked up to before I met you was **Mayeul**. Thank you for always be willing to answer my questions and all the work you put in with the Data analysis paper. I was happy to meet you in Barcelona and I wish you the best.

Besides these people there are more great people in the diamond group. Some of them have left already and others are starting their own journey. First of all, I want to thank **Aryan.** I had some of the greatest cat conversations with you and even Jane was willing to show herself. I want to thank **Aldona** for always be willing to explain complex cell stuff and how to determine the condition of the cells. I was always able to have good conversations with **Alina** and thank you for being the person who helped identify whether something was wrong with the setups. I want to thank **Rokshana** for always being so sweet. When I was making long hours due to the corana restrictions you always made sure I was still taking care of myself. I want to thank you for all the food you gave me and I hope you do well. I also want to thank diamond group members, both old and new, for their amazing help and conversations: **Linyan, Yuchen, Claudia, Siyu, Yue, Arturo, Neda, Kiran, Charles, Britt and Elsa**. I hope you will all have amazing careers and a good time where ever you are.

I was also blessed with great roommates. When I arrived in the department I was given a warm welcome by **Guangyue and Huaying.** I want to thank you both for the potluck we shared. We also had some great conversations which I missed quite a lot during the lockdowns. Later on I had fortune to meet **Guang**, I hope you will have a great time getting to know dutch culture and food (and drinks). I wish you the best of luck with your own thesis and defense. My other new roommate **Jie** is an amazing person. She prepares some great food and is always willing to make small talk. I was so fortunate that I could share this in my last moths in the depart.

The BME department is not only made up of the students, but the scientific staff is what keeps everything together. I want to thank **Ed** for always be willing to help me with something technical and helping me understand the software even more. With your help I was able to identify problems which I would have otherwise missed. I always felt comfortable talking to you and to ask questions. I also want to thank **Willem**, although we only started working together later you asked questions which made me think on why I did things the way I did, which was good to remember. I also want to thank you for always being willing to help if needed. I also want to thank the other scientific staff, **Gesinda, Joop, Betsy, Willy, Hans, Reinier, Brandon** for all the work they put into the department to keep things running as they are.

I want to thank the rest of the BME department (**Hélder, Prashant, Theo, Patrick, Jelmer, Henny, Henk, Inge and all the students**) for their very useful input during the BME presentations.

I want to thank my dear friend **Jorge** for being there when needed and helping me relax at times of great phd stress. You're a great person and I know you will succeed with anything you set your mind to. I also want to thank **Alexander.** Our bi-ish weekly meetings have thought me so much about myself and I want to thank you for helping me design the cover of this thesis.

Als laatste, maar zeker niet de minst belangrijke mensen wil ik mijn familie bedanken. Jullie hebben me altijd gesteund en ondanks dat het onderwerp niet het makkelijkste is hebben jullie altijd je best gedaan om het toch te begrijpen. **Sophie en Gerard**, ik had geen betere schoonouders kunnen hebben en ik ben blij dat ik dit met jullie mag delen. **Papa en Mama**, misschien was het lang geleden dat jullie niet meer bij konden houden wat

ik deed, maar toch hebben jullie me altijd gesteund in wat ik deed. Ik ben blij dat ik deze kans heb kunnen nemen en dat ik altijd op jullie kon terug vallen. Als laatste wil ik mijn lieve zus **Silke** bedanken. Het was niet altijd makkelijk, maar voor jou was het altijd het makkelijkste om te begrijpen waar ik mee zat. Je had soms eerder door dat een artikel van mij was gepubliceerd dan ikzelf. Ik hoop dat jij, **Mark en Saar** veel plezier gaan hebben en dat we nog vele jaren Sinterkerst en nieuw kunnen vieren.

De belangrijkste persoon wordt altijd als laatste aangesproken en dat ben jij, mijn lieve **Erwin.** Zonder jou en jouw steun was ik denk ik nooit gekomen waar ik nu ben. Woorden schieten te kort om uit te drukken hoe dankbaar ik ben. Maar, ik ben dankbaar dat je er altijd voor me was, ook al zat het tegen. Dat je altijd hielp met die dingen waar ik moeite mee had, zoals het proeflezen van teksten. Je was regelmatig mijn geheugensteun (die ik dan ook echt nodig was!) en je maakt de beste gerechten. Ik hoop dat ik je de rest van mijn leven bij me kan houden.

About the Author

Thea Vedelaar was born on the 4th of February in Emmen, the Netherlands. She graduated from the Hondsrug College in Emmen in 2012 and afterwards went to start her bachelor in Physics at the University of Groningen. During this time she helped organizing and participated in the Japan Netherlands Student Conference (JNSC). Near the end of her bachelor degree she completed an internship at the KVI institute on the topic of proton imaging. Afterwards she continued with a master in physics at the Univeristy of Groningen. At the end of the master she did another internship, this time at the department of radiotherapy at the UMCG. She focused on the development of finding image biomarkers in order to improve the treatment of head and neck cancers.

In late 2018 she started her PhD program at the UMCG in the bioanalysis and imaging group which is lead by prof. Romana Schirhagl. Here the main focus of her projects would be different applications of quantum sensing with the NV-center in diamond. Additionally she learned to maintain and improve the home build confocal microscopes. During her PhD program she participated in a number of international conferences. Additionally she got nominated by the Dutch TV program Klokhuis for a science prize by explaining her study on virus towards Dutch children.